Catalytic Processes for Production of Chemicals from Biomass using Heterogeneous Catalysts

By

Mrunmayi D. Kumbhalkar

A dissertation submitted in partial fulfillment of

the requirements for the degree of

Doctor of Philosophy

(Chemical Engineering)

at the

UNIVERSITY OF WISCONSIN-MADISON

2017

Date of final oral examination: 05/05/2017

The dissertation is approved by the following members of the Final Oral Committee:

James. A. Dumesic, Professor, Chemical and Biological Engineering
George W. Huber, Professor, Chemical and Biological Engineering
Thatcher W. Root, Professor, Chemical and Biological Engineering
Christos T. Maravelias, Professor, Chemical and Biological Engineering
Ive Hermans, Associate Professor, Chemistry

ABSTRACT

Biomass has the potential to serve as a sustainable platform for the production of fuels and chemicals, however, there are several challenges associated with the deoxygenation of biomass-derived intermediates using heterogeneous catalysis. In this work, a cascade process to convert levoglucosan, an anhydrosugar present in pyrolysis oil, to distillate range hydrocarbons is discussed. In particular, the dehydration of alcohols and heterocyclics present in the mixture of monofunctional oxygenates obtained from the aqueous-phase hydrodeoxygenation of sorbitol (derived from levoglucosan) was investigated. The dehydration of a model compound, 1-hexanol, was carried over H-ZSM-5, SiO_2/Al_2O_3, γ-Al_2O_3, and $MgAl_xO_y$. The highest rate and selectivity towards hexenes was observed over SiO_2/Al_2O_3 with minimal activity towards dihexyl ether. Thereafter, the conversion of a simulated feed representing the monofunctional stream as well as the actual effluent from sorbitol aqueous-phase hydrodeoxygenation was performed over SiO_2/Al_2O_3. The olefin yields obtained are similar for the simulated as well as the actual feed indicating that the conversion of various functionalities such as alcohols, aldehydes, carboxylic acids, and heterocyclics occurs independently. The C_2-C_6 olefins thus obtained can be oligomerized over acid catalysts to produce distillate range hydrocarbons.

The vapor-phase dehydration of cyclic ethers to dienes over solid acid catalysts is examined. Dienes, traditionally obtained through fossil fuel and natural gas resources, are important chemicals used in the production of plastics, adhesives, as well as fine chemicals. A reaction network for 2-methyltetrahydrofuran dehydration to pentadienes over SiO_2/Al_2O_3 was proposed using weight hourly space velocity studies and the relative stability of the carbenium ion intermediates. Reaction kinetics studies performed to probe the effect of temperature and partial pressure of 2-methyltetrahydrofuran revealed a strong interaction between the cyclic ether and the

catalyst surface. Though the catalyst deactivated with time on stream, it was regenerable upon calcination with no observable loss in initial activity. Solid acids with both Brønsted and Lewis acid sites are active for dehydration to dienes with the catalytic activity for diene formation being proportional to the concentration of Brønsted acid sites on the catalyst. The dehydration of other cyclic ethers such as tetrahydrofuran, tetrahydropyran, and 2,5-dimethyltetrahydrofuran resulted in the formation of their respective dienes. This conversion of cyclic ethers can serve as a potential route to produce dienes from biomass.

Next, the effects of addition of a promoter such as Sn to monometallic Pt catalyst and overcoating a Pt catalyst with alumina using atomic layer deposition are investigated for the dehydrogenation of alkanes for their use as endothermic fuels. The interaction of alkanes with metal surfaces results in the formation of coke precursors such as alkynes by deep dehydrogenation leading to catalyst deactivation. Thermogravimetric analysis and transmission electron microscopy were employed to study catalyst deactivation due to coke deposition and metal particle sintering. Several factors were noted to affect the catalyst performance for the dehydrogenation of ethane and isobutane, such as the support, metal loadings, and hydrogen co-feed pressure. The amount of coke deposited per surface Pt atom was lower on the PtSn catalysts as compared to the monometallic catalyst which is attributed to geometric and/or ligand effect brought about by Sn. The alumina overcoated Pt/γ-Al_2O_3 catalyst showed higher initial as well as steady state turnover frequencies for alkene formation as compared to the non-overcoated catalyst.

Lastly, the use of X-ray absorption spectroscopy for determining the catalyst nanoparticle structure for several bimetallic catalysts is discussed. The measurements for various catalysts - PtMo catalysts for water gas shift reaction, AuMo catalysts for reverse water gas shift reaction, and RhRe catalysts for C-O hydrogenolysis of biomass-derived tetrahydropyran-2-methanol -

were carried at the respective element edges to determine the metal oxidation states, bond distances between the constituent metals and local coordination numbers. These results were combined with the reactivity data and inferences from other characterization techniques to identify the nature of the active site, thereby providing a basis for future rational catalyst design.

ACKNOWLEDGMENTS

First and foremost, I would like to thank my parents, Dinkar T. Kumbhalkar and Sunita D. Kumbhalkar, for their incessant support and encouragement throughout my life. I look up to you in every sphere of my life, be it my professional career or trying to achieve a work-life balance. I thank my family- Dada, Aai, Anushree, Tanushree, and Vithoba for instilling in me the values of hard work and honesty.

I am profoundly thankful for to my advisor, Prof. James A. Dumesic, for everything he has taught me over the last five years. His tireless passion for learning something new every day in the field of heterogenous catalysis has kept me motivated throughout the years. I have immensely benefited from the advantages of being associated with a scientist of his stature. I am thankful for the opportunities I have had to learn the state-of-the-art techniques and improve my skill set. I have also made innumerable mistakes during my research here and I hope to learn from them and strive to be a better scientist.

I am thankful to Exxon Mobil Corporation and the Air Force Office of Scientific Research for funding the projects I have worked on during my graduate research. I would like to thank the members of my current thesis committee for their guidance as well as the other faculty that have contributed to my development throughout the years at UW-Madison.

I would like to thank all the past and present members of the Dumesic group that I have had the pleasure of working with. A special mention to David, Ana, Mei, Brandon, Carrie, Tom S, Ricky, Ronald, and Jeremy who taught me the basics- be it making a catalyst using incipient wetness impregnation or GC maintenance, during my early years in the lab. I would like to thank Judy Lewison for making sure the Dumesic lab runs smoothly and most importantly, for baking the best lemon bread in the world!

I have had the good fortune of several fruitful collaborations over the course of my graduate research. I extend my special thanks to Prof. Jeffrey Miller for his guidance with x-ray absorption spectroscopy. Over the last four years, his assistance with XAS experiments at Argonne National Laboratory and his expertise on the painstaking data analysis that followed, thoroughly helped me in better understanding of x-ray absorption spectroscopy with every project. I am grateful to all the Dumesic group members- Maddie, Siddarth, Isaias, Yifei, Insoo, and Zach, who accompanied me at Argonne for putting up with sleepless nights while performing XAS experiments. I thank Dr. Sungsik Lee for his collaboration on the Air Force project as well as his help in collecting XAS data. I would like to thank Prof. Mavrikakis and Dr. Guowen Peng for their guidance with the Air Force project. I thank David Jackson for his time and patience in teaching me how to make overcoated catalysts using atomic layer deposition. I thank Prof. Huber for his insightful questions and comments on the Exxon project. I am immensely thankful to my Exxon team members - Nat, Dan, and Peter, for their collaboration and contributions to the project. I am also thankful to Scott, Ross, and Ashley - our project team members from Exxon for their ideas and suggestions during the monthly meetings over the last two years.

I am also thankful to Dr. Eric Codner, Steven Schumacher, and Joel Lord- without whom, it would have taken me countless extra hours to troubleshoot my reactor system. I would like to thank the faculty and staff at UW for their help. Special thanks to Christi, and Kathy for their collaboration during my ChEGS term and Mary, Russ, and Beth for their help throughout these memorable years at UW.

I am blessed to have had made some amazing friends during the last five years in Madison. A big thank you to Rasika, Vidhya, Gowtham, Ashwini, Apoorv, Ayushi, Chaitanya K, and

Chaitanya W for the enjoyable board game nights, for making me feel at home away from home, and for all the awesome Indian food.

I wish to extend my thanks to Prof. Huber once again. I met Pranav because Prof. Huber decided to move from Amherst to Madison and for that I will be eternally grateful. Last but not the least, I thank Pranav for being with me through thick and thin over the years. His attitude towards various things in life and the sense of perspective he provides helps me in appreciating the bigger picture. Though the talks at home end up involving discussions about heterogeneous catalysis as those at work, I wouldn’t trade anything for having Pranav as a partner-in-crime for life. I look forward to moving with you in Midland but for me, we will always be Badgers and Madison will always be our home!

TABLE OF CONTENTS

LIST OF TABLES

LIST OF FIGURES

CHAPTER 1

Introduction

1.1. Introduction

The energy, material, and chemical industries rely heavily on fossil-based carbon resources such as petroleum, natural gas, and coal, for feedstocks. The field of catalysis has played a central role in the conversion of these raw resources into value-added end products. Approximately 90% of the industrial organic chemicals are manufactured from petroleum or natural gas, using a platform chemical approach.[1-3] The rise in world population and improved standards of living have resulted in an increase in demand for energy and chemicals, thereby increasing the use of diminishing fossil-based resources.[4,5] The current processes for manufacturing chemicals from these resources produce a large amount of waste and have high CO_2 emissions.[1,6] The economic, environmental, and political concerns have made it imperative to develop processes to meet these ever-growing demands with alternative and renewable sources of carbon such as biomass.[7,8] While there are several options such as solar, hydroelectric, nuclear, wind, and geothermal for production of electricity, biomass remains the only viable option for production of energy-dense carbon-based fuels and chemicals.[9] In recent years, biomass has attracted considerable attention as a renewable feedstock for production of fuels and chemicals, mostly due to its low cost and abundance.

There are three general classes of biomass: starches, triglycerides, and lignocellulosic biomass.[10] The first two, starches and triglycerides, are generally not considered a long term solution as they are integral parts of the food chain. Lignocellulosic biomass refers to the fibrous and woody portions of plants. These portions are inedible for humans and thus, do not compete with food sources. Lignocellulosic biomass is composed of cellulose (~40-50 wt%, a glucose polymer with β-glycosidic bonds), hemicellulose (~25-35 wt%, an amorphous C_5 and C_6 sugar polymer), lignin (~15-20 wt%, a complex amorphous polymer containing phenolic linkages), and lesser amounts of terpenes, ash, and extractives.[2,11] A study by U.S. Department of Energy in 2011 determined that over 1.2 billion dry tons of lignocellulosic biomass could be made available for large scale bioenergy and biorefinery industries by 2040 at a price of ~$60/dry ton which could potentially replace half of the transportation fuels consumed in the U.S.[12,13] Despite this advantage, lignocellulosic biomass is not being commonly used as a feedstock for production of fuels as the existing processes for upgrading are not cost-competitive to their fossil-based counterparts. In contrast to the low oxygen content (0.05-1.5 wt%) in crude oil,[14] biomass normally contains 16-49 wt% oxygen which makes it less energy dense.[15] To produce energy-rich fuels and chemicals from biomass, we need to partially or completely deoxygenate biomass either by removing it as CO or CO_2 which lowers carbon efficiency or by removing it as water which requires a source of hydrogen. The profitability from selling chemicals is higher than that from fuels. Although chemicals account for only about 10% crude oil usage, the sale of chemicals generates around USD 375 billion/yr which is comparable to that from high volume fuels (USD 385 billion/yr).[3,16] Therefore, the production of fuels from biomass can be integrated with the co-production of low-volume, high value-added chemicals to improve the economic potential.

Lignocellulose can either be treated as a whole (thermochemical route) or it can first be fractionated to yield streams of sugars and lignin which can then be processed independently (hydrolysis route) (Figure 1.1). The thermochemical routes, such as pyrolysis, gasification, and liquefaction, facilitate the deconstruction of biomass using direct application of heat and are comparatively inexpensive methods compared to the catalytic routes.[17] Pyrolysis oil or bio-oil is obtained via pyrolysis which is carried out in the absence of oxygen at 573-873 K and involves reactions such as dehydration, cracking, isomerization, dehydrogenation, aromatization, and coking. However, this bio-oil is a complex mixture that contains hundreds of highly oxygenated species, has high acidity and degrades with time. For this reason, bio-oil is unsuitable for use as a fuel and must be processed further.[13,18]

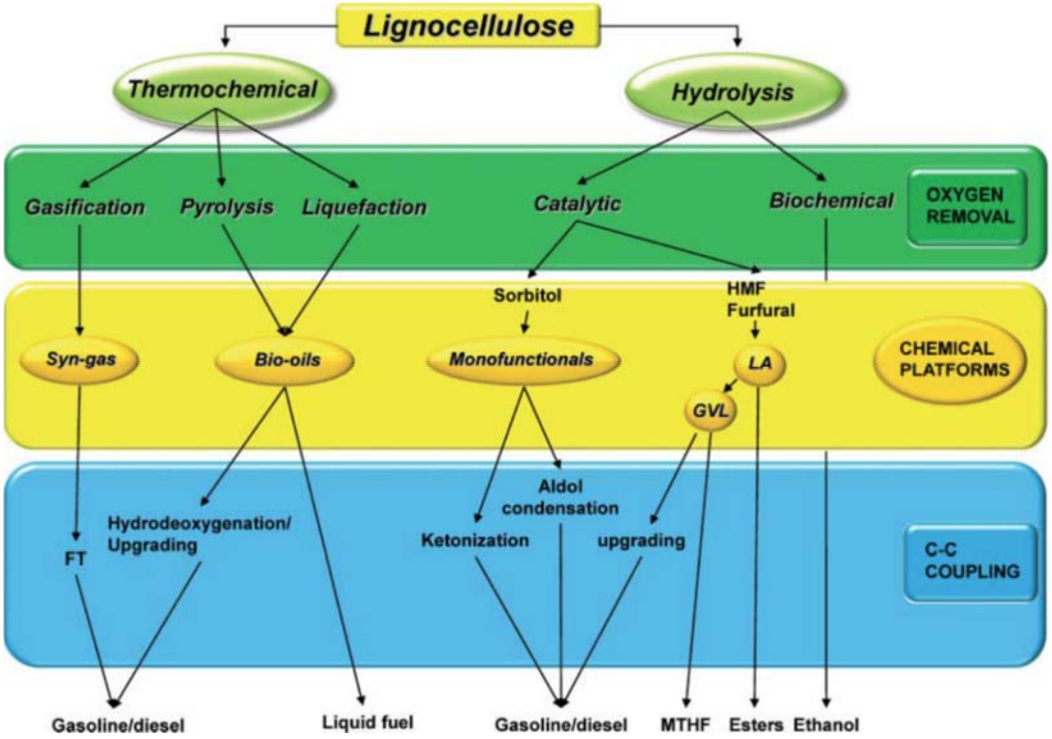

Figure 1.1. Strategies for conversion of lignocellulosic biomass (Adapted from Alonso *et al.*[10]).

Hydrolysis of the β-glycoside ether linkages using acid catalysis or enzymatic means is applied to break these bonds and yield simple carbohydrates.[19,20] The resulting mixture consists of C_5 and C_6 sugars representing a water-soluble source of carbon that can be further processed by hydrolysis, dehydration, isomerization, aldol condensation, hydrogenation, selective oxidation, and hydrogenolysis for the selective removal of oxygen functionalities for the production of fuels and chemicals.[10,13,21] Heterogeneous catalysts used for these reactions can be acids, bases, supported metals, and metal oxides. While these methods have higher costs unlike thermochemical pathways, selective formation of specific products can be obtained using aqueous-phase processing thereby achieving high carbon efficiency. A biorefinery concept based on this approach is illustrated in Figure 1.2 where carbohydrates from both the cellulose and hemicellulose fractions of biomass are upgraded to fuels and/or chemicals[22,23] The C_5 and C_6 sugars can be converted to furfural and 5-hydroxymethylfufural, respectively.[24] Variety of molecules such as furfuryl alcohol, 2-methyltetrahydrofuran, dimethylfuran, γ-valerolactone, etc. can be produced from furfural and 5-hydroxymethylfufural which can serve as chemicals and/or fuel additives.[25-27] Alternatively, aqueous phase reforming of both C_5 and C_6 sugars results in formation of monofunctional oxygenates which can be further deoxygenated to fuel precursors using the aforementioned chemistries.[28,29]

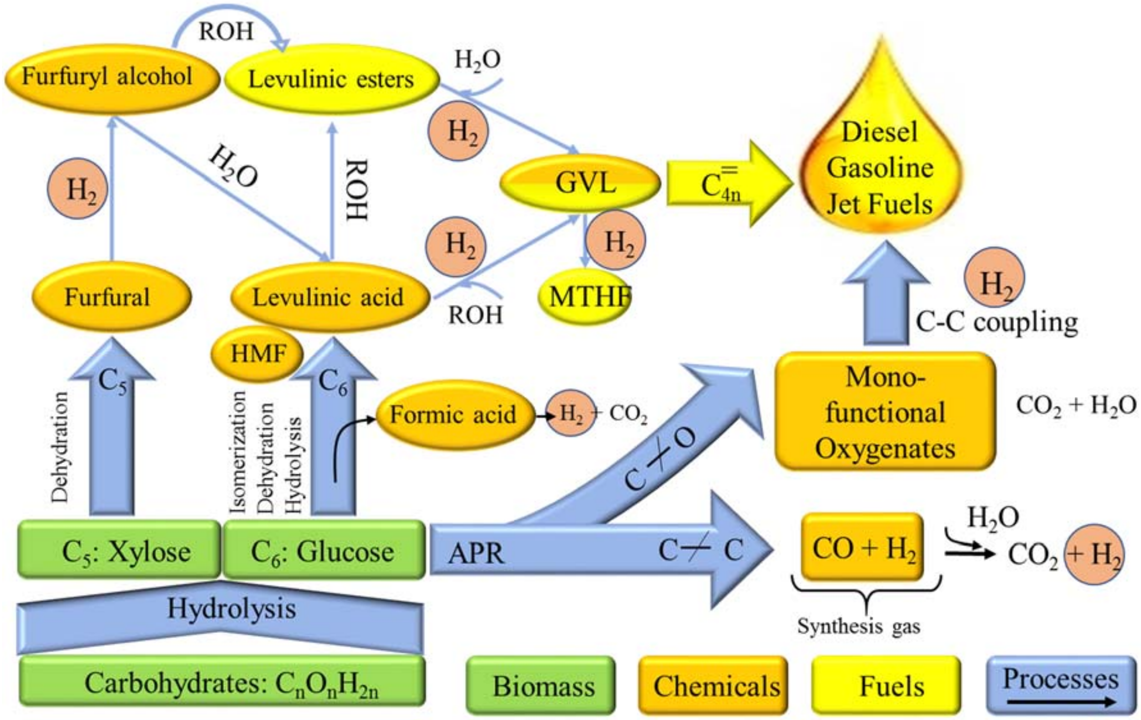

Figure 1.2. Roadmap for conversion of C_5 and C_6 fractions of lignocellulosic biomass to fuels and chemicals (Adapted from Wettstein *et al.*[22]).

Bimetallic catalysts display electronic and chemical properties that are distinct from their parent metals which often results in enhancements in the catalytic activity, selectivity, and stability. Since the pioneering contributions by Sinfelt *et al*. to the use of bimetallic catalysts,[30,31] changes in reactivities and selectivities have been reported for various chemistries such as dehydrogenation,[32-34] hydrogenolysis,[35,36] and oxidation.[37,38] The changes in ensemble size, ensemble composition, and electronic/ligand effect brought about upon alloy formation of the promoter metal and the parent metal modify the configuration and the binding energies of the reaction intermediates adsorbed onto the catalyst surface, which in turn result in changes in the catalyst behavior.[39] Numerous characterization techniques such as chemisorption, temperature programmed desorption, x-ray absorption spectroscopy, etc. are employed to determine the structure of the catalyst nanoparticle. Based on the structure-function relationships, conclusions can be drawn about the nature of the active site for a particular reaction thereby assisting in rational catalyst design.

The application of heterogeneous catalysis in various fields outlined above is the basis of the studies presented in the following chapters. The experimental methods used throughout the thesis are presented in Chapter 2. In Chapter 3, the multi-step conversion of an anhydrosugar, levoglucosan (LGA), present in the water-soluble fraction of pyrolysis oil to distillate range hydrocarbons will be discussed. Sorbitol can be obtained in near quantitative yield from LGA using hydrolysis and hydrogenation reactions. The aqueous-phase hydrodeoxygenation (APHDO) of sorbitol over Co/TiO_2 results in the formation of monofunctionals consisting primarily of alcohols and heterocyclics. The monofunctional intermediates can then be converted into distillate range molecules by dehydration-oligomerization route. The dehydration of alcohols is investigated for model alcohol compounds such as ethanol and 1-hexanol over H-ZSM-5, SiO_2/Al_2O_3, γ-Al_2O_3, and $MgAl_xO_y$ catalysts as well as the isomerization of olefins so formed. The reaction network for 1-hexanol dehydration based on weight hourly space velocity studies is discussed. The catalyst that shows higher selectivity towards intramolecular than intermolecular dehydration and stability with time on stream is chosen for studying the conversion of a simulated feed representing the effluent from the sorbitol APHDO reactor and the actual sorbitol APHDO feed in the same reactor.

The conversion of various functionalities is tracked during the reaction of the actual APHDO effluent. In addition to monoalkenes obtained from dehydration of alcohols, we observed dienes in the product stream from dehydration of heterocyclics. Distillate range hydrocarbons can then be obtained from the oligomerization of C_2-C_6 olefins over acid catalysts such as H-ZSM-5, Amberlsyt-70, and H-ferrierite.[40,41] Pyrolysis oil contains a complex mixture of higher oxygenates and it is imperative to develop strategies to deoxygenate these molecules for their use as fuel components. The process adopted here for the conversion of levoglucosan can be applied to other carbohydrates derived from biomass.

Chapter 4 focuses on the fundamental chemistry that occurs during dehydration of biomass-derived cyclic ethers to dienes over solid acid catalysts. The hydrodeoxygenation of cyclic ethers over transition metal catalysts to a mixture of alkenes and alkanes,[42,43] and the hydrogenolysis to polyols over bimetallic catalysts has been investigated.[36] There is limited work reported on the dehydration of cyclic ethers over solid acids. Heterogeneous catalysts dominate industrial catalysts with an estimated 80% of catalytic processes using solid catalysts.[44] Solid catalysts are advantageous to homogenous catalysts owing to their ease in separations and non-corrosiveness, which can account for over half the initial equipment costs for fuel and chemical industries.[16] Using 2-methyltetrahydrofuran (2-MTHF) as the model compound, we have employed space time studies to study the reaction network as well as the factors that affect the activity of SiO_2/Al_2O_3 for the dehydration reaction. The relative stability of carbenium ions is highlighted as the key factor affecting the product selectivity. Experimentally calculated apparent activation energy to diene formation and the fractional order dependence on the reactant reveal the strong interaction of 2-MTHF with the catalyst surface. Importantly, for industrial applications, it is shown that the solid acid catalyst is regenerable with negligible loss in initial activity. Both

Brønsted and Lewis acid catalysts are shown to be active for 2-MTHF dehydration. In addition to 2-MTHF, ring opening of other cyclic ethers, namely, tetrahydropyran, tetrahydrofuran, and 2,5-dimethyltetrahydrofuran to their respective dienes is discussed.

In Chapter 5, the use of bimetallic catalysts and catalysts coated using atomic layer deposition is discussed to drive dehydrogenation of alkanes for their use as endothermic fuels. The interaction of alkanes with metal surfaces results in the formation of strongly held residues by deep dehydrogenation, polymerization or fragmentation into carbon species all of which lead to catalyst deactivation. During the dehydrogenation of ethane and isobutane, a variety of factors were noted to affect catalyst performance, such as the support, metal loadings, and hydrogen co-feed pressure. Thermogravimetric analysis and transmission electron microscopy were employed to study catalyst deactivation due to coke deposition and metal particle sintering. Addition of the promoter metal (e.g., tin) to the monometallic Pt catalyst was shown to lower the amount of coke per surface Pt atom. An enhancement in turnover frequency for alkene formation was observed upon alumina overcoating of a Pt/γ-Al_2O_3 catalyst.

X-ray absorption spectroscopy has emerged as a powerful tool for determining the catalyst nanoparticle structure and composition at an atomic level. Chapter 6 discusses the use of XAS to determine the local atomic environment, oxidation state, and particle size of catalysts for the following systems: carbon and silica-supported PtMo catalysts for water gas shift reaction, silica-supported AuMo catalysts for reverse water gas shift reaction, and carbon-supported RhRe catalysts for C-O hydrogenolysis of biomass-derived tetrahydropyran-2-methanol. Due to limitations in individual methods, a combination of catalyst characterization techniques is used to draw the catalyst structure. The structure-activity correlations are used to elucidate the nature of the active sites for these probe reactions.

In Chapter 7, recommendations are made for development of an integrated process to make dienes from lignocellulosic biomass as well as ideas for coupling of biomass-derived ethanol are proposed.

1.2. References

1. Christensen, C. H.; Rass-Hansen, J.; Marsden, C. C.; Taarning, E.; Egeblad, K., The renewable chemicals industry. ChemSusChem 2008, 1 (4), 283-289.
2. Nikolau, B. J.; Perera, M.; Brachova, L.; Shanks, B., Platform biochemicals for a biorenewable chemical industry. Plant J. 2008, 54 (4), 536-545.
3. Weissermel, K.; Arpe, H. J., Industrial Organic Chemistry. Wiley-VCH: 2008.
4. U.S. Energy Information Administration, International energy outlook 2016, DOE/EIA-0484(2016), U.S. Department of Energy; 2016.
5. British Petroleum Company, BP Statistical review of world energy, British Petroleum Co.; 2016.
6. Sheldon, R. A., The E Factor: fifteen years on. Green Chem. 2007, 9 (12), 1273-1283.
7. United Nations Intergovernmental Panel on Climate Change, Special Report on Renewable Energy Sources and Climate Change Mitigation; 2011.
8. Lacis, A. A.; Schmidt, G. A.; Rind, D.; Ruedy, R. A., Atmospheric CO2: Principal Control Knob Governing Earth's Temperature. Science 2010, 330 (6002), 356-359.
9. Fornasiero, P.; Graziani, M., Renewable Resources and Renewable Energy: A Global Challenge, Second Edition. CRC Press: 2006.
10. Alonso, D. M.; Bond, J. Q.; Dumesic, J. A., Catalytic conversion of biomass to biofuels. Green Chem. 2010, 12 (9), 1493-1513.
11. Wyman, C. E.; Dale, B. E.; Elander, R. T.; Holtzapple, M.; Ladisch, M. R.; Lee, Y. Y., Coordinated development of leading biomass pretreatment technologies. Bioresour. Technol. 2005, 96 (18), 1959-1966.
12. Langholtz, M. H.; Stokes, B. J.; Eaton, L. M. U.S. Department of Energy. 2016 Billion-Ton Report: Advancing Domestic Resources for a Thriving Bioeconomy, Volume 1: Economic Availability of Feedstocks, ORNL/TM-2016/160.; Oak Ridge National Laboratory, Oak Ridge, TN.: 2016; p 448.
13. Huber, G. W.; Dale, B. E., Grassoline at the Pump. Sci.Am. 2009, 301 (1), 52-56.
14. Jenkins, B. M.; Baxter, L. L.; Miles Jr, T. R.; Miles, T. R., Combustion properties of biomass. Fuel Processing Technology 1998, 54 (1–3), 17-46.
15. Vassilev, S. V.; Baxter, D.; Andersen, L. K.; Vassileva, C. G., An overview of the chemical composition of biomass. Fuel 2010, 89 (5), 913-933.
16. Rinaldi, R.; Schuth, F., Design of solid catalysts for the conversion of biomass. Energy Environ. Sci. 2009, 2 (6), 610-626.
17. de Wild, P. J.; den Uil, H.; Reith, J. H.; Kiel, J. H. A.; Heeres, H. J., Biomass valorisation by staged degasification A new pyrolysis-based thermochemical conversion option to produce value-added chemicals from lignocellulosic biomass. J. Anal. Appl. Pyrolysis 2009, 85 (1-2), 124-133.

18. Lange, J.-P., Lignocellulose conversion: an introduction to chemistry, process and economics. Biofuels, Bioproducts and Biorefining 2007, 1 (1), 39-48.
19. Sun, Y.; Cheng, J. Y., Hydrolysis of lignocellulosic materials for ethanol production: a review. Bioresour. Technol. 2002, 83 (1), 1-11.
20. Dhepe, P. L.; Fukuoka, A., Cellulose Conversion under Heterogeneous Catalysis. ChemSusChem 2008, 1 (12), 969-975.
21. Climent, M. J.; Corma, A.; Iborra, S., Heterogeneous Catalysts for the One-Pot Synthesis of Chemicals and Fine Chemicals. Chem. Rev. 2011, 111 (2), 1072-1133.
22. Wettstein, S. G.; Alonso, D. M.; Gurbuz, E. I.; Dumesic, J. A., A roadmap for conversion of lignocellulosic biomass to chemicals and fuels. Curr. Opin. Chem. Eng. 2012, 1 (3), 218-224.
23. Alonso, D. M.; Wettstein, S. G.; Mellmer, M. A.; Gurbuz, E. I.; Dumesic, J. A., Integrated conversion of hemicellulose and cellulose from lignocellulosic biomass. Energy Environ. Sci. 2013, 6 (1), 76-80.
24. Luterbacher, J. S.; Alonso, D. M.; Dumesic, J. A., Targeted chemical upgrading of lignocellulosic biomass to platform molecules. Green Chem. 2014, 16 (12), 4816-4838.
25. Dong, F.; Zhu, Y. L.; Ding, G. Q.; Cui, J. L.; Li, X. Q.; Li, Y. W., One-step Conversion of Furfural into 2-Methyltetrahydrofuran under Mild Conditions. ChemSusChem 2015, 8 (9), 1534-1537.
26. Roman-Leshkov, Y.; Barrett, C. J.; Liu, Z. Y.; Dumesic, J. A., Production of dimethylfuran for liquid fuels from biomass-derived carbohydrates. Nature 2007, 447 (7147), 982-U5.
27. Wettstein, S. G.; Bond, J. Q.; Alonso, D. M.; Pham, H. N.; Datye, A. K.; Dumesic, J. A., RuSn bimetallic catalysts for selective hydrogenation of levulinic acid to γ-valerolactone. Applied Catalysis B: Environmental 2012, 117–118 (0), 321-329.
28. Kunkes, E. L.; Simonetti, D. A.; West, R. M.; Serrano-Ruiz, J. C.; Gartner, C. A.; Dumesic, J. A., Catalytic conversion of biomass to monofunctional hydrocarbons and targeted liquid-fuel classes. Science 2008, 322 (5900), 417-421.
29. Kim, Y. T.; Dumesic, J. A.; Huber, G. W., Aqueous-phase hydrodeoxygenation of sorbitol: A comparative study of Pt/Zr phosphate and Pt-ReOx/C. J. Catal. 2013, 304, 72-85.
30. Sinfelt, J. H.; Yates, D. J. C.; Carter, J. L., Catalytic hydrogenolysis and dehydrogenation over Copper-Nickel alloys. J. Catal. 1972, 24 (2), 283-&.
31. Sinfelt, J. H., Bimetallic catalysts: discoveries, concepts, and applications. Wiley: 1983.
32. Biloen, P.; Dautzenberg, F. M.; Sachtler, W. M. H., Catalytic dehydrogenation of propane to propene over platinum and platinum-gold alloys. J. Catal. 1977, 50 (1), 77-86.
33. Sattler, J. J. H. B.; Gonzalez-Jimenez, I. D.; Luo, L.; Stears, B. A.; Malek, A.; Barton, D. G.; Kilos, B. A.; Kaminsky, M. P.; Verhoeven, T. W. G. M.; Koers, E. J.; Baldus, M.; Weckhuysen, B. M., Platinum-Promoted Ga/Al2O3 as Highly Active, Selective, and Stable Catalyst for the Dehydrogenation of Propane. Angewandte Chemie International Edition 2014, 53 (35), 9251-9256.
34. Sun, P.; Siddiqi, G.; Vining, W. C.; Chi, M.; Bell, A. T., Novel Pt/Mg(In)(Al)O catalysts for ethane and propane dehydrogenation. J. Catal. 2011, 282 (1), 165-174.
35. Ruppert, A. M.; Weinberg, K.; Palkovits, R., Hydrogenolysis Goes Bio: From Carbohydrates and Sugar Alcohols to Platform Chemicals. Angew. Chem.-Int. Edit. 2012, 51 (11), 2564-2601.
36. Chia, M.; Pagan-Torres, Y. J.; Hibbitts, D.; Tan, Q. H.; Pham, H. N.; Datye, A. K.; Neurock, M.; Davis, R. J.; Dumesic, J. A., Selective Hydrogenolysis of Polyols and Cyclic Ethers over

Bifunctional Surface Sites on Rhodium-Rhenium Catalysts. J. Am. Chem. Soc. 2011, 133 (32), 12675-12689.

37. Ketchie, W. C.; Murayama, M.; Davis, R. J., Selective oxidation of glycerol over carbon-supported AuPd catalysts. J. Catal. 2007, 250 (2), 264-273.
38. Della Pina, C.; Falletta, E.; Rossi, M., Highly selective oxidation of benzyl alcohol to benzaldehyde catalyzed by bimetallic gold-copper catalyst. J. Catal. 2008, 260 (2), 384-386.
39. Ponec, V., On the role of promoters in hydrogenations on metals; alpha,beta-unsaturated aldehydes and ketones. Appl. Catal. A-Gen. 1997, 149 (1), 27-48.
40. Bond, J. Q.; Alonso, D. M.; Wang, D.; West, R. M.; Dumesic, J. A., Integrated Catalytic Conversion of gamma-Valerolactone to Liquid Alkenes for Transportation Fuels. Science 2010, 327 (5969), 1110-1114.
41. Kim, Y. T.; Chada, J. P.; Xu, Z. R.; Pagan-Torres, Y. J.; Rosenfeld, D. C.; Winniford, W. L.; Schmidt, E.; Huber, G. W., Low-temperature oligomerization of 1-butene with H-ferrierite. J. Catal. 2015, 323, 33-44.
42. Bui, P.; Cecilia, J. A.; Oyama, S. T.; Takagaki, A.; Infantes-Molina, A.; Zhao, H. Y.; Li, D.; Rodriguez-Castellon, E.; Lopez, A. J., Studies of the synthesis of transition metal phosphides and their activity in the hydrodeoxygenation of a biofuel model compound. J. Catal. 2012, 294, 184-198.
43. Bui, P. P.; Oyama, S. T.; Takagaki, A.; Carrow, B. P.; Nozaki, K., Reactions of 2-Methyltetrahydropyran on Silica-Supported Nickel Phosphide in Comparison with 2-Methyltetrahydrofuran. ACS Catal. 2016, 6 (7), 4549-4558.
44. de Jong, K. P., Synthesis of Solid Catalysts. Wiley: 2009.

CHAPTER 2

Experimental Techniques

2.1. Introduction

This chapter contains experimental methods and techniques that are generally applicable throughout this thesis. Detailed experimental methods are discussed in the subsequent chapters whenever relevant.

2.2. Catalyst Synthesis and Preparation

2.2.1. Supported metal catalysts

Monometallic Pt catalysts studied in Chapter 5 were prepared both using incipient wetness impregnation and ion exchange. Bimetallic PtSn/SiO_2 and PtSn/K-L-Zeolite catalysts with varying Pt to Sn atomic ratios were synthesized via sequential impregnation. Where SiO_2, γ-Al_2O_3 and KLZ are mentioned as the supports, untreated fumed silica (Cabot, Cab-O-Sil®, EH5), γ-Al_2O_3 (Strem Chemicals) and K-doped LTL-Zeolite (Tosoh Corporation, $SiO_2/Al_2O_3 = 6$) were used, respectively. Monometallic Pt catalysts supported on SiO_2 and γ-Al_2O_3 were prepared by incipient wetness impregnation with aqueous solutions of tetraammineplatinum(II) nitrate precursor ($Pt(NH_3)_4(NO_3)_2$, Sigma-Aldrich) and hydrochloroplatinic acid hydrate ($H_2PtCl_6.xH_2O$, Sigma-Aldrich). Atomic layer deposition technique was employed to overcoat the Pt/γ-Al_2O_3 catalysts with alumina layer as described in the following section.

Platinum was added to SiO_2 by ion exchange method of Benesi *et al.* (Figure 2.1).[1] The extent of exchange was controlled by adjusting the pH of a $Pt(NH_3)_4(NO_3)_2$ and silica slurry with an aqueous, basic solution of $Pt(NH_3)_4(OH)_2$ (Strem Chemicals) over a course of 20 minutes. The resulting material was filtered, washed with deionized water, and dried overnight in air at 390 K. This catalyst was calcined in flowing air at 573 K for 2 h, reduced in flowing H_2 at 673 K and passivated at room temperature in flowing 2% O_2 in He. The actual Pt loading was determined using inductively coupled plasma atomic emission spectroscopy. PtSn/SiO_2 catalysts with set Pt:Sn atomic ratios were prepared by adding the appropriate amount of tin precursor into the parent Pt/SiO_2 catalyst. Tin was added to the Pt/SiO_2 catalyst by evaporative impregnation of a solution of tributyltin acetate ($CH_3CO_2Sn[(CH_2)_3CH_3)]_3$, Strem Chemicals) in pentane. The catalyst was then dried overnight at 390 K, treated with flowing oxygen at 573 K for 2 h, followed by reduction at 773 K in flowing hydrogen for 2 h and passivated at room temperature in flowing 2% O_2 in He.

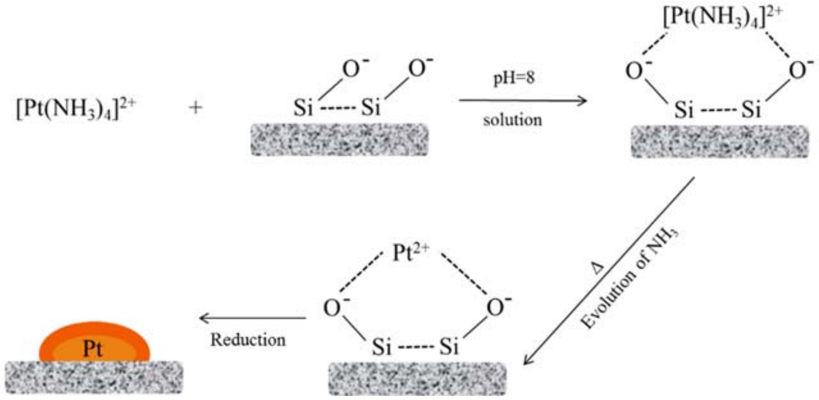

Figure 2.1. Ion exchange protocol using the Benesi method to achieve high metal dispersion.[1]

Prior to the addition of Pt, the K-L-Zeolite was first baked in dry air at 873 K for 18 h to remove all the chemisorbed water.[2] Pt was impregnated onto KLZ using a solution of $Pt(NH_3)_4(NO_3)_2$ in DI water under inert atmosphere. Tin was incorporated in the same way using tributyltin acetate as the precursor. The routine of calcination-reduction-passivation followed as mentioned for the SiO_2-supported catalyst. The hydrotalcite (Mg/Al = 3, Sigma Aldrich) was decomposed in flowing air at 773 K overnight to obtain the corresponding Mg-Al mixed oxides ($MgAl_xO_y$).

Supported PtMo and AuMo catalysts characterized using X-ray absorption spectroscopy were prepared using controlled surface reactions described elsewhere.[3] For the carbon-supported RhRe samples, monometallic and bimetallic catalysts were prepared by incipient wetness impregnation of the Norit Darco and Vulcan carbon supports with aqueous solutions of

$RhCl_3.xH_2O$ (Sigma Aldrich) and NH_4ReO_4 (Sigma Aldrich). A detailed description of the synthesis of the aforementioned catalysts can be found in Chapter 6.

Amorphous SiO_2/Al_2O_3 (13.7 wt% alumina content) obtained from Grace Davison (Grade 135) was used for dehydration of alcohols present in the effluent from aqueous phase hydrodeoxygenation of sorbitol and ring opening of various heterocyclics to dienes. The catalyst was calcined *ex situ* at 773 K (4.2 K min^{-1}, 2 h) in flowing air (Airgas, 50 cm^3 min^{-1}). ZSM-5 (Zeolyst International; CBV 2314, CBV 5524G, CBV 8014; $SiO_2/Al_2O_3 = 23, 50, 80$, respectively), Mordenite (Zeolyst International; CBV 21A; $SiO_2/Al_2O_3 = 20$), and Zeolite Beta (Zeolyst International; CP814E; $SiO_2/Al_2O_3 = 25$) were purchased in the ammonium form and converted to the proton form by calcination in flowing air for 5 h at 823 K (1 K min^{-1}). The other solid acids namely γ-Al_2O_3 (Strem Chemicals), Al-Sn-Beta (Al-Sn-BEA, Si/Sn=200, Si/Al= 50, Haldor Topsøe A/S, Denmark), $NbOPO_4$, and Nb_2O_5 (CBMM, Brazil) were used directly without any pretreatment.

2.2.2. Atomic layer deposition

The overcoated catalysts were prepared using atomic layer deposition (ALD) in a fluidized bed reactor described elsewhere.[4] Nitrogen was used as a carrier gas, with the pressure in the reactor varying between 4.5 and 6.0 Torr during depositions. The bed velocity was sufficient for fluidization of particles throughout the deposition process. The substrates were held in the reactor at deposition temperature and pressure for 2 h under a dry nitrogen stream before each deposition. The ALD processes were monitored *in situ* using a Residual Gas Analyzer quadrupole mass spectrometer (RGA) downstream of the deposition chamber. The RGA chamber was pumped differentially through a 40 μm orifice giving a pressure of $2x10^{-5}$ Torr in the analysis chamber.

Trimethylaluminum (TMA, 97% purity from Sigma Aldrich) was used as the precursor compound for alumina overcoats. TMA was held in a bubbler at room temperature and fed through a metering valve to give a partial pressure of 1 Torr. Deionized water was kept in a bubbler held in a cooling bath at 280 K and fed through a metering valve. Depositions were performed at 303 K using sequential pulses separated by 10 min purges of inert carrier gas. The pulse sequence used was: TMA - Purge - H_2O - Purge as depicted in Figure 2.2. This sequence of four steps denotes one ALD cycle. Precursor pulse lengths were determined using the RGA by observing the methyl ion (m/z = 15) of the reaction byproduct CH_4. Surface reactions resulted in a sharp increase in byproduct concentration, followed by a decrease when saturation had occurred. An automated LabVIEW program was used to terminate pulses when the byproduct partial pressure fell to 45% of its peak level for the first three pulses. The subsequent pulses lengths were fixed at the duration recorded by the program during the third pulse. The catalysts with alumina overcoat studied in Chapter 5 are named by the number of ALD cycles, followed by the ALD substrate. For example, a Pt/γ-Al_2O_3 catalyst overcoated with x cycles of TMA/H_2O ALD is named xALD/Pt/γ-Al_2O_3.

For synthesizing hydrothermally stable catalysts described in Chapter 3, overcoats of titania and zirconia were deposited onto γ-Al_2O_3 substrate. For titania ALD, titanium tetrachloride ($TiCl_4$, 99.9% purity from Sigma Aldrich) was held in a bubbler maintained at 290 K with a 50 cm^3 min^{-1} nitrogen stream diverted through the bubbler to carry the precursor. Deionized water was kept in a bubbler held in a cooling bath at 280 K and fed through a metering valve. Depositions were performed at 423 K using sequential pulses of metal organic precursor and water under a pressure of 1-2 Torr and separated by 10 min purges of inert carrier gas.

For zirconia ALD onto alumina substrate, tetrakis(dimethylamido)zirconium ($Zr(NMe_2)_4$) (TDMAZ, Strem Chemicals) and deionized water were used as precursors for Zr and O, respectively. Ultra-high purity nitrogen gas (Airgas) was used for purging the reactor in between precursor pulses. The TDMAZ bubbler was heated to 353 K to increase its vapor pressure and a nitrogen flow of 50 cm^3 min^{-1} was maintained through the bubbler to entrain the precursor.[5] The deposition was executed out at 473 K and at pressure of 1 Torr. The substrate was coated using the TDMAZ – Purge - H_2O - Purge pulse sequence. The pulse and purge times 150-180 seconds for the precursors were selected based on the completion of half-cycle surface reactions, as monitored by the decrease in the RGA signal intensity. The nomenclature for titania and zirconia overcoated catalysts is similar to that described for alumina ALD.

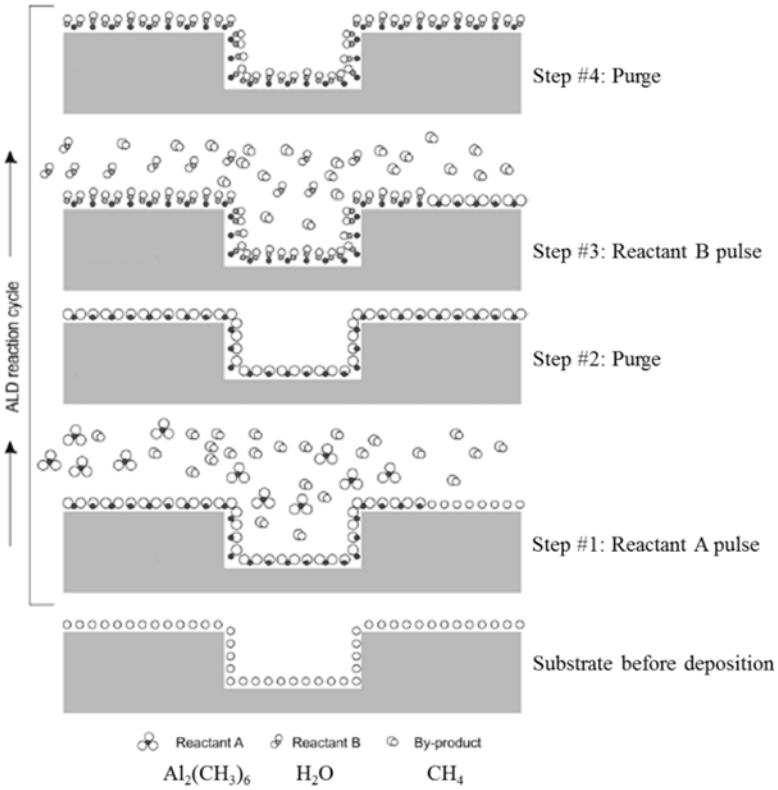

Figure 2.2. Schematic of an ALD reaction cycle (Adapted from Puurunen[6]).

2.3. Catalyst Characterization

2.3.1. CO chemisorption

The surface Pt sites for the Pt and PtSn catalysts studied in Chapter 5 were determined using their CO uptake at 308 K measured using an ASAP 2020C (Micromeritics) after reduction of the catalyst at 773 K (0.5 K min^{-1}) for 2 h. The number of catalytic sites was taken to be equal to the irreversible CO uptake at this temperature and the dispersion was calculated accordingly. The average metal particle size was determined using the equation for atomic density of (111) plane ($d_p = \frac{1.1}{\text{Dispersion}}$, where d_p is the particle diameter in nm)

2.3.2. N_2 physisorption

The Brunauer-Emmett-Teller (BET) surface area was obtained from the nitrogen physisorption isotherms recorded at liquid nitrogen temperature (77 K) using a volumetric adsorption unit (Micromeritics, ASAP 2020). The catalysts were degassed at 423 K in vacuum for 6 h prior to the measurements. The Barrett-Joyner-Halenda (BJH) method were used to determine pore size and volume.

2.3.3. Inductively coupled plasma atomic emission spectroscopy

A Perkin-Elmer Plasma 400 ICP Emission Spectrometer was used to quantify the metal content of the supported metal catalyst. The catalyst metal loading in the reduced supported metal samples was analyzed by dissolving the metal from the support using aqua regia. The metal digestion was performed in 10 mL thick-walled reactors (Alltech) with a triangular stir bar and a cap liner. The reactor was immersed in an oil bath set at the desired temperature. The ICP instrument was calibrated for the desired concentration range using standard solutions for the metal of interest.

2.3.4. Thermogravimetric Analysis

Thermogravimetric analysis (TGA) was conducted using a TA Instruments Q500 system. To determine the amount of coke deposited on the catalysts studied in Chapters 3, 4, and 5, approximately 20 mg of the sample was loaded onto a Pt pan. The loss in weight was tracked as the temperature was raised from room temperature to 1073 K in 80 cm^3 min^{-1} O_2 flow with 10 K min^{-1} ramp rate.

2.3.5. Electron microscopy and spectroscopy

The particle size and composition distributions were obtained using scanning transmission electron microscopy (STEM) and energy dispersive x-ray spectroscopy (EDS) respectively. STEM imaging was performed using a FEI Titan STEM with Cs aberration correction operated at 200 kV in high-angle annular dark field (HAADF) mode. EDS data was collected using the same microscope with an EDAX SiLi detector. Catalyst samples were suspended in ethanol, sonicated for 5 min, and then deposited onto a holey carbon Cu TEM grid. STEM samples were plasma cleaned for 10 min with 20% O_2 in argon gas mixture immediately before being loading into the microscope. From the particle size distribution, the number average particle size was determined using the relation $d = \sum_i \frac{d_i}{n}$, where d_i is the particle diameter of each nanoparticle, n is the total number of nanoparticles counted for a given sample, and the summation was performed over all the particles identified in the STEM images.

2.3.6. X-ray absorption spectroscopy

For silica supported Pt and PtSn catalysts, Pt L_{III}-edge (11.564 keV) X-ray absorption spectroscopy (XAS) measurements were conducted at beamline 12-BM at the Advanced Photon Source (APS) at Argonne National Laboratory. A double crystal of Si(111) was used as a monochromator. X-ray absorption near-edge spectroscopy (XANES) data were collected at the Pt in the fluorescence mode at room temperature using a 13 elements germanium detector. The energy was calibrated using a Pt foil.

We investigated the structure-property relationships for carbon and silica-supported PtMo catalysts for water gas shift reaction. The XAS measurements for these catalysts were conducted in transmission mode at beamline 10-BM-B at the APS. For the AuMo samples, the XANES data was collected in both transmission and fluorescence mode at Sector 12-BM-B. The carbon-supported RhRe catalysts for hydrogenolysis of tetrahydropyran-2-methanol were scanned at Sector 20-BM-B in transmission mode. The detailed description can be found in Chapter 6. Briefly, the catalysts were reduced in a continuous-flow reactor, which consisted of a quartz tube (1 inch OD, 10 inch length) sealed with Kapton windows by two Ultra-Torr fittings. Ball valves were welded to each Ultra-Torr fitting and served as the gas inlet and outlet. A K-type thermocouple was placed internally against the catalyst sample holder to monitor temperature. Catalyst samples were pressed into the cylindrical sample holder consisting of six wells, each forming a self-supporting wafer. The amount of catalyst was added to give an absorbance (μx) of approximately 1.0. The catalysts were reduced in flowing 3.5% H_2 in He (50 cm^3 min^{-1}) at 573 K, purged with flowing He at 573 K for 10 min and then cooled to room temperature. XAS spectra were collected in He at room temperature for the reduced samples. All the XAS analysis was performed using Athena and WinXAS softwares.[7,8]

2.3.7. NH_3 and isopropylamine temperature programmed desorption

The total and Brønsted acid site densities on the catalyst were estimated using ammonia temperature-programmed desorption (NH_3-TPD) and isopropylamine temperature-programmed desorption (IPA-TPD), respectively, using Micromeritics, Autochem II 2920. Approximately 100 mg of sample was loaded in a quartz cell and pretreated in He at 773 K. For NH_3 adsorption, the sample was cooled to 423 K after pretreatment, saturated with NH_3 for 1 h and then flushed with He for 1 h to remove the physisorbed ammonia. The TPD was performed using a temperature ramp of 10 K min^{-1} from 423 K to 973 K under flowing He. The amount of ammonia desorbed was calculated by integrating the thermal conductivity detector signal. For IPA-TPD, the IPA was dozed in pulses over the sample at 323 K until saturation after which the cell was purged with He for 1 h. During TPD, the propene evolved via IPA decomposition was quantified to determine the Brønsted acid site density.

2.3.8. Powder X-ray diffraction

The bulk crystalline structure of the catalysts was determined by X-ray diffraction (XRD). The XRD patterns were obtained with a high-resolution Bruker D8 Discover diffractometer using Cu Kα radiation ($\lambda = 0.15406$ nm), operated at 50 kV and 1000 mA (2.0 kW) at a scan rate of 0.1 (2θ) s^{-1}. Crystal phases were identified using Inorganic Crystal Structure Database (ICSD).

2.4. Reaction Studies and Analysis

2.4.1. Continuous flow reaction studies

The dehydrogenation of alkanes was studied in the down flow reactor using one quarter to one half inch stainless steel tube reactors. The experiments were performed in the temperature range of 723-873 K and pressure of 1 atm with He (Airgas) as a carrier gas. The flow rates were controlled using Brooks mass flow controllers and for temperature control, PID controller (Love Controls) with a K-type thermocouple (Omega) was used. Before each reaction, the catalyst was reduced in flowing H_2 at 773 K for 1 h and then brought to the reaction temperature before feeding the reactant gas mixture. Identification of products in the gas phase was performed using a gas chromatograph-mass spectrometer (Shimadzu Corp., GCMS-QP2010S) equipped with a SHRXI-5MS capillary column (30 m × 0.25 mm × 0.25 μm). Quantitative analyses were performed for this gas phase reaction using a gas chromatograph (Shimadzu Corp., GC-2014) equipped with a FID detector with a Rt®-Alumina BOND/MAPD (50 m × 0.53 mm × 10 μm) capillary column (Restek), and a TCD detector with a HaySep DB 100/120 packed column (Alltech). The effluent from the reactor was fed straight into this GC, thus maintaining a real-time operation. This was an advantage given the time scale of deactivation of catalyst.

The dehydration of alcohols to olefins and the ring opening of various heterocyclics to dienes was studied in gas-phase in a fixed-bed down-flow reactor (Figure 2.3) under atmospheric pressure. Half-inch and quarter-inch stainless steel tubing was used as reactors and the catalyst was packed in a between plugs of quartz wool and quartz beads. The reactor was filled to the top of the heating zone with fused SiO_2. A well-insulated furnace (Applied Test Systems) was used as the heat source and aluminium blocks were used around the reactor and to ensure isothermal operation. Reactor temperature was monitored at the reactor wall using a K-type thermocouple (Omega) and 16A series programmable PID controller (Love Controls, Series 16A) connected to a variable transformer (Staco Energy Products). The feed was pumped from a graduated measuring cylinder into the reactor using an HPLC pump (Lab Alliance Series I). Helium (Airgas) was used as the carrier gas and the flow rates were adjusted using a mass flow controller (Brooks Instruments).

For the first set of reactions using dodecane as the solvent, 1-20 wt% of 2-MTHF in dodecane was introduced in the reactor using an HPLC pump. Helium was used as the carrier gas and the total gas flow rate out of the system was measured using a bubble meter. The reactor effluent was passed to a gas-liquid separator immersed in an ice-water bath to ensure that condensation of low-boiling products does not take place in the tubing connected to the gas GC. Gas-phase products were purged from the separator by flowing He and were analysed using an online GC-FID (Agilent GC6890) equipped with a GSQ-PLOT column (Agilent) and a GC-TCD (Shimadzu) equipped with a HaySep DB 100/120 column (Alltech) using He as the reference gas to detect CO and CO_2. Periodic liquid drains were collected from the separator throughout the duration of the experiment and injected in a GC-2014 (Shimadzu) with a Rtx-VMS column (Restek). Both the gas and liquid products were identified using a GC-MS (Shimadzu, QP-2010). Same columns (Rtx-VMS) were installed in both the GC and GC-MS for ease of identification of compounds. Catalyst regeneration was achieved by calcining the catalysts at 773 K (4 K min^{-1}, 2 h hold) in flowing air. CO_2 evolution was monitored using a GC-TCD. The CO_2 peak area increased with temperature and eventually decreased to zero suggesting that coke removal was complete.

For the second set of reactions without using any solvent, low flow rates of the cyclic ethers were achieved using a syringe pump (Harvard Apparatus, PHD Ultra) and helium was used as a carrier gas. The gas-liquid separator was bypassed and all the lines from the reactor to the gas GC were heat traced and were maintained at 423 K to prevent condensation of the products and reactants. The gas products were analysed continuously throughout the experiment. The products were analysed by an online GC equipped with a barrier discharge ionization detector (GC-BID, Shimadzu) with a Rt-Q-BOND column (Restek).

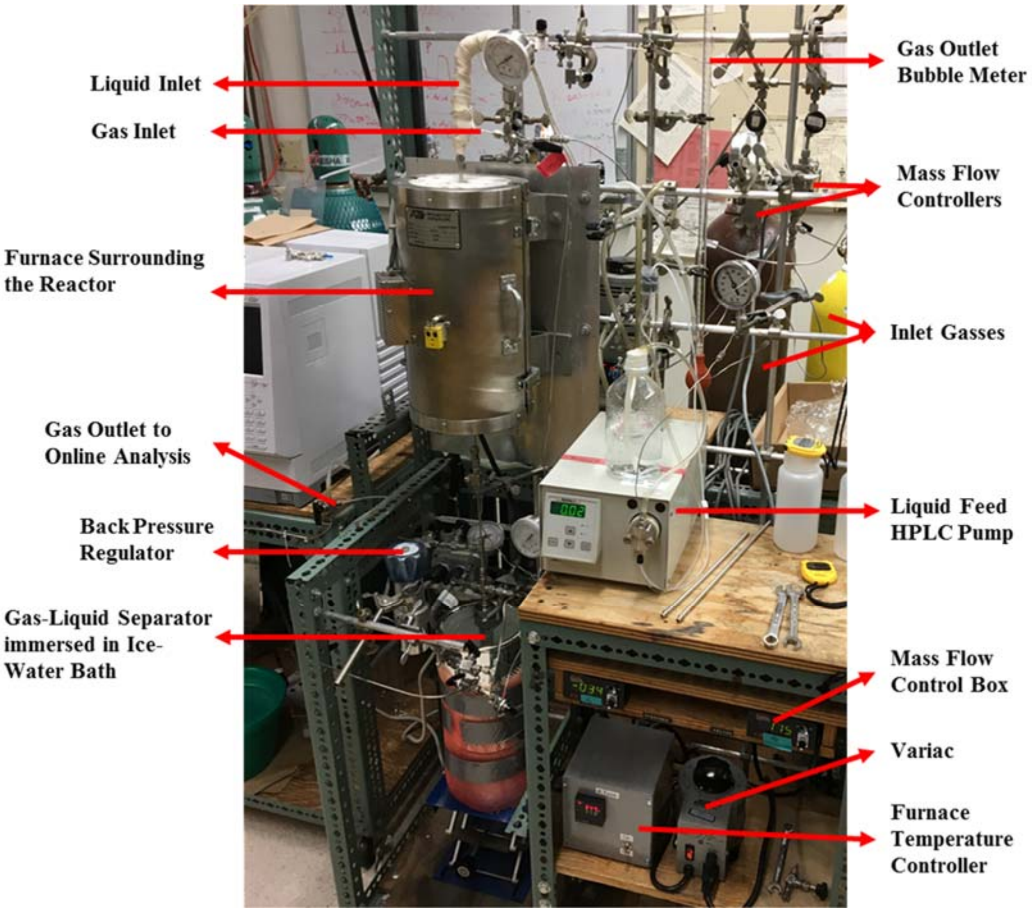

Figure 2.3. Continuous flow reactor used for dehydration of alcohols and cyclic ethers to monoalkenes and dienes.

Conversion, selectivity, yield, and weight hourly space velocity (WHSV) are defined as below (Equations (2.1) to (2.4)) and will be used throughout the thesis.

$$\text{Conversion} = \frac{\text{moles of carbon in the reactant converted}}{\text{moles of carbon in the reactant fed}} \times 100\% \tag{2.1}$$

$$\text{Carbon Selectivity} = \frac{\text{moles of carbon in the product}}{\text{moles of carbon in the reactant converted}} \times 100\% \tag{2.2}$$

$$\text{Carbon Yield} = \frac{\text{moles of carbon in the product}}{\text{moles of carbon in the reactant fed}} \times 100\% \tag{2.3}$$

$$\text{WHSV (h}^{-1}\text{)} = \frac{\text{reactant flow rate (g h}^{-1}\text{)}}{\text{mass of catalyst (g)}} \tag{2.4}$$

2.4.2. Batch reaction studies

Batch reactions were performed using a 50 mL pressure vessel (Figure 2.4, Parr Instrument, Model 4790) placed inside a chemical fume hood. The catalyst and a magnetic stir bar were loaded into the reactor, the vessel was sealed, pressurized and depressurized with He three times to displace the air in the reactor, and finally pressurized with H_2 for catalyst reduction. The reactor was cooled to room temperature post reduction and the reactants were pumped in using a high performance liquid chromatography (HPLC) pump. The temperature was raised to the reaction temperature and the reaction was carried for a set time period. Homogeneity of the reactor contents was achieved via magnetic stirring.

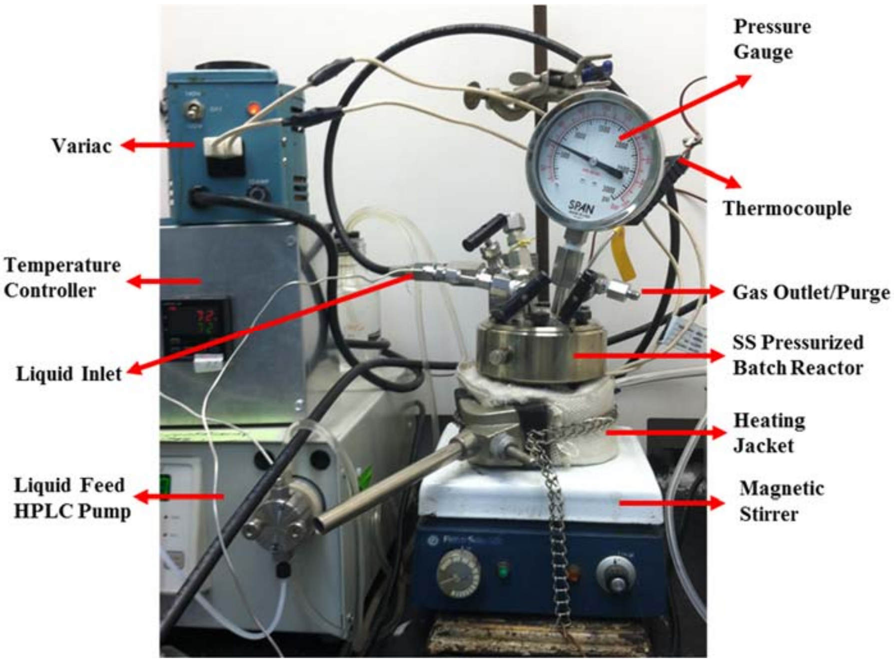

Figure 2.4. Parr Instrument pressure reactor used for batch reactions.

After the reaction, the reactor was slowly depressurized, the liquid product was separated from the catalyst using a syringe filter and the product was then analyzed using GC or HPLC. The gas phase products, if any, were collected in a gas bag and injected in a GC-MS using microneedle for qualitative analysis. The hydrothermal treatments for zirconia and titania overcoated catalysts described in Chapter 3 were performed using batch reactors at 473 K.

2.5. References

1. Benesi, H. A.; Curtis, R. M.; Studer, H. P., Preparation of highly dispersed catalytic metals - Platinum supported on silica gel. J. Catal. 1968, 10 (4), 328.
2. Cortright, R. D.; Dumesic, J. A., L-zeolite-supported platinum and platinum/tin catalysts for isobutane dehydrogenation. Appl. Catal. A-Gen. 1995, 129 (1), 101-115.
3. Hakim, S. H.; Sener, C.; Alba-Rubio, A. C.; Gostanian, T. M.; O'Neill, B. J.; Ribeiro, F. H.; Miller, J. T.; Dumesic, J. A., Synthesis of supported bimetallic nanoparticles with controlled size and composition distributions for active site elucidation. J. Catal. 2015, 328, 75-90.
4. Wiedmann, M. K.; Jackson, D. H. K.; Pagan-Torres, Y. J.; Cho, E.; Dumesic, J. A.; Kuech, T. F., Atomic layer deposition of titanium phosphate on silica nanoparticles. J. Vac. Sci. Technol. A 2012, 30 (1).
5. Hausmann, D. M.; Kim, E.; Becker, J.; Gordon, R. G., Atomic layer deposition of hafnium and zirconium oxides using metal amide precursors. Chem. Mat. 2002, 14 (10), 4350-4358.
6. Puurunen, R. L., Surface chemistry of atomic layer deposition: A case study for the trimethylaluminum/water process. J. Appl. Phys. 2005, 97 (12).
7. Ravel, B.; Newville, M., Athena, Artemis, Hephaestus: data analysis for X-ray absorption spectroscopy using IFEFFIT. J. Synchrot. Radiat. 2005, 12 (4), 537-541.
8. Ressler, T., WinXAS: a program for X-ray absorption spectroscopy data analysis under MS-Windows. J. Synchrot. Radiat. 1998, 5, 118-122.

CHAPTER 3

Upgrading of Monofunctional Intermediates obtained from Aqueous-Phase Hydrodeoxygenation of Biomass-Derived Carbohydrates

3.1. Introduction

Pyrolysis oils are low quality fuels which cannot be used in conventional gasoline or diesel engines largely due to their high oxygen contents. Upgrading strategies for deoxygenation of pyrolysis oils are imperative for their use in transportation fuels. In this chapter, we describe a multi-step catalytic process (Figure 3.1) for conversion of levoglucosan (LGA), a major anhydrosugar present in pyrolysis oil,[1-3] to monofunctional compounds, which can subsequently be coupled with various C-C coupling reactions to obtain distillate range molecules.

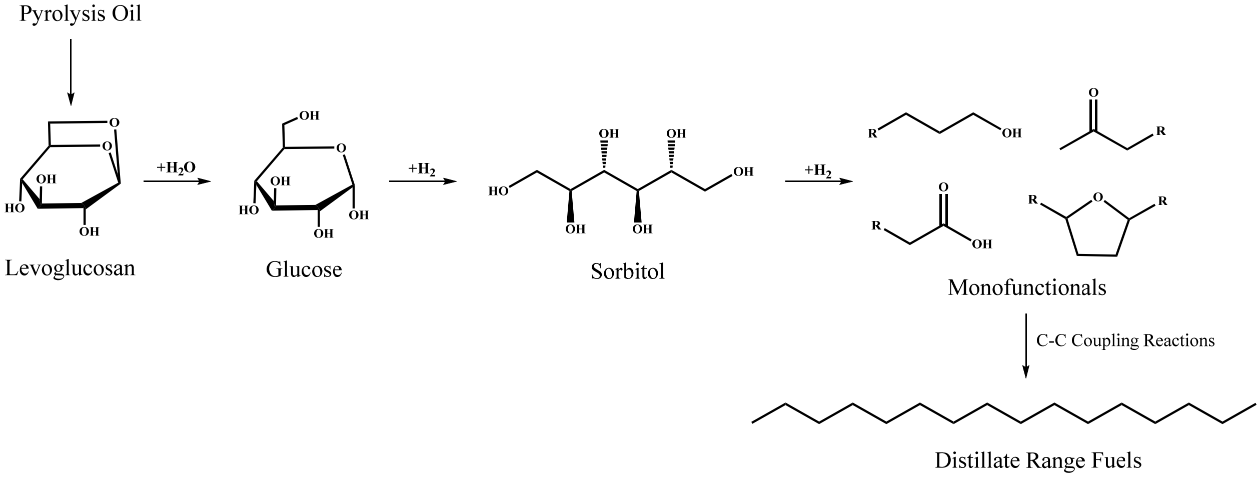

Figure 3.1. Pathway to convert levoglucosan to distillate range fuels.

Sugar syrups produced via the pyrolysis of red oak pyrolysis oil are rich in LGA.[4] This LGA can be converted to sorbitol with a two-step process. Firstly, LGA is hydrolyzed to glucose using acid catalysts.[5] Following hydrolysis, glucose is converted to sorbitol in near quantitative yield using metal catalysts such as Ru/C.[6,7] Sorbitol is converted into monofunctional intermediates such as alcohols, aldehydes, ketones, carboxylic acids, and heterocyclics containing 1-6 carbons and 1-2 oxygen atoms via aqueous-phase hydrodeoxygenation (APHDO) over catalysts such as PtRe/C and PdAg/WO_x-ZrO_2.[8-10] The conversion of sorbitol into jet and diesel fuel range molecules has been widely studied.[8,9,11-13] Various chemistries are used for conversion of monofunctional intermediates into distillate range molecules. Aldehydes and ketones can undergo aldol condensation resulting in the formation of heavier ketones.[11,12,14] Ketonization of carboxylic acids leads to the formation of higher ketones which can be further deoxygenated.[15,16] Heterocyclics can be converted to alcohols over supported bimetallic catalysts containing reducible metal and oxophilic promoter.[17,18] Alcohols can either be dehydrogenated to produce aldehydes which can undergo aldol condensation or can be dehydrated to produce olefins which can be oligomerized resulting in the formation of hydrocarbons with higher carbon number.[19]

In our current work, the monofunctional intermediates are produced using the APHDO of sorbitol with carbon yields up to 56% over Co/TiO_2.[20] These monofunctional species consist mainly of alcohols (69% of the carbon in monofunctionals) and heterocyclic species (23% of the carbon in monofunctionals). The majority of these species (52%) are C_5 or C_6 compounds, and only small amounts of ketones and acids are formed. The monofunctionals (mainly alcohols) can be converted to distillate range molecules via a C-C bonding formation step either by dehydration step to form olefins followed by olefin oligomerization or a dehydrogenation step to form aldehydes followed by an aldol condensation step. Recently, Kozlowski and Davis have reviewed the Guerbet coupling of alcohols over mixed metal oxides, metal phosphates, and supported transition metals such as copper.[21] Guerbet coupling involves four fundamental chemistries: dehydrogenation of alcohol to aldehyde, aldol condensation of the aldehyde followed by dehydration and hydrogenation to result in formation of the coupled alcohol. Within the reaction conditions probed for ethanol condensation over $Cu/MgAl_xO_y$, we did not achieve high yield to the C-C coupled products. The dehydration of alcohols to olefins and subsequent oligomerization was chosen as the route for upgrading the monofunctionals. Since the mid-1960s, dehydration of alcohols to olefins and ethers in gas-phase as well as in high-water environments has been studied over various solid acid catalysts.[22-25]

In this chapter, firstly, we have studied the dehydration of linear alcohols such as ethanol and 1-hexanol over crystalline H-ZSM-5, amorphous SiO_2/Al_2O_3, a Lewis acid γ-Al_2O_3, and a mixed oxide $MgAl_xO_y$ at 548 K and 1 atm. The objective of this study was to find the catalyst that showed high selectivity towards the desired olefin (intramolecular dehydration) and minimal selectivity towards the undesired ether (intermolecular dehydration). The reaction network for alcohol dehydration was determined using weight hourly space velocity studies. The study also sought to identify a catalyst stable under gas-phase dehydration conditions. Secondly, we investigated the conversion of a simulated feed representing the product mixture from the sorbitol APHDO effluent to establish the optimal reaction conditions for maximizing olefin yield. Lastly, the conversion of actual sorbitol APHDO effluent was performed to gain understanding of feeding various functionalities at the same time over the solid acid catalyst. Along with monoalkenes produced from the dehydration of alcohols, we observed the formation of dienes which are proposed to originate from the heterocyclics present in the feed mixture. The monoalkenes and dienes together can be subsequently oligomerized over solid acids to produce distillate range hydrocarbons.

3.2. Materials and Methods

3.2.1. Catalyst preparation

Carbon supported PdCe (5 wt% Pd, 0.7 wt% Ce, Pd:Ce = 1:0.1) and RuCe (5 wt% Ru, 0.7 wt% Ce, Ru:Ce = 1:0.1) catalysts were prepared by sequential addition of metal precursors using incipient wetness impregnation. Palladium(II) nitrate dihydrate (Sigma Aldrich), ruthenium(III) nitrosylnitrate (Alfa Aesar), cerium(III) nitrate hexahydrate (Acros Organics) were used as precursors for Pd, Ru, and Ce, respectively. The PdCe catalyst was obtained by successive impregnation of dried, unreduced Pd/C with aqueous solution of cerium(III) nitrate hexahydrate. The catalysts were dried in air at 383 K, reduced in flowing hydrogen at 723 K, and passivated with flowing 1% O_2 in Ar at room temperature. Supported Cu catalysts, Cu/CeO_2 (4 wt% Cu) and Cu/$MgAl_xO_y$ (5 wt% Cu), were prepared by incipient wetness impregnation using aqueous solution of copper(II) nitrate (Sigma Aldrich). Commercial layered hydrotalcite (Sigma Aldrich, Mg/Al = 3) was calcined in air at 773 K to obtain the mixed oxide, $MgAl_xO_y$. The catalysts were dried in air at 383 K, reduced in flowing hydrogen at 673 K, and passivated with flowing 1% O_2 in Ar at room temperature. The overcoated catalysts- 10ZrO_x/SiO_2, 5TiO_2/γ-Al_2O, and 15TiO_2/γ-Al_2O_3 were synthesized using atomic layer deposition as described in Chapter 2.

ZSM-5 (Zeolyst International; CBV 2314, $SiO_2/Al_2O_3 = 23$) was studied for dehydration of ethanol and 1-hexanol. The zeolite was purchased in the ammonium form and converted to the proton form by calcination in air for 5 h at 823 K (1 K min^{-1}). Amorphous SiO_2/Al_2O_3 (13.7 wt% alumina content) was obtained from Grace Davison (Grade 135) and it was calcined *ex situ* at 773 K (4.2 K min^{-1}, 2 h) in flowing air (Airgas, 50 cm^3 min^{-1}) before use. The Lewis acid, γ-Al_2O_3 (Strem Chemicals), was used directly without any pretreatment. All the catalysts were pretreated in He at 773 K for 2 h before each reaction.

3.2.2. Catalyst activity studies

The vapor-phase dehydration of pure ethanol (EtOH, Sigma Aldrich) was studied in a fixed-bed down-flow reactor at temperatures varying from 548 to 623 K and atmospheric pressure. The same setup was used for studying the dehydration of 1-hexanol (1-HexOH, Sigma Aldrich), the simulated feed, and the actual sorbitol APHDO effluent. Half-inch and quarter-inch stainless steel tubing was used for reactors and the catalyst was packed in a between plugs of quartz wool and quartz beads. A well-insulated furnace (Applied Test Systems) was used as the heat source and aluminium blocks were used around the reactor to ensure isothermal operation. Reactor temperature was monitored at the reactor wall using a K-type thermocouple (Omega) and 16A series programmable PID controller (Love Controls). Pure ethanol was pumped from a graduated measuring cylinder into the reactor using an HPLC pump (Lab Alliance Series I). Helium (Airgas) was used as the carrier gas and the flow rates were adjusted using a mass flow controller (Brooks Instruments). The reactor effluent was diverted to a gas-liquid separator immersed in an ice-water bath to ensure that condensation of low-boiling products does not take place in the tubing connected to the gas GC. Gas-phase products were purged from the separator by flowing He and were analysed using an online GC-FID (Agilent) and a GC-2014 (Shimadzu) equipped with a TCD using He as the reference gas. Periodic liquid drains were collected from the separator and injected in a GC-2014 (Shimadzu). For high conversion reactions, the liquid drains were biphasic. The organic and aqueous phases were separated using a separatory funnel and their masses and volumes were noted. The GC sensitivities for products were determined by making standards in both phases individually. Both the gas and liquid products were identified using a GC-MS (Shimadzu, QP-2010). The preliminary ethanol condensation reactions were performed in a Parr reactor at 523 K. The hydrothermal stability of ALD overcoated catalysts was studied in a Parr reactor at 473 K and 28 bar pressure.

3.3. Results and Discussion

3.3.1. Deoxygenation of model monofunctional compounds

3.3.1.1. C-C Coupling of ethanol

The condensation of ethanol was carried out in a batch reactor at 523 K and 100 psi initial hydrogen pressure. We synthesized PdCe/C, RuCe/C, and Cu/CeO_2 catalysts using the traditional incipient wetness impregnation method. A 25 mL solution of 5 wt% ethanol in cyclohexane was loaded in a Parr reactor with 0.3 g of catalyst. The autogenous pressure at the reaction temperature was 650 psi. The products obtained after a 6 h reaction are listed in Table 3.1. The desired C-C coupled product, 2-butanone, was observed over Cu/CeO_2 but it was only a minor product. The batch reactor studies were only qualitative. Ethanol condensation was further studied in a flow reactor to obtain quantitative data for determining the reaction pathway.

Table 3.1. Products formed during the qualitative batch reactor studies for ethanol condensation.

Catalyst	Major Product	Minor Product
PdCe/C	Diethyl ether	2-ethoxy propane, Ethyl acetate
RuCe/C	Methane	Acetone, Ethyl acetate
Cu/CeO_2	Ethyl acetate	Acetaldehyde, 2-butanone

Previous work on alcohol condensation by Iglesia *et al.* and Davis *et al.* showed that mixed oxides with strong base sites and weak acid sites coupled with a metal site for dehydrogenation/hydrogenation of intermediates resulted in high activity and selectivity towards the C-C coupled products.[21,26] Thus, we studied gas-phase ethanol coupling over a Cu/$MgAl_xO_y$ catalyst in an up-flow fixed bed reactor at 573 K and 1 atm. The equilibrium conversion of ethanol to acetaldehyde under the reaction conditions was calculated to be 94%. The catalyst deactivated with time on stream with ethanol conversion decreasing from 53% to 8% in 7 h (Figure 3.2(a)). The selectivity towards acetaldehyde was around 90% during the reaction. Among other products, the ethene selectivity increased with decreasing selectivities towards ethyl acetate and 1-butanol as seen in Figure 3.2(b). Thus, Cu/$MgAl_xO_y$ was active but not selective for the formation of the C-C coupled product, 1-butanol formed via aldol condensation/Guerbet reaction.

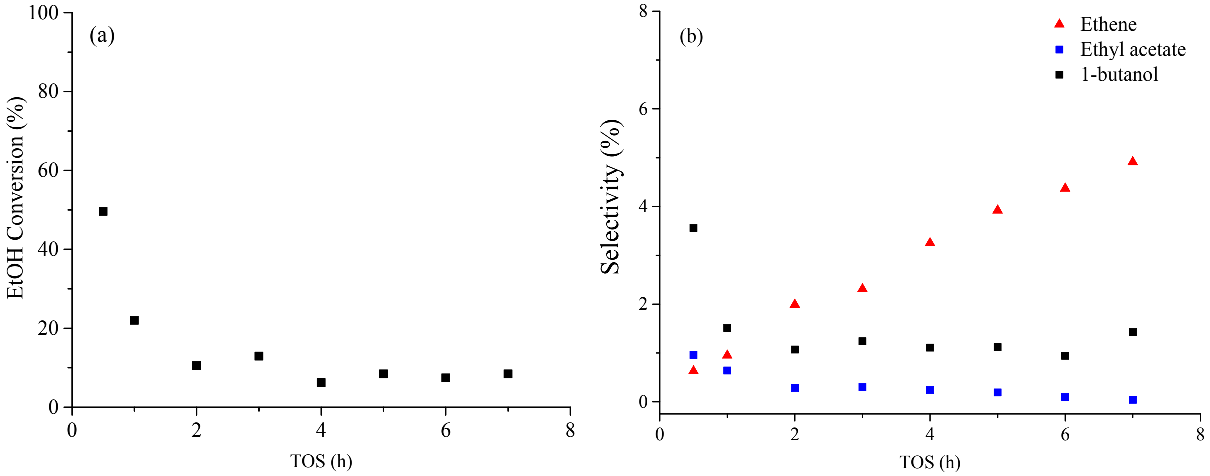

Figure 3.2. (a) Ethanol conversion over Cu/$MgAl_xO_y$ catalyst and (b) selectivities towards ethene, ethyl acetate, and 1-butanol. Reaction conditions: 0.2 g of 5 wt% Cu/$MgAl_xO_y$; T: 573 K; P: 1 atm; EtOH flow rate: 14.3 µl min^{-1}; He flow rate: 70 cm^3 min^{-1}.

3.3.1.2. Overcoated catalysts for hydrothermal stability

The hydrodeoxygenation of biomass-derived sugars is carried out in aqueous environment at elevated temperatures over silica and alumina supported catalysts. The hydrolysis of Si-O linkages in silica supports and the loss of crystallinity in alumina supports in high-water environments lead to catalyst deactivation.[27,28] The hydrothermal stability of the catalysts is of utmost importance under such reaction conditions. The upgrading of monofunctionals present in the aqueous fraction of the effluent will require a catalyst that is hydrothermally stable. Titania and zirconia are known to be hydrothermally stable supports but they have the drawback of having low surface areas.[29] To this end, we overcoated high surface area supports such as silica and alumina with titania and zirconia using ALD. The catalyst synthesis protocol is described in Chapter 2. Nitrogen physisorption isotherms were measured at 77 K using Micromeritics ASAP 2020. The surface areas were calculated using the BET method. Pore size distributions were obtained using the BJH method of the desorption branch of the isotherm.

Hydrothermal treatment constituted of aging catalyst samples in water at 473 K with 28 bar of He for 12 h in a Parr reactor. The aged samples were washed with water, filtered and dried in an oven at 393 K overnight. The nitrogen physisorption isotherms were again measured to probe any changes in the BET area as well as the pore size distribution. We prepared a zirconia-overcoated sample with silica substrate ($10ZrO_x/SiO_2$) using 10 ALD cycles of zirconium precursor (tetrakis(dimethylamido)zirconium) and water. The BET surface area of the fresh $10ZrO_x/SiO_2$ was 314 m^2 g^{-1} but it decreased to 125 m^2 g^{-1} after aging. The average pore diameter increased from 10.90 to 26.38 nm, thereby indicating that this material was not hydrothermally stable. Titania was deposited using 5 and 15 cycles of alternate $TiCl_4$ and H_2O pulses in an ALD fluidized bed reactor to synthesize $5TiO_2/\gamma\text{-}Al_2O_3$ and $15TiO_2/\gamma\text{-}Al_2O_3$, respectively. We performed hydrothermal aging experiments for these samples and control runs for $\gamma\text{-}Al_2O_3$ and TiO_2. The physisorption isotherms and pore size distributions are shown in Figure 3.3.

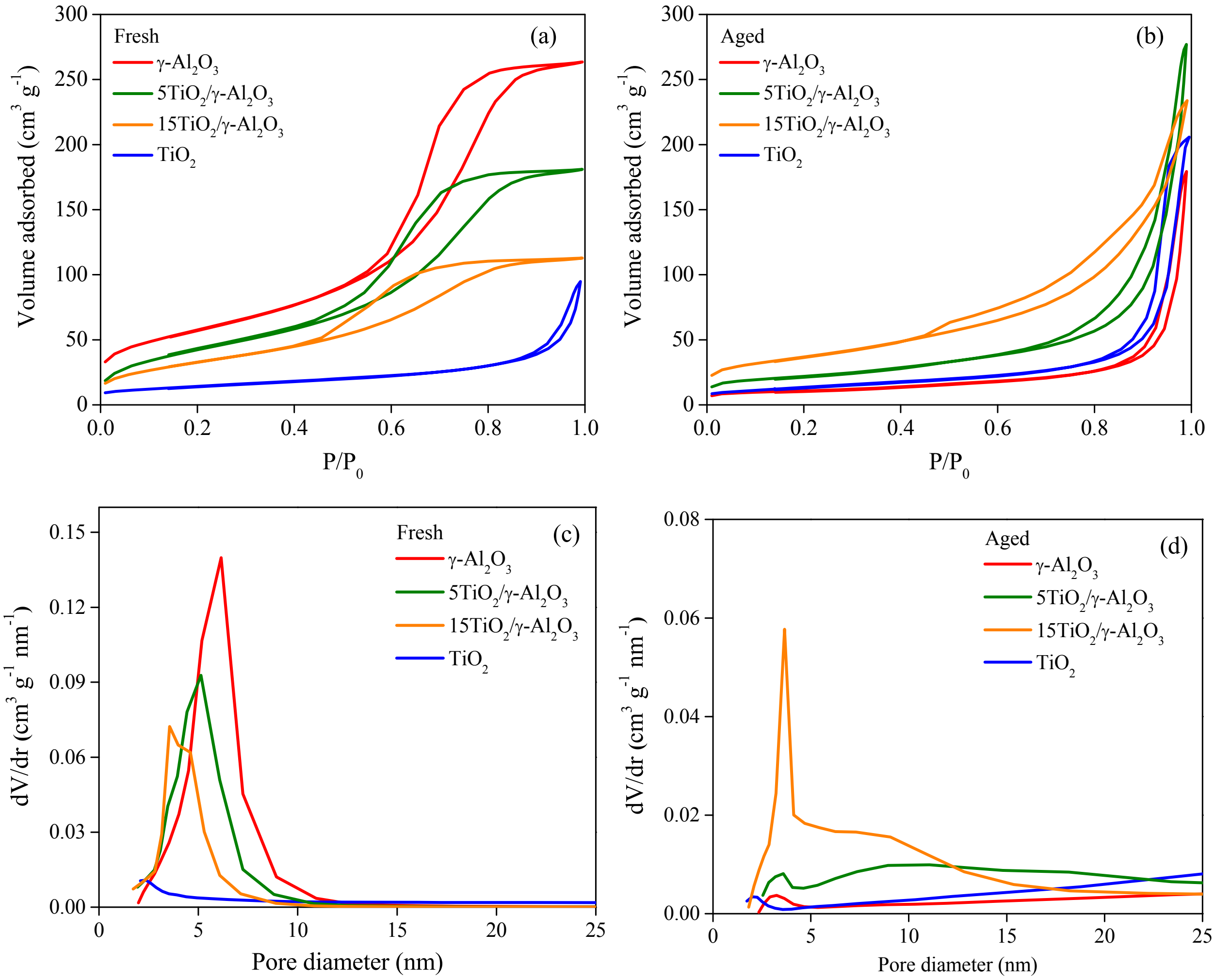

Figure 3.3. Nitrogen adsorption-desorption isotherms and pore size distribution measured for fresh ((a) and (c), respectively) and hydrothermally aged ((b) and (d), respectively) samples.

We observed that the γ-Al_2O_3 substrate is not stable under the hydrothermal treatment whereas TiO_2 shows remarkable hydrothermal stability (Table 3.2). The surface area goes down for the 5TiO_2/γ-Al_2O_3 post aging but it still higher than the surface area of the aged γ-Al_2O_3. The 15TiO_2/γ-Al_2O_3 sample shows rather remarkable stability post this treatment. The mean pore diameter keeps decreasing as we increase the number of ALD cycles which is indicative of the ALD overcoating onto the pore walls. The mean pore diameter for the aged γ-Al_2O_3 and aged 5TiO_2/γ-Al_2O_3 suggests a possible collapse of the structure. The pore diameters of the as-prepared and aged 15TiO$_2$/γ-Al$_2$O$_3$, however, are only slightly varied thereby suggesting good hydrothermal stability for this sample.

Table 3.2. BET surface areas and BJH pore diameters of the fresh and hydrothermally aged samples.

Sample	**BET surface area (m^2 g^{-1})**		**BJH pore diameter (nm)**	
	Fresh	**Aged**	**Fresh**	**Aged**
γ-Al$_2$O$_3$	209	39	6.15	32.12
5TiO$_2$/γ-Al$_2$O$_3$	160	77	5.13	11.06
15TiO$_2$/γ-Al$_2$O$_3$	122	132	3.56	3.65
TiO$_2$	51	49	2.37	2.26
SiO$_2$	317	73	10.94	30.22
10ZrO$_x$/SiO$_2$	314	125	10.90	26.38

3.3.1.3. Dehydration of linear alcohols

Since majority of the monofunctional compounds are alcohols, the dehydration of alcohols was studied as the first step in the dehydration-oligomerization route for C-C coupling. We investigated the conversion of ethanol and 1-hexanol over solid acids such as H-ZSM-5 (SiO$_2$:Al$_2$O$_3$ = 23), SiO$_2$/Al$_2$O$_3$, γ-Al$_2$O$_3$ and mixed oxide such as MgAl$_x$O$_y$. The vapor-phase dehydration was carried out in a flow reactor and the analytical protocol comprised of first injecting the gaseous effluent in GC-FID and GC-TCD and thereafter injecting the liquid drained from the condenser in a GC-FID. For ethanol conversion over H-ZSM-5, the conversion decreases from 97% to 85% in 42 h time on stream. As seen in Figure 3.4(a), the rate of both ethanol consumption and ethene production decreased as the reaction progressed. With decreasing ethanol conversion, the selectivity towards ethene went down as that towards diethyl ether increased (Figure 3.4(b)).

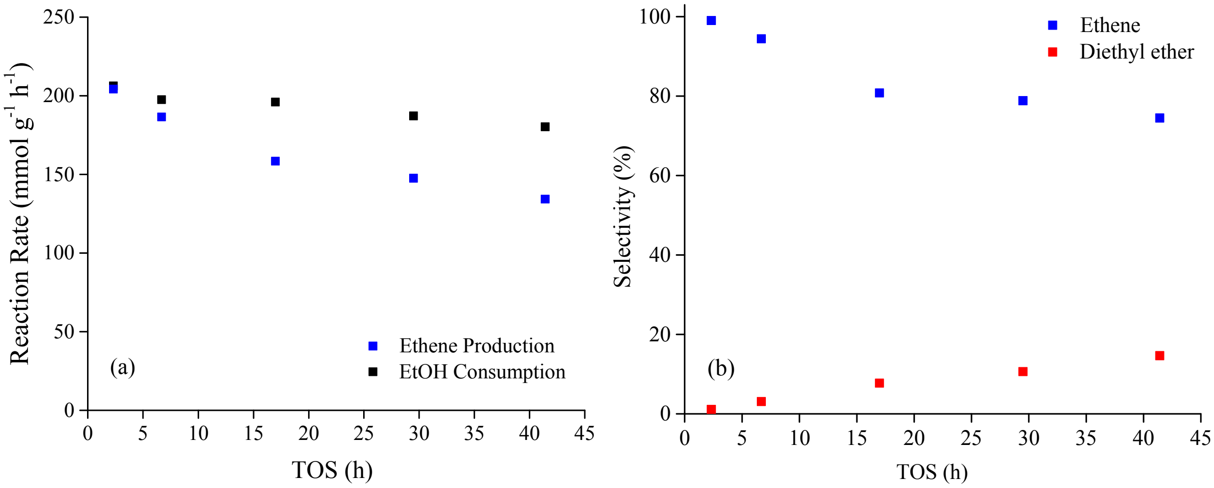

Figure 3.4. (a) Rate of EtOH consumption and ethene production (b) Selectivity towards ethene and diethyl ether. Reaction conditions: 0.2 g of H-ZSM-5; T: 548 K; P: 1 atm; EtOH flow rate: 0.04 mL min^{-1}; He flow rate: 30 cm^3 min^{-1}.

Thermogravimetric analysis was employed to study the extent of deactivation. Two step changes were observed during this analysis, one for loss of water around 373 K and the other due to burning of coke in oxygen atmosphere at 787 K. We observed a 8.5 wt% decrease in weight due to loss of coke deposited on the catalyst surface (Figure 3.5). The carbon lost due to coke formation was observed to be less than 0.1% of the carbon fed to the reactor during the entire reaction.

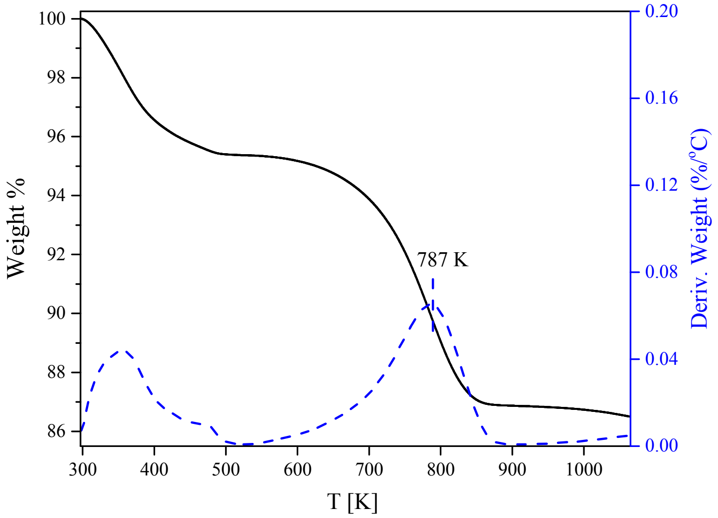

Figure 3.5. Thermogravimetric analysis of the spent H-ZSM-5 catalyst after EtOH dehydration.

Dehydration of a higher alcohol, 1-hexanol, was studied in the same reactor setup. Under similar operating conditions, 1-hexanol conversion decreased from 100% to 65% in 41 h. The deactivation rate for H-ZSM-5 was higher for 1-hexanol than for ethanol. Primarily hexene isomers were formed via dehydration whereas some C_3-C_5 hydrocarbons were formed due to cracking side reactions. A significant amount of isomerization (both branching and double-bond shift) was observed as can be seen in Figure 3.6(a) which compares the rate of formation of hexene isomers (excluding 1-hexene) to that of the rate of 1-hexene formation. In addition to 2-hexene and 3-hexene, other hexene isomers such as 2-methyl-2-pentene, 3-methyl-2-pentene, 2-methyl-1-pentene, and 2,3-dimethyl-2-butene were formed.

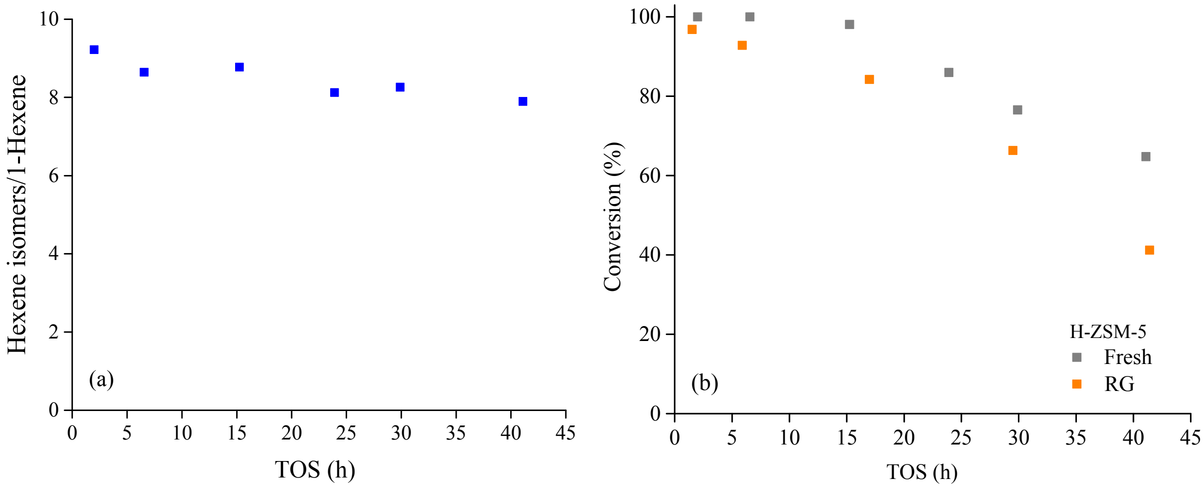

Figure 3.6. (a) Ratio of rate of production of hexene isomers (excluding 1-hexene) to the rate of formation of 1-hexene over H-ZSM-5 and (b) EtOH conversion over fresh and regenerated H-ZSM-5 catalyst. Reaction conditions: 0.2 g H-ZSM-5; T: 548 K; P: 1 atm; 1-HexOH flow rate: 0.04 mL min^{-1}; He flow rate: 30 cm^3 min^{-1}; RG: Regeneration in air at 773 K for 2 h.

Regenerability of H-ZSM-5 for 1-hexanol dehydration was investigated (Figure 3.6(b)). After the reaction on fresh catalyst, the reactor was cooled to room temperature and then the same bed was calcined in flowing air at 773 K for 2 h. The online GC-TCD was used to track the production of CO_2. Dehydration of 1-hexanol was carried out over this regenerated catalyst, and it was observed that the conversion decreases with time on stream for both the fresh and regenerated catalysts but the regenerated catalyst appears to deactivate faster than the fresh catalyst. Water is known to cause dealumination of the zeolite framework thereby reducing the number of Brønsted acid sites.[30-32] Dehydration is directly related to the concentration of Brønsted acid sites. The decrease in dehydration activity over H-ZSM-5 and the irreversible deactivation can thus be explained. A solution to this issue would be to use a pre-steamed H-ZSM-5.

The dehydration of 1-hexanol over H-ZSM-5 led to formation of isomerized hexenes with low selectivity to α-olefin. This was attributed to high acidity of the zeolite. Since our focus is to make high cetane molecules, we need to use catalysts which are less acidic. In this regard, we studied 1-hexanol dehydration on lesser acidic catalysts like SiO_2/Al_2O_3, and γ-Al_2O_3. A purely Lewis solid acid, γ-Al_2O_3 was pretreated in He at 773 K for 2 h before each reaction. The conversion of 1-HexOH decreased initially but remained almost the same as the reaction progressed (Figure 3.7(a)). Qualitative analysis performed using GC-MS showed the formation of 1-hexene, 2-hexene, and dihexyl ether (DHE). No skeletal isomerization was observed over this catalyst. Among the hexenes, 1-hexene was the major product thereby yielding good α-olefin selectivity. This, however, was accompanied by formation of DHE with nearly the same carbon selectivity (Figure 3.7(b))

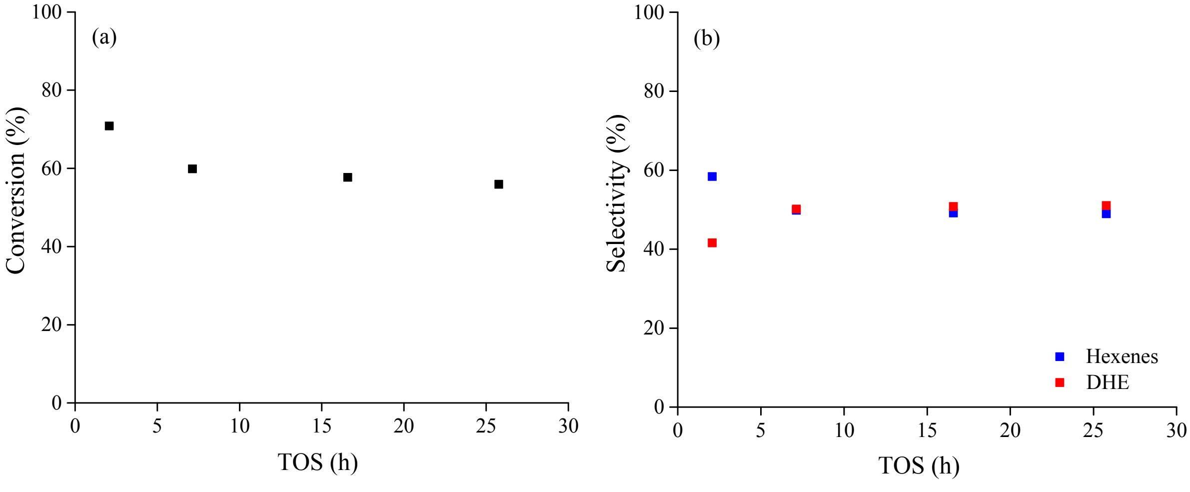

Figure 3.7. (a) 1-HexOH conversion and (b) product selectivity over γ-Al_2O_3. Reaction conditions: 0.2 g γ-Al_2O_3; T: 548 K; P: 1 atm; 1-HexOH flow rate: 0.04 mL min^{-1}; He flow rate 30 cm^3 min^{-1}.

With the same operating conditions over SiO_2/Al_2O_3, GC-MS showed formation of 1-hexene, 2-hexene, 3-hexene, and DHE. Skeletal isomerization was negligible over SiO_2/Al_2O_3. Conversion of 1-HexOH decreased from 64.5% to 40.6% with 26 h time on stream (Figure 3.8(a)). From the selectivity plot, hexenes are the major product with minor carbon selectivity towards the ether. Unlike in the case of γ-Al_2O_3, double bond isomerization was significant over SiO_2/Al_2O_3.

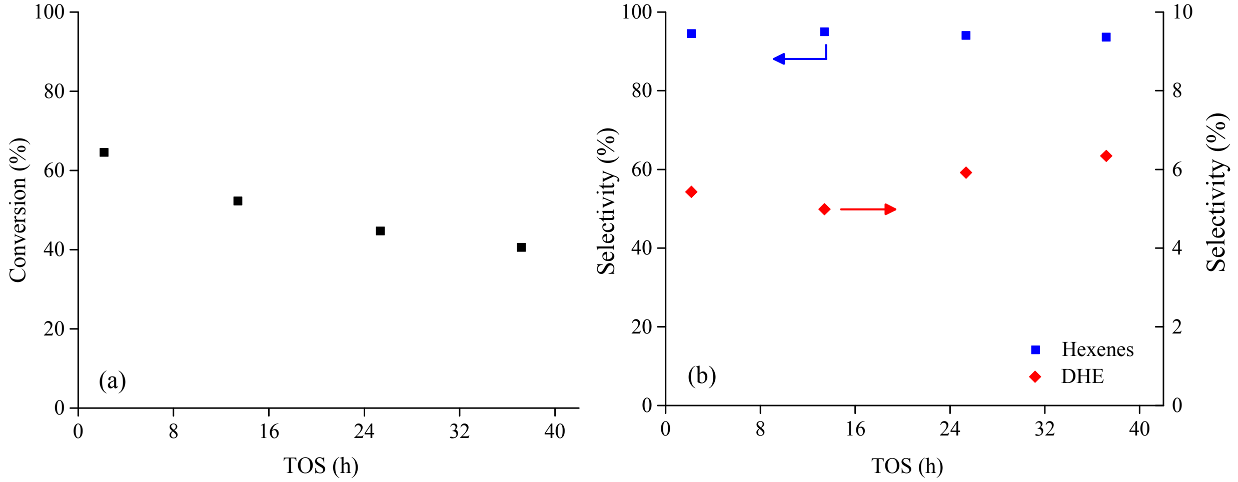

Figure 3.8. (a) 1-HexOH conversion and (b) product selectivity over SiO_2/Al_2O_3. Reaction conditions: 0.2 g SiO_2/Al_2O_3; T: 548 K; P: 1 atm; 1-HexOH flow rate: 0.04 mL min^{-1}; He flow rate: 30 cm^3 min^{-1}.

To further understand the product formation over γ-Al_2O_3 and SiO_2/Al_2O_3, we performed the weight hourly space velocity (WHSV) studies. By increasing the space velocity (i.e. decreasing the space time), we can determine the primary and secondary products and thereby develop a reaction network. Similar work has been reported in the literature for 1-butanol dehydration.[22,33] Dehydration of 1-HexOH was carried out at different WHSVs over SiO_2/Al_2O_3 with the catalyst regeneration step in between. After performing a certain WHSV run, the catalyst bed was regenerated via calcination at 773 K for 2 h. The reactor was cooled to room temperature and pretreated in helium before heating it back to the reaction temperature. Three data points were obtained within 10 h of the start of the reaction. Hexenes and DHE production rates were plotted for these data points against time on stream to obtain the initial rates. The plot of initial rates versus inverse of space velocity over SiO_2/Al_2O_3 can be seen in Figure 3.9. The y-intercept for both these curves is positive and thus, the hexenes and DHE are primary products.

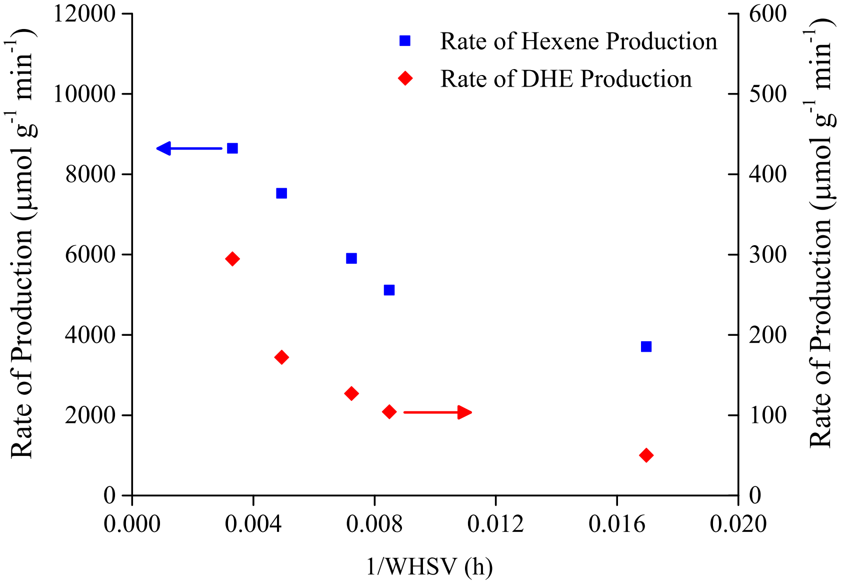

Figure 3.9. Initial rate of formation of hexenes and DHE versus the inverse of space velocity over SiO_2/Al_2O_3. The catalyst was regenerated by calcination in between different WHSVs.

The hexenes include 1-hexene, 2-hexene, and 3-hexene. When they are plotted separately, at any given WHSV, the rate of 3-hexene production is the highest. Since the first olefin to be formed from 1-HexOH dehydration is 1-hexene, Figure 3.10 shows that rapid double bond isomerization takes place over this catalyst. The gas phase thermodynamic calculations performed using values from Yaws' handbook show that if we start with 100 moles of 1-hexene, we will have 10 moles of 1-hexene, 24.4 moles of trans-2-hexene, and 65.6 moles of trans-3-hexene at equilibrium at 548 K.[34]

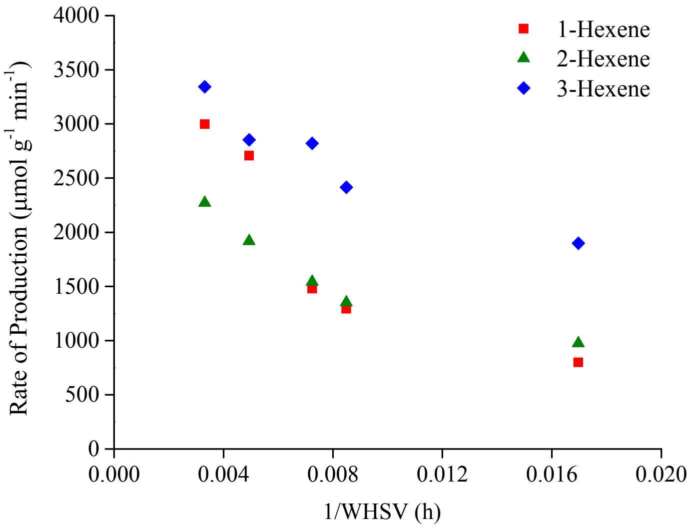

Figure 3.10. Initial rate of formation of 1-hexene, 2-hexene, and 3-hexene versus space time over SiO_2/Al_2O_3.

The reaction network for 1-HexOH dehydration over γ-Al_2O_3 was also determined by WHSV runs with catalyst regeneration in between. Similar to SiO_2/Al_2O_3, hexenes and DHE were found to be primary products (Figure 3.11). However, unlike SiO_2/Al_2O_3, double bond shift isomerization was not significant and the rate of production of 1-hexene was the highest.

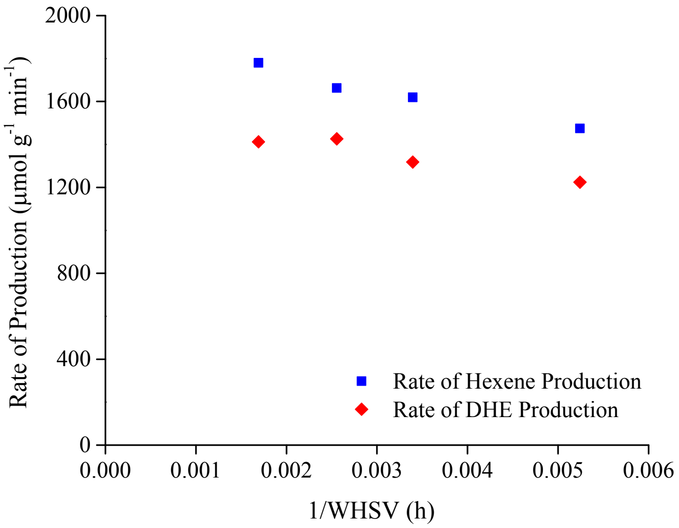

Figure 3.11. Initial rate of formation of hexenes and DHE versus the inverse of space velocity over γ-Al_2O_3. The catalyst was regenerated by calcination in between different WHSV runs.

We studied 1-hexanol dehydration over a mixed oxide, $MgAl_xO_y$. Qualitative analysis performed using GC-MS showed the formation of 1-hexene, dihexyl ether, hexanal, and 2-butyl-

1-octanol. No double bond shifting or skeletal isomerization was observed over this catalyst. The rate of dehydration to 1-hexene per mass of catalyst, however, was low compared to that on γ-Al_2O_3 and SiO_2/Al_2O_3. We observed the formation of a C-C coupled product, the C_{12} alcohol, over the mixed oxide. A fresh batch of catalyst was packed for each of the various space velocity experiments. Three data points were obtained within 10 h of the start of the reaction. The plot of initial rates of production of the products versus inverse of space velocity over $MgAl_xO_y$ can be seen in Figure 3.12. The y-intercepts for DHE, hexene and hexanal are positive, thus these species are the primary products. The curve for C_{12} alcohol appears to go through origin for the limit of zero space time implying that it is a secondary product. This supports the identification of hexanal as a primary product and 2-butyl-1-octanol as a secondary product since the C_{12} alcohol is likely a product of aldol condensation of hexanal over the mixed oxide.

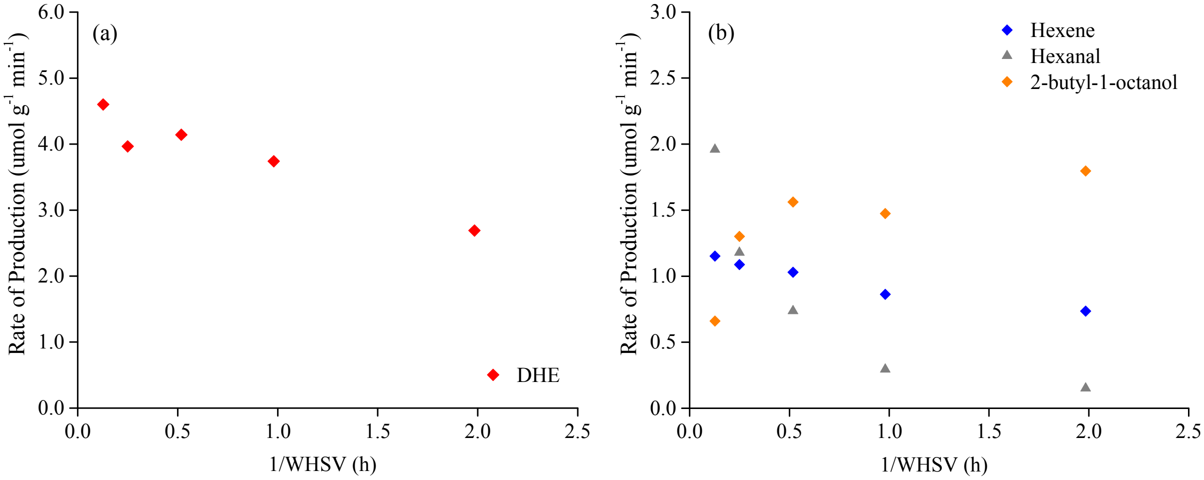

Figure 3.12. Initial rate of formation of (a) DHE, (b) hexene, hexanal and 2-butyl-1-octanol over $MgAl_xO_y$. A fresh catalyst bed was packed for different WHSVs. Operating conditions: 0.5- 4 g $MgAl_xO_y$; T: 548 K; P: 1 atm; 1-HexOH: He molar ratio= 0.26.

Amongst SiO_2/Al_2O_3, γ-Al_2O_3, and $MgAl_xO_y$, SiO_2/Al_2O_3 showed the highest carbon selectivity towards hexenes (Figure 3.13). The rate of production of hexenes was also the highest over SiO_2/Al_2O_3. The α-olefin selectivity was the highest over γ-Al_2O_3 but the carbon selectivity towards undesired dehydration product, dihexyl ether, was 60% as compared to 10% over SiO_2/Al_2O_3. The C-C coupled product, 2-butyl-1-octanol was observed over $MgAl_xO_y$ but the specific rate was very low (1.1 μmol g^{-1} min^{-1}). Thus, SiO_2/Al_2O_3 was chosen to study the conversion of simulated feed representing the actual effluent from sorbitol aqueous phase hydrodeoxygenation reactor.

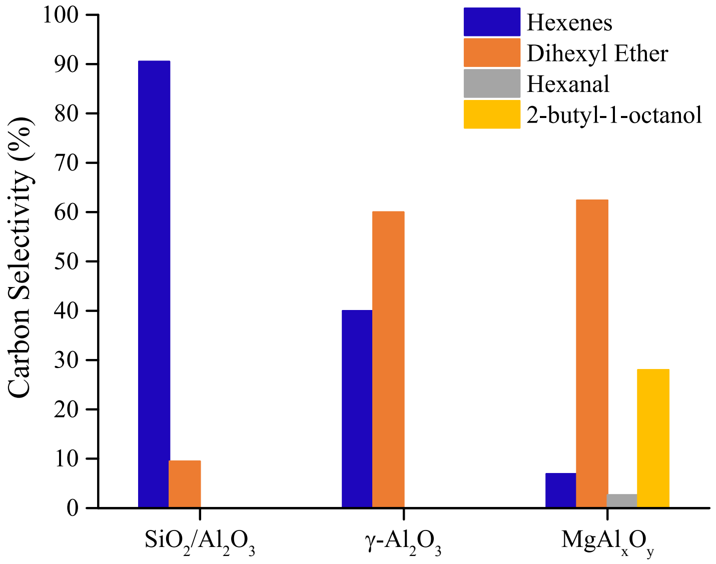

Figure 3.13. Comparison of product selectivities over SiO_2/Al_2O_3, γ-Al_2O_3, and $MgAl_xO_y$ at 548 K and 1 atm. Selectivities are compared at ~22% 1-HexOH conversion.

3.3.1.4. Conversion of simulated feed

For studying the conversion of a mixed alcohol system, a simulated feed was prepared by mixing monofunctional intermediates at weight ratios similar to the effluent of 20 wt% sorbitol APHDO (Table 3.3). Reactions were carried out at the same WHSV for a range of temperatures between 548 K and 623 K with increments of 25 K. This study was aimed at investigating the extent of cracking with increasing temperatures. At 548 K, the secondary alcohols in the feed showed nearly 100% conversion while the primary alcohols and the heterocycles were largely unconverted. Butenes, pentenes, and hexenes were observed whereas self or cross ethers were not seen. Among the alkenes, respective double bond isomers were detected though their skeletal counterparts were not observed.

Table 3.3. Simulated feed representing the monofunctionals seen in the sorbitol APHDO effluent.

Feed Components	wt%
3-hexanol	26.7
2-hexanol	18.6
2-pentanol	17.2
1-hexanol	14.1
1-pentanol	9.2
2-methyltetrahydrofuran	7.7
1-butanol	6.7

The alkene yield increases with an increase in temperature (Figure 3.14) but is accompanied by an increase in the formation of C_2 and C_3 alkenes. The extent of cracking was measured by tracking the percent of carbon converted to C_2 and C_3 alkenes (undesired alkenes) to the carbon present in all the alkenes formed. At 623 K, this value was 0.1% which implies that cracking is not significant under these operating conditions and that the overarching goal of high alkene yield can be achieved by increasing the reaction temperature.

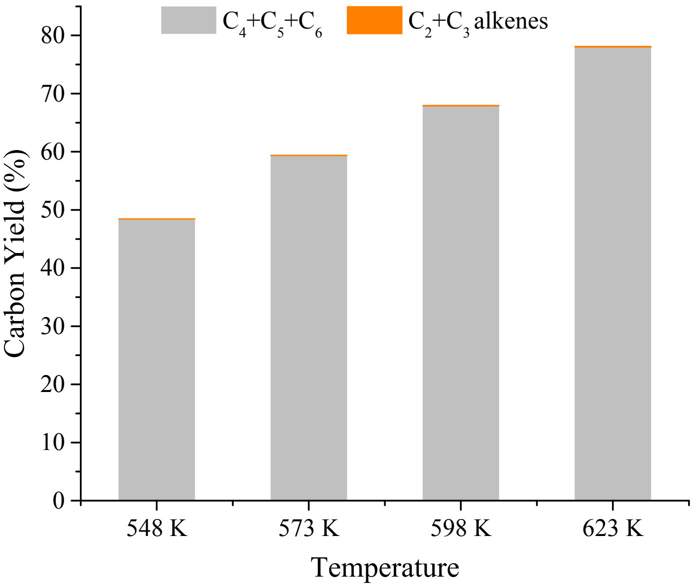

Figure 3.14. Yield of C_4+C_5+C_6 alkenes (desired) and C_2+C_3 alkenes (undesired) at various reaction temperatures. Reaction conditions: 0.1 g SiO_2/Al_2O_3; P: 1 atm; WHSV: 40 h^{-1}.

3.3.2. Conversion of actual sorbitol APHDO effluent

Conversion of monofunctionals feed obtained from aqueous phase hydrodeoxygenation of sorbitol at 523 K over Co/TiO_2 was studied. The organic phase of the sorbitol APHDO effluent was extracted in cyclohexane to obtain a 6 wt% monofunctionals feed prior to the reaction. Before carrying out the reaction with this feed, we performed a reaction with a 6 wt% 1-hexanol in cyclohexane to obtain the optimal reaction conditions. Assuming dehydration to be a near-first order reaction, the conversion is independent of concentration. We obtained 100% conversion over SiO_2/Al_2O_3 with the 6 wt% 1-HexOH in cyclohexane feed over ~30 h time on stream and 90% carbon yield to hexene isomers as seen in Figure 3.15.

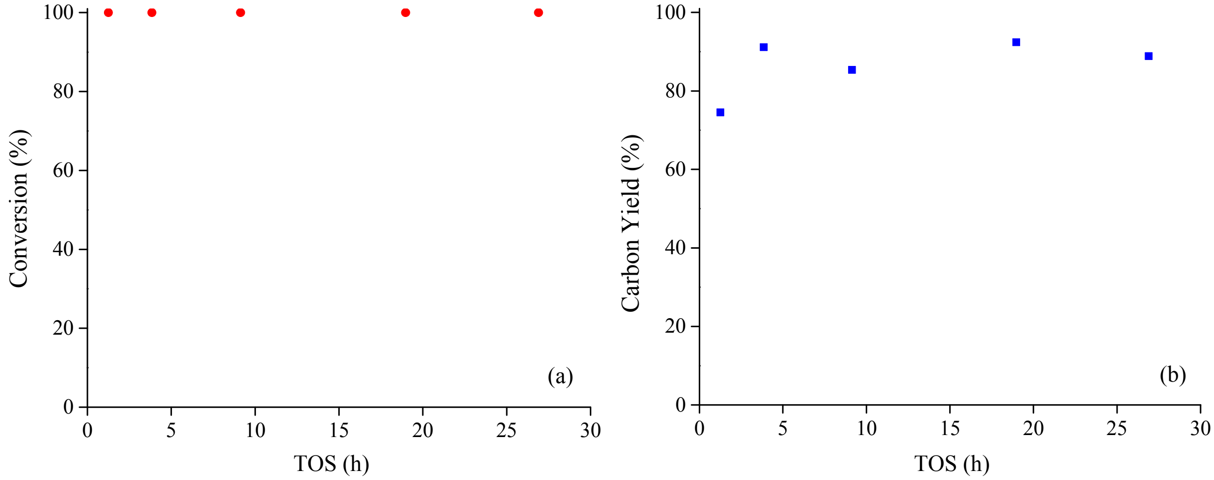

Figure 3.15. (a) 1-HexOH conversion and (b) yield towards hexenes over SiO_2/Al_2O_3. Reaction conditions: 0.1 g SiO_2/Al_2O_3; T: 623 K; P: 1 atm; WHSV: 19 h^{-1}; 30 cm^3 min^{-1} He.

At these operating conditions, both double bond and skeletal isomerization were observed. The double bond shifted isomers 1, 2, and 3-hexenes and skeletal isomerized hexenes- 3-methyl-1-pentene, 4-methyl-2-pentene, 3-methyl-2-pentene, etc. were seen. Cracking to smaller C_2-C_5 alkenes was observed but was negligible as compared to the total alkenes formed.

Table 3.4. First 10 major compounds in the organic phase produced from the effluent of sorbitol APHDO.

Feed Components	wt.%
1-pentanol	0.75
3-hexanol	0.68
1-hexanol	0.65
2-hexanol	0.51
2,5-dimethyltetrahydrofuran	0.47
2-methyltetrahydropyran	0.42
1-butanol	0.35
Tetrahydropyran	0.32
2-pentanol	0.26
2-methyltetrahydrofuran	0.21

We used the same operating conditions for conversion of 6 wt% monofunctionals feed over SiO_2/Al_2O_3. The main functionalities in the feed are alcohols, heterocyclics, ketones, and aldehydes. The first 10 major compounds in the monofunctionals feed are listed in Table 3.4. A total of 27 compounds were identified to be present in the monofunctional feed.

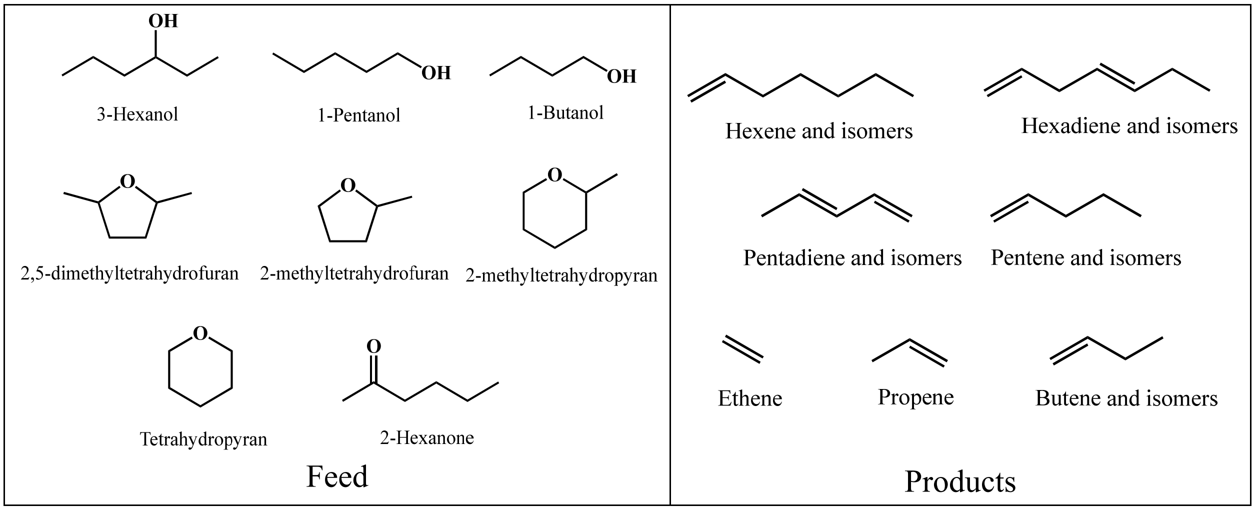

Figure 3.16. Representative feed components (left) and the products (right) for conversion of actual monofunctionals feed over SiO_2/Al_2O_3.

The representative feed components and products are as shown in Figure 3.16. The conversion of 1-pentanol (highest weight fraction in the feed) is as seen in Figure 3.17(a). In addition to 1-pentanol, all other alcohols show full conversion throughout the course of reaction. We obtain ~75% yield based on the total carbon fed to alkenes including monoalkenes and dienes (see Figure 3.17(b)). This yield is similar to that obtained for a simulated feed containing alcohols and heterocyclic compound studied previously. This suggests that all the different functional molecules are getting converted independently without interfering with their individual respective chemistries.

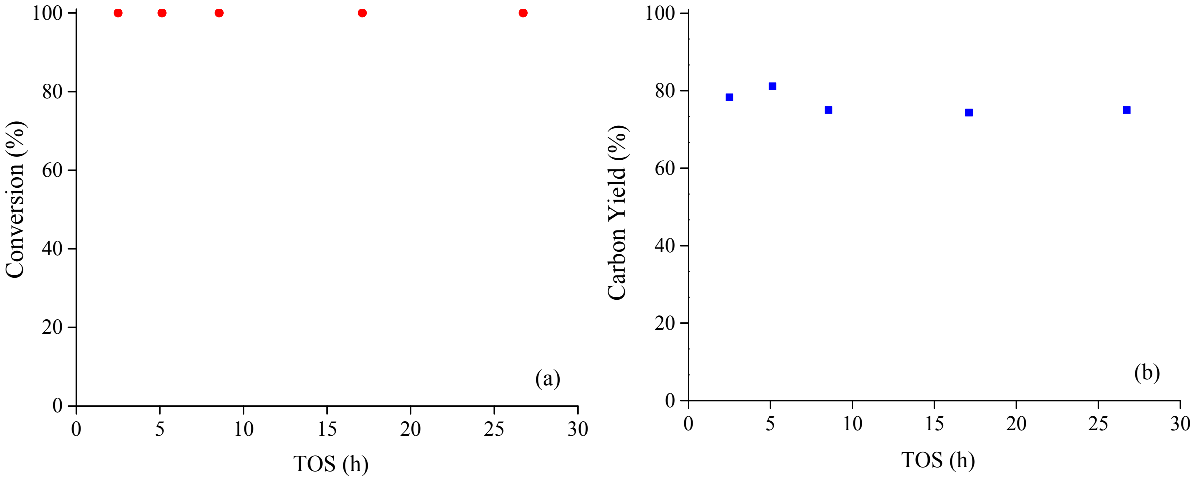

Figure 3.17. (a) 1-pentanol conversion and (b) total yield towards alkenes over SiO_2/Al_2O_3. Reaction conditions: 0.1 g SiO_2/Al_2O_3; T: 623 K; P: 1 atm; WHSV: 19 h^{-1}; 30 cm^3 min^{-1} He.

In addition to the monoalkenes, we observed formation of dienes during the real feed conversion. We hypothesize that the dienes originate from ring opening of heterocyclic species (see Chapter 4 for more details). The ketones present in the monofunctionals stream were 2-butanone, 2-pentanone, 3-pentanone, and 2-hexanone. As seen in Figure 3.18(a), the flow rate of 2-hexanone coming out of the reactor is higher than that going into the reactor. 3-hexanone was not present in the inlet stream but we observed 3-hexanone in the effluent stream (Figure 3.18(b)). This indicated that the ketones are being formed via conversion of another functional group present in the feed. We performed a reaction with 5 wt% 2-hexanone in cyclohexane over SiO_2/Al_2O_3 at 723 K and atmospheric pressure to probe if isomerization takes place to form 3-hexanone. However, we found that the carbonyl position remains unchanged indicating that 3-hexanone is being formed via a different route. We propose that the heterocyclic molecules present in the feed are getting converted to either aldehyde or ketone depending on the methyl branching on the cyclic ether as well as the position of ring opening.

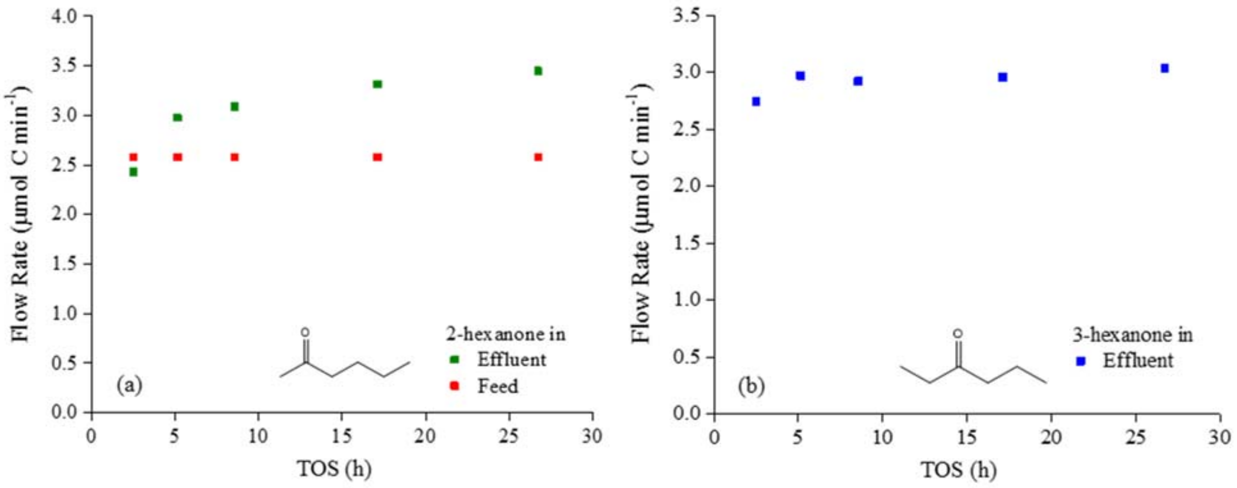

Figure 3.18. (a) Flow rate of 2-hexanone in and out of the reactor and (b) flow rate of 3-hexanone in the product stream. 3-hexanone was not present in the feed stream. Reaction conditions: 0.1 g SiO_2/Al_2O_3; T: 623 K; P: 1 atm; WHSV: 19 h^{-1}; 30 cm^3 min^{-1} He.

For example, 2-methyltetrahydropyran present in the monofunctionals can ring open to form 2-hexanone which can explain the increase in the amount of 2-hexanone coming out of the reactor. To verify this hypothesis, we added the carbon moles present in the heterocyclics, aldehydes/ketones and dienes coming out of the reactor and compared the total moles to those in the aldehydes/ketones and heterocyclics fed into the reactor (Equation(3.1)).

$$\frac{(\text{C moles (Heterocyclics + Ketones + Dienes)}_{out}}{(\text{C moles (Heterocyclics + Ketones)}_{in}} = 1 \tag{3.1}$$

If the ratio is close to 1, our hypothesis that the heterocyclics are getting converted to aldehydes/ketones is valid. As seen in Figure 3.19, this ratio is ~0.9 throughout the reaction indicating that the heterocyclics are indeed getting converted to the carbonyl compounds and dienes. 2-hexanone can be formed via ring opening of 2-methyltetrahydropyran whereas 2-ethyltetrahydrofuran ring opening can lead to the formation of 3-hexanone. 2-ethyltetrahydrofuran can be formed via the dehydration of 1,4-hexanediol, a possible monofunctional intermediate from sorbitol APHDO.

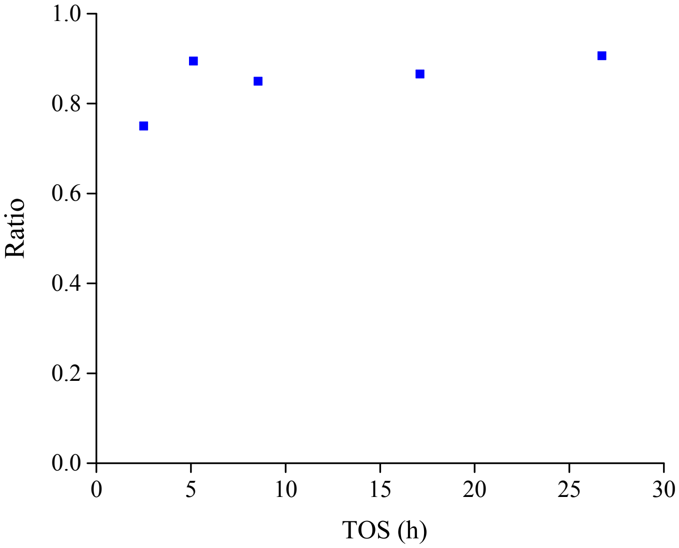

Figure 3.19. The ratio of moles of carbon in the heterocyclics, ketones, and dienes coming out of the reactor to the moles of carbon in the heterocyclics and ketones fed into the reactor during the conversion of actual sorbitol APHDO effluent to dienes.

The heterocyclics present in this monofunctional feed have 1 double bond equivalence due to their ring structure. Upon ring opening, they convert to the aldehyde form which subsequently isomerizes to the enol form. Over the acid catalyst used for this conversion, the enol undergoes dehydration forming a diene as the final product. The conversion of various heterocyclics during real feed conversion is as shown in Figure 3.20. The methyl-substituted cyclic ethers show >90% conversion whereas 2-methyltetrahydropyran conversion goes down as the reaction progresses.

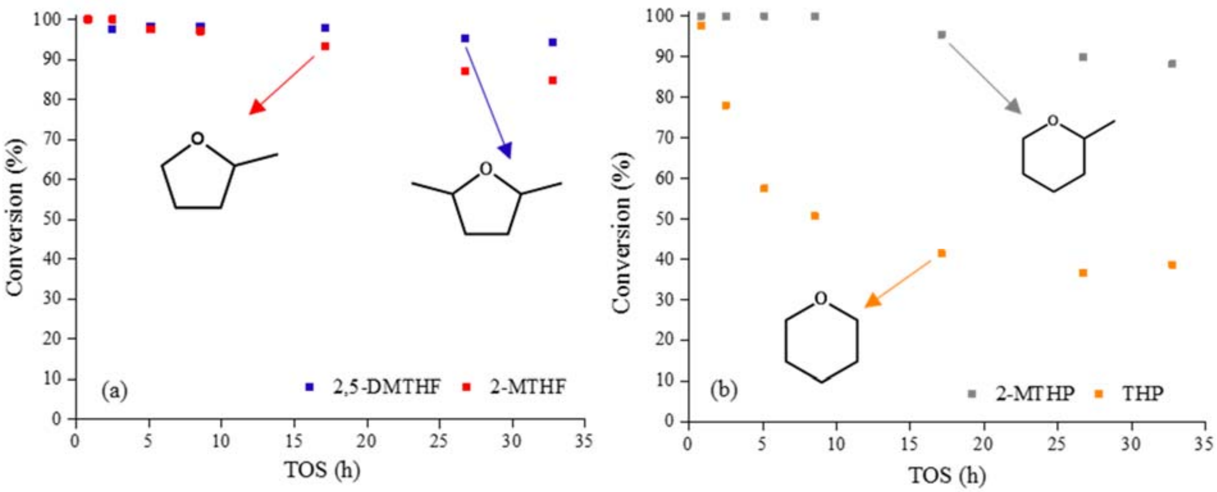

Figure 3.20. (a) Conversion of 5-membered ring heterocyclics, and (b) 6-membered ring heterocyclics present in the actual sorbitol effluent over SiO_2/Al_2O_3.

To investigate the ring opening mechanism of 2-MTHF, we performed reactions with a 10 wt% 2-MTHF in 1-HexOH feed. The conversion of 1-HexOH was ~100% for 80 h time on stream whereas that of 2-MTHF decreased from 100% to 94.8% (Figure 3.21). We observed the formation of products resulting from the dehydration and cracking of 1-HexOH as well as 2-MTHF.

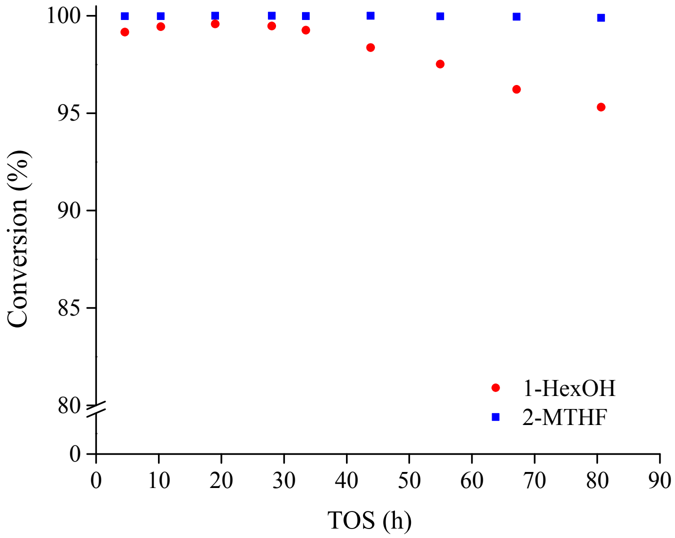

Figure 3.21. 2-MTHF and 1-HexOH conversion with time on stream over SiO_2/Al_2O_3. Reaction conditions: 1.0 g catalyst; 10 wt% 2-MTHF in 1-HexOH feed, T: 623 K; WHSV: 1.9 h^{-1}; P: 1 atm; 30 cm^3 min^{-1} He.

Cracking side reaction to C_2-C_4 alkenes with time on stream is depicted in Figure 3.22(a). As the reaction progresses the percent carbon in the undesired alkenes stays nearly constant at 2.5%. The extent of cracking is thus not very significant, and we obtain a high yield to the desired alkenes which can be subsequently oligomerized. The carbon yield towards pentadiene and pentenes combined based on 2-MTHF was ~60% i.e. 40% of the 2-MTHF carbon was unaccounted for (Figure 3.22(b)). It was, thus, difficult to decouple the conversion of 2-MTHF from that of 1-HexOH. Subsequently, we decided to use an inert solvent, dodecane, which did not show any conversion over this catalyst under the same operating conditions. The ring opening reactions of 2-MTHF and other heterocyclics present in the monofunctionals will be discussed in detail in the next chapter. The conversion of 2-MTHF over SiO_2/Al_2O_3 to a diene with minimal cracking side reactions is an important observation as it shows that we can convert the carbon present in the heterocyclics fraction of monofunctionals into molecules that can further be upgraded by oligomerization into desired distillate-range hydrocarbons.

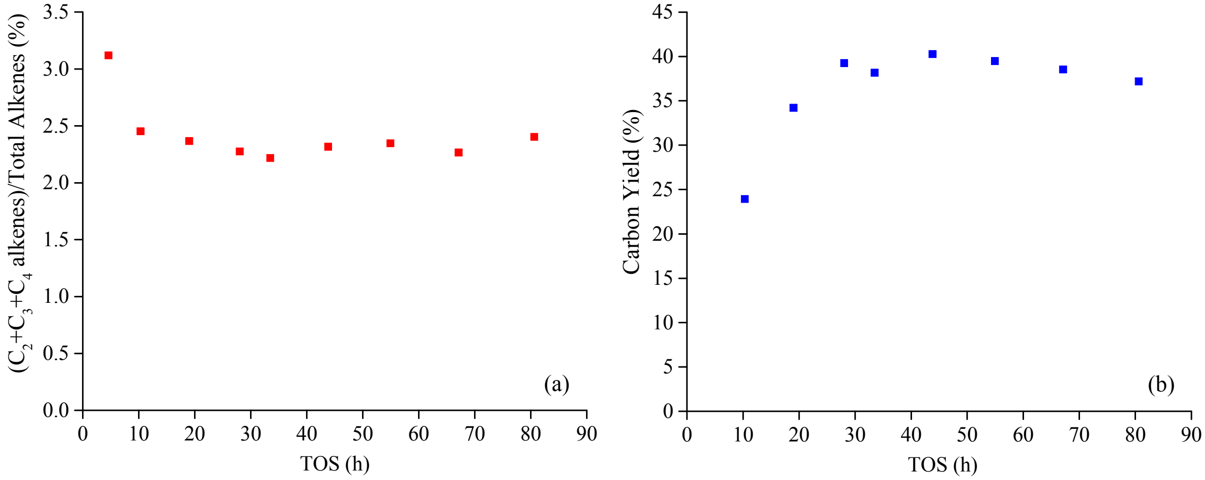

Figure 3.22. (a) Combined carbon yield towards pentadiene and pentene with time on stream and (b) percent carbon in undesired alkenes (C_2+C_3+C_4 alkenes) as compared to that in all the alkenes formed. Reaction conditions: 1.0 g catalyst; 10 wt% 2-MTHF in 1-HexOH feed, T: 623 K; P: 1 atm; WHSV: 1.9 h^{-1}; He flow rate: 30 cm^3 min^{-1}.

The Sankey diagram for the integrated process starting from LGA to C_{12} olefins is shown in Figure 3.23. The Sankey diagram summarizes the flow of carbon through each step in this cascade process starting with 100 moles of carbon in the starting material (LGA in this scenario). The height of each stream is proportional to the amount of carbon in the stream and the darkness corresponds to the carbon concentration in the molecule associated with that stream. Thus, the streams become progressively darker as we go through the deoxygenation process. Near quantitative yield of sorbitol is obtained from LGA. A 56% carbon yield of monofunctionals is obtained from sorbitol APHDO. An unidentified heavier carbon stream constitutes ~18% of the carbon that was present in sorbitol. We have achieved 75% carbon yield to olefins from the monofunctionals mixture, thereby resulting in 42.2 carbon moles in the alkenes stream. Oligomerization has been widely studied in literature over acid catalysts such as H-ZSM-5 and H-ferrierite.[19,35] Based on these studies, we propose that all the alkenes formed via dehydration can be oligomerized. Thus, starting with 100 moles of LGA, we have shown an overall carbon yield of 42.2% to distillate range molecules.

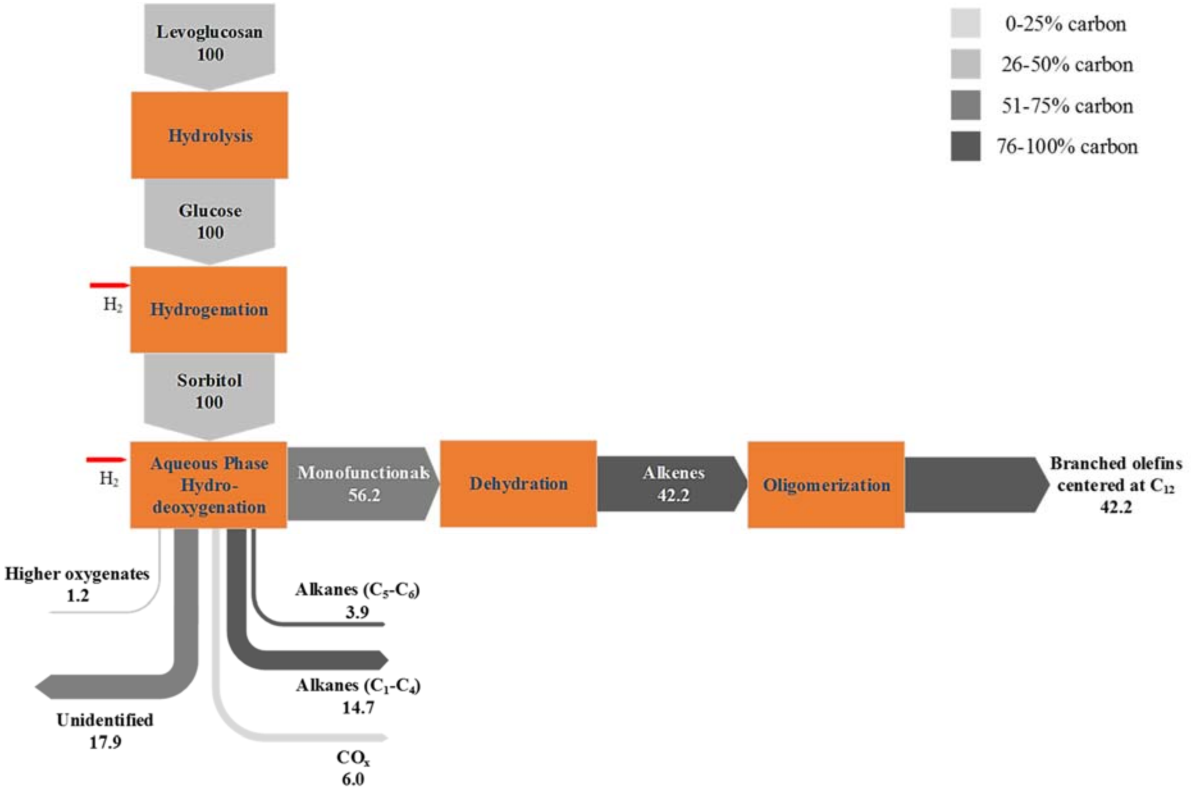

Figure 3.23. Sankey diagram representing the carbon flows for the steps involved in the overall conversion of LGA to distillate range molecules.

3.4. Conclusions

The aqueous-phase hydrodeoxygenation of sorbitol (obtained from levoglucosan) over Co/TiO_2 resulted in a monofunctional stream consisting mainly of alcohols and heterocyclics. The monofunctional intermediates can then be converted into distillate range molecules by dehydration-oligomerization route. We studied the dehydration of linear alcohols such as ethanol and 1-hexanol over crystalline H-ZSM-5, amorphous SiO_2/Al_2O_3, a Lewis acid- γ-Al_2O_3, and a mixed oxide- $MgAl_xO_y$ at 548 K and 1 atm. H-ZSM-5 suffered irreversible deactivation due to dealumination. The other catalysts deactivated with time on stream but were regenerable upon calcination. The highest rate and high selectivity towards hexenes was observed over SiO_2/Al_2O_3. Double bond shift isomerization over SiO_2/Al_2O_3 led to the formation of 1, 2, and 3-hexenes and a small amount of skeletal isomers were also seen. Nearly 97% α-olefin selectivity was obtained over γ-Al_2O_3 but the overall carbon selectivity towards undesired dihexyl ether was 60%. The C-C coupled product, 2-butyl-1-octanol was observed over $MgAl_xO_y$ but the specific rate was very low. Weight hourly space velocity studies over SiO_2/Al_2O_3 and γ-Al_2O_3 showed both hexene and dihexyl ether to be primary products.

The conversion of a simulated feed representing the product mixture from the sorbitol APHDO effluent was investigated over SiO_2/Al_2O_3 at temperatures ranging from 548 to 623 K. A carbon yield of 78% to the desired alkenes with 0.1% yield to the undesired smaller alkenes was obtained at 623 K. The actual sorbitol APHDO effluent was fed to a reactor packed with SiO_2/Al_2O_3 at 623 K to convert the monofunctionals stream to olefins. Along with monoalkenes produced from the dehydration of alcohols, we observed the formation of dienes which are proposed to originate from the heterocyclics present in the feed mixture. Nearly 75% yield to monoalkenes and dienes is obtained, based on the total carbon in the monofunctionals. This olefin yield is similar to that obtained for simulated feed indicating that the conversion of various functionalities occurs independently. Dienes are proposed to originate from ring opening of heterocyclic compounds and this chemistry is reported in Chapter 4. The C_2-C_6 olefins thus obtained can be oligomerized over acid catalysts to produce distillate range hydrocarbons.

3.5. Acknowledgements

The work in this chapter was funded by ExxonMobil and was performed by a team comprising of Dan McClelland, Nat Eagan, Peter Galebach under the guidance of Prof. G. W. Huber and Prof. J. A. Dumesic as principal investigators.

3.6. References

1. Vispute, T. P.; Zhang, H. Y.; Sanna, A.; Xiao, R.; Huber, G. W., Renewable Chemical Commodity Feedstocks from Integrated Catalytic Processing of Pyrolysis Oils. *Science* 2010, *330* (6008), 1222-1227.
2. Bai, X. L.; Johnston, P.; Sadula, S.; Brown, R. C., Role of levoglucosan physiochemistry in cellulose pyrolysis. *J. Anal. Appl. Pyrolysis* 2013, *99*, 58-65.
3. Zhang, Y. A.; Brown, T. R.; Hu, G. P.; Brown, R. C., Techno-economic analysis of monosaccharide production via fast pyrolysis of lignocellulose. *Bioresour. Technol.* 2013, *127*, 358-365.
4. Pollard, A. S.; Rover, M. R.; Brown, R. C., Characterization of bio-oil recovered as stage fractions with unique chemical and physical properties. *J. Anal. Appl. Pyrolysis* 2012, *93*, 129-138.
5. Helle, S.; Bennett, N. M.; Lau, K.; Matsui, J. H.; Duff, S. J. B., A kinetic model for production of glucose by hydrolysis of levoglucosan and cellobiosan from pyrolysis oil. *Carbohydr. Res.* 2007, *342* (16), 2365-2370.
6. Gallezot, P.; Nicolaus, N.; Fleche, G.; Fuertes, P.; Perrard, A., Glucose hydrogenation on ruthenium catalysts in a trickle-bed reactor. *J. Catal.* 1998, *180* (1), 51-55.
7. Perrard, A.; Gallezot, P.; Joly, J. P.; Durand, R.; Baljou, U.; Coq, B.; Trens, P., Highly efficient metal catalysts supported on activated carbon cloths: A catalytic application for the hydrogenation of D-glucose to D-sorbitol. *Appl. Catal. A-Gen.* 2007, *331*, 100-104.
8. Kunkes, E. L.; Simonetti, D. A.; West, R. M.; Serrano-Ruiz, J. C.; Gartner, C. A.; Dumesic, J. A., Catalytic conversion of biomass to monofunctional hydrocarbons and targeted liquid-fuel classes. *Science* 2008, *322* (5900), 417-421.
9. Blommel, P.; Dally, B.; Lyman, W.; Cortright, R., Method and systems for making distillate fuels from biomass. *US20120198760 A1* 2012.
10. Kim, Y. T.; Dumesic, J. A.; Huber, G. W., Aqueous-phase hydrodeoxygenation of sorbitol: A comparative study of Pt/Zr phosphate and Pt-ReOx/C. *J. Catal.* 2013, *304*, 72-85.
11. West, R. M.; Kunkes, E. L.; Simonetti, D. A.; Dumesic, J. A., Catalytic conversion of biomass-derived carbohydrates to fuels and chemicals by formation and upgrading of mono-functional hydrocarbon intermediates. *Catal. Today* 2009, *147* (2), 115-125.
12. West, R. M.; Liu, Z. Y.; Peter, M.; Gartner, C. A.; Dumesic, J. A., Carbon-carbon bond formation for biomass-derived furfurals and ketones by aldol condensation in a biphasic system. *J. Mol. Catal. A-Chem.* 2008, *296* (1-2), 18-27.
13. West, R. M.; Liu, Z. Y.; Peter, M.; Dumesic, J. A., Liquid Alkanes with targeted molecular weights from biomass-derived carbohydrates. *ChemSusChem* 2008, *1* (5), 417-424.

14. Huber, G. W.; Chheda, J. N.; Barrett, C. J.; Dumesic, J. A., Production of liquid alkanes by aqueous-phase processing of biomass-derived carbohydrates. *Science* 2005, *308* (5727), 1446-1450.
15. Pham, T. N.; Sooknoi, T.; Crossley, S. P.; Resasco, D. E., Ketonization of Carboxylic Acids: Mechanisms, Catalysts, and Implications for Biomass Conversion. *ACS Catal.* 2013, *3* (11), 2456-2473.
16. Gartner, C. A.; Serrano-Ruiz, J. C.; Braden, D. J.; Dumesic, J. A., Catalytic Upgrading of Bio-Oils by Ketonization. *ChemSusChem* 2009, *2* (12), 1121-1124.
17. Chia, M.; Pagan-Torres, Y. J.; Hibbitts, D.; Tan, Q. H.; Pham, H. N.; Datye, A. K.; Neurock, M.; Davis, R. J.; Dumesic, J. A., Selective Hydrogenolysis of Polyols and Cyclic Ethers over Bifunctional Surface Sites on Rhodium-Rhenium Catalysts. *J. Am. Chem. Soc.* 2011, *133* (32), 12675-12689.
18. Koso, S.; Ueda, N.; Shinmi, Y.; Okumura, K.; Kizuka, T.; Tomishige, K., Promoting effect of Mo on the hydrogenolysis of tetrahydrofurfuryl alcohol to 1,5-pentanediol over Rh/SiO2. *J. Catal.* 2009, *267* (1), 89-92.
19. Bond, J. Q.; Alonso, D. M.; Wang, D.; West, R. M.; Dumesic, J. A., Integrated Catalytic Conversion of gamma-Valerolactone to Liquid Alkenes for Transportation Fuels. *Science* 2010, *327* (5969), 1110-1114.
20. Eagan, N. E.; Chada, J. P.; Wittring, A. M.; Buchanan, J. S.; Dumesic, J. A.; Huber, G. W., Aqueous-Phase Hydrodeoxygenation of Sorbitol to Monofunctional Fuel Precursors over Co/TiO2 *In preparation*.
21. Kozlowski, J. T.; Davis, R. J., Heterogeneous Catalysts for the Guerbet Coupling of Alcohols. *ACS Catal.* 2013, *3* (7), 1588-1600.
22. Knözinger, H.; Köhne, R., Dehydration of alcohols over alumina. 1. Reaction Scheme. *J. Catal.* 1966, *5* (2), 264.
23. Knözinger, H.; Kochloef.K; Meye, W., Kinetics of bimolecular ether formation from alcohols over alumina. *J. Catal.* 1973, *28* (1), 69-75.
24. West, R. M.; Braden, D. J.; Dumesic, J. A., Dehydration of butanol to butene over solid acid catalysts in high water environments. *J. Catal.* 2009, *262* (1), 134-143.
25. Roy, S.; Mpourmpakis, G.; Hong, D. Y.; Vlachos, D. G.; Bhan, A.; Gorte, R. J., Mechanistic Study of Alcohol Dehydration on gamma-Al2O3. *ACS Catal.* 2012, *2* (9), 1846-1853.
26. Gines, M. J. L.; Iglesia, E., Bifunctional condensation reactions of alcohols on basic oxides modified by copper and potassium. *J. Catal.* 1998, *176* (1), 155-172.
27. Ravenelle, R. M.; Copeland, J. R.; Kim, W. G.; Crittenden, J. C.; Sievers, C., Structural Changes of gamma-Al2O3-Supported Catalysts in Hot Liquid Water. *ACS Catal.* 2011, *1* (5), 552-561.
28. Xiong, H. F.; Pham, H. N.; Datye, A. K., Hydrothermally stable heterogeneous catalysts for conversion of biorenewables. *Green Chem.* 2014, *16* (11), 4627-4643.
29. Duan, J. Z.; Kim, Y. T.; Lou, H.; Huber, G. W., Hydrothermally stable regenerable catalytic supports for aqueous-phase conversion of biomass. *Catal. Today* 2014, *234*, 66-74.
30. Ong, L. H.; Domok, M.; Olindo, R.; van Veen, A. C.; Lercher, J. A., Dealumination of HZSM-5 via steam-treatment. *Microporous Mesoporous Mat.* 2012, *164*, 9-20.
31. deLucas, A.; Canizares, P.; Duran, A.; Carrero, A., Dealumination of HZSM-5 zeolites: Effect of steaming on acidity and aromatization activity. *Appl. Catal. A-Gen.* 1997, *154* (1-2), 221-240.

32. Yang, H.; Coolman, R. J.; Karanjkar, P.; Wang, H.; Xu, Z.; Chen, H.; Moutziaris, T. J.; Huber, G. W., The effect of steam on the catalytic fast pyrolysis of cellulose. *Green Chem.* 2015, *17* (5), 2912-2923.
33. Berteau, P.; Ruwet, M.; Delmon, B., Reaction pathways in 1-butanol dehydration on γ-Al2O3. *Bull. Soc. Chim. Belg.* 1985, *94* (11-12), 859-868.
34. Yaws, C. L., *Yaws' Handbook of Thermodynamic and Physical Properties of Chemical Compounds*. Knovel.
35. Kim, Y. T.; Chada, J. P.; Xu, Z. R.; Pagan-Torres, Y. J.; Rosenfeld, D. C.; Winniford, W. L.; Schmidt, E.; Huber, G. W., Low-temperature oligomerization of 1-butene with H-ferrierite. *J. Catal.* 2015, *323*, 33-44.

CHAPTER 4

Ring Opening of Biomass-derived Cyclic Ethers to Dienes over Solid Acid Catalysts

4.1. Introduction

Lignocellulosic biomass has recently received considerable interest as a renewable feedstock for the production of platform molecules which can subsequently be converted to fuels and value-added chemicals.[1,2] One such molecule, 2-methyltetrahydrofuran (2-MTHF) has gained attention as a green solvent or as a gasoline additive.[3,4] 2-MTHF can be obtained from biomass-derived intermediates such as levulinic acid and furfural.[5] The pentoses in lignocellulose can be converted to furfural using acid hydrolysis.[6-8] Furfural can undergo hydrodeoxygenation to 2-MTHF in high yield in a single step over silica-supported Pd and Cu catalysts.[9] 2-MTHF is also a monofunctional intermediate produced during aqueous phase hydrodeoxygenation of sorbitol over catalysts such as Pt-Re/C and Pd-Ag/WO_x-ZrO_2.[10,11] In our on-going work of aqueous phase hydrodeoxygenation of sorbitol over Co/TiO_2, these monofunctional intermediates consist mainly of alcohols (69% of the carbon in monofunctionals) and heterocyclic species (23% of the carbon in monofunctionals).[12] These monofunctional compounds can then undergo C-C bond formation followed by hydrodeoxygenation to produce jet and diesel range blendstocks.[2,13] The monofunctionals can also be fed to an acidic catalyst to produce olefins, which can then be converted into jet and diesel fuel by oligomerization and hydrogenation reactions. In our current work, we remove the oxygen from these monofunctional compounds via dehydration using a solid acid catalyst. In addition to the monoalkenes formed by dehydration of the alcohol fraction, we also observed dienes in the effluent stream. We then performed studies over this solid acid using 2-MTHF as the model heterocyclic and observed the formation of 1,4-pentadiene and 1,3-pentadiene isomers. There is limited work reported on the dehydration of cyclic ethers to dienes. The objective of this work, therefore, is to understand the reaction network as well as the factors that affect the activity of the solid acid for this acid-catalyzed reaction.

1,3-Pentadiene, commercially known as piperylene, is a highly volatile, flammable, linear hydrocarbon. Piperylenes are by-products of the petroleum industry and are widely used as monomers in the production of adhesives, plastics, and resins. The conjugated dienes serve as substrates for conversion into highly functionalized molecules via organic reactions, e.g., Diels-Alder, hydroformylation, and carbonylation.[14,15] Currently, the main source of C_5 hydrocarbons is steam cracking of naphtha obtained from crude oil. The separation of C_5 hydrocarbons is achieved using extractive rectification and metal-organic frameworks.[16] Besides the crude oil route, majority of literature for piperylene production involves processes using thermochemical methods and homogeneous catalysis. Geller and Schniepp observed that pyrolytic decomposition of 1,5-pentanediol diacetate yielded 1,4-pentadiene with 90-96% purity at 848 K.[17] Brookhart and co-workers have reported ~40% yield to piperylenes via transfer dehydrogenation of pentane using iridium pincer complex.[18] Recently, Goldman and co-workers have reported high yields (~70%) to piperylenes for the same reaction catalyzed by pincer-ligated iridium complexes.[19] These homogeneous catalysts, however, have separations costs associated with them and have challenges for large scale applications.

An alternative and renewable route to produce pentadienes would be to employ heterogeneous catalysts for conversion of biomass-derived platform chemicals. Chia and Dumesic have studied a process for conversion of 4-hydroxy-6-methyl-2-pyrone to 6-methyl-5,6-dihydro-2-pyrone and used acid-catalyzed ring opening of the latter compound to produce 2,4-hexadienoic acid and 1,3-pentadiene.[20] The advantage of this method is that the starting material can be made from a renewable precursor, such as biomass-derived glucose using recombinant bacteria or yeast. Another process would be the conversion of C_5 cyclic ether, 2-MTHF, obtained in good yield from lignocellulose-derived pentoses. Oyama and co-workers have reported ~33% yield of pentadienes during the hydrodeoxygenation of 2-MTHF over WP/SiO_2 at 623 K.[21] Johns developed a process consisting of two-step hydrogenation of furfural to 2-MTHF using Cu and Ni catalysts and subsequently dehydrating 2-MTHF over a phosphate salt at temperatures near 600 K to obtain 1,3-pentadienes with small amount of 1,4-pentadiene.[22] Norman has reported the dehydration of 2-MTHF to piperylene in high yield over vanadium-titanium-phosphorous ternary mixed oxide and boron phosphate.[23] Over V-Ti-P oxide, 80% of 2-MTHF is converted to 1,4-pentadiene and 1,3-pentadiene with 81.4% total selectivity i.e. 65.1 % yield at 623 K and atmospheric pressure. The side products reported are 4-penten-2ol, 3-penten-2-ol, and an unknown fraction. Diene polymerization leads to formation of coke and subsequent catalyst deactivation. Dehydration of tetrahydropyran and 3-methyltetrahydrofuran to pentadiene and isoprene was carried out, but the activity was lower as compared to that for 2-MTHF.

In this work, the vapor-phase dehydration of 2-MTHF to pentadienes was investigated over various solid acids, particularly over amorphous SiO_2/Al_2O_3. We performed space velocity studies to probe the reaction network for the ring opening of 2-MTHF. The effects of temperature and partial pressure of the reactant on the activity of 2-MTHF are also discussed. In addition to 2-MTHF, ring opening of other cyclic ethers, namely, tetrahydropyran, tetrahydrofuran, and 2,5-dimethyltetrahydrofuran to their respective dienes was investigated. This conversion of cyclic ethers can serve as a potential route to make dienes from biomass.

4.2. Materials and Methods

4.2.1. Materials and Characterization

The cyclic ethers, 2-methyltetrahydrofuran (2-MTHF, Sigma-Aldrich, >99%, 250 ppm butylated hydroxytoluene as stabilizer), 2,5-dimethlytetrahydrofuran (2,5-DMTHF, Sigma-Aldrich, 96%), tetrahydrofuran (THF, Sigma-Aldrich, >99.9%, BHT as stabilizer), and tetrahydropyran (THP, Sigma-Aldrich, 99%) were used as purchased without further purification.

Amorphous SiO_2/Al_2O_3 (13.7 wt% alumina content) obtained from Grace Davison (Grade 135) was used for the ring opening of various heterocyclics to dienes. The catalyst was calcined *ex situ* at 773 K (2 K min^{-1}, 2 h) in flowing air (Airgas, 50 cm^3 min^{-1}). The BET surface area was obtained from the nitrogen adsorption isotherms carried out in a volumetric adsorption unit (Micromeritics, ASAP 2010). The catalyst was degassed at 423 K in vacuum for 6 h prior to the measurements. The surface area and mean pore diameter for the catalyst were calculated to be 450 m^2 g^{-1} and 5.4 nm, respectively. Ring opening of 2-MTHF was also investigated over various solid acids like H-ZSM-5 ($SiO_2:Al_2O_3 = 23$), H-Mordenite (H-MOR, $SiO_2:Al_2O_3 = 20$), H-Beta (H-BEA, $SiO_2:Al_2O_3 = 25$) (Zeolyst International), γ-Al_2O_3 (Strem Chemicals), Al-Sn-Beta (Al-Sn-BEA, Si/Sn=200, Si/Al= 50, Haldor Topsøe A/S, Denmark), $NbOPO_4$, and Nb_2O_5 (CBMM, Brazil).

The total and Brønsted acid site densities on the catalysts were estimated using ammonia temperature-programmed desorption (NH_3-TPD) and isopropylamine temperature-programmed desorption (IPA-TPD), respectively. The detailed experimental procedure is described in Chapter 2, Section 2.3.7.

4.2.2. Reactivity Measurements

The ring opening of various heterocyclics was studied in gas-phase in a fixed-bed down-flow reactor (Figure 4.1) at atmospheric pressure and temperatures varying from 573 to 653 K. The details of the experimental setup and analytical protocol is described in Chapter 2, Section 2.4.1. Total carbon balances are typically closed to within 10%. Both the gas and liquid products were identified using a GC-MS (Shimadzu, QP-2010).

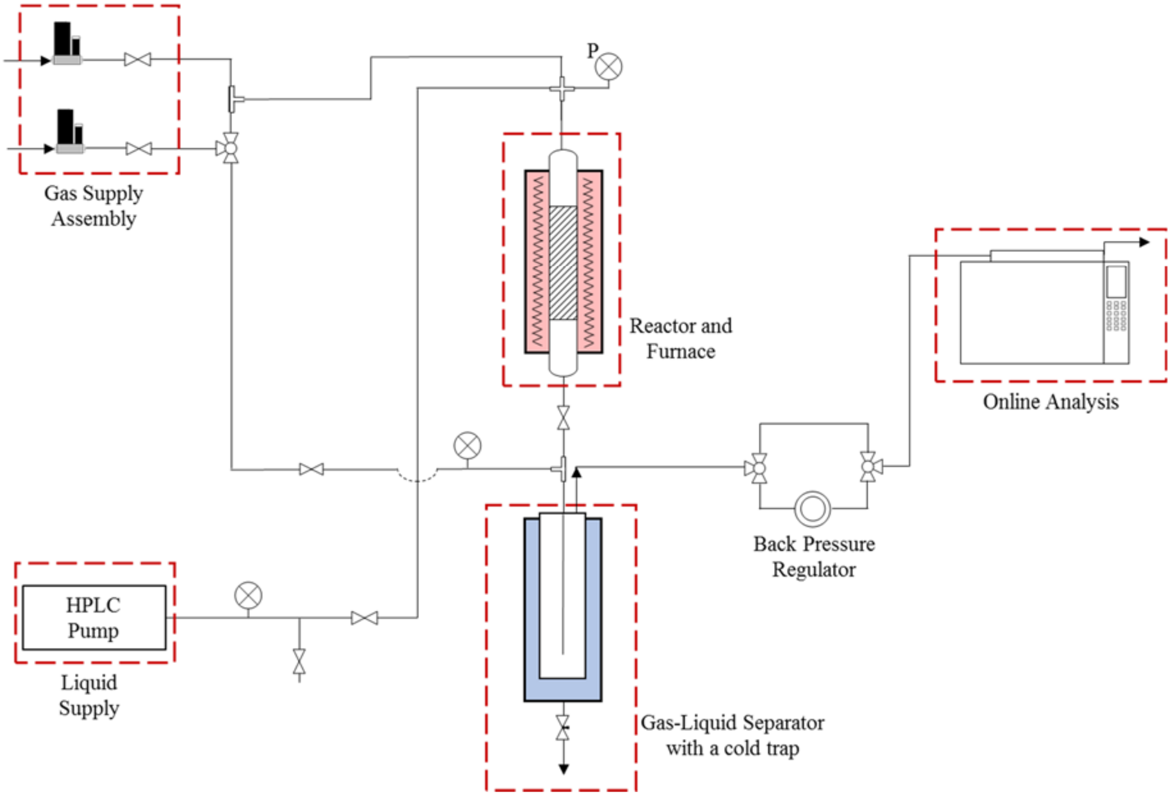

Figure 4.1. Experimental reactor setup for dehydration of cyclic ethers performed with dodecane solvent.

We carried out a control experiment to ensure that the solvent was inert. Using pure dodecane as the feed and the same reaction conditions over SiO_2/Al_2O_3, we did not observe any dodecane conversion. Similarly, to verify that the conversion of 2-MTHF to pentadiene is indeed catalytic, we performed a reaction at 623 K using a control bed in the absence of a catalyst and we did not see any 2-MTHF conversion. The kinetic studies were performed in the absence of external and internal mass transfer limitations. To assess whether intrinsic kinetic parameters were obtained in the absence of external and internal mass transfer limitations, we employed the Mears (external mass transfer, Equation(4.1)) and Weisz-Prater criteria (internal mass transfer, Equation(4.2)) using the parameters in Table 4.1. In these expressions, *Rate* is the rate of reactant consumption per unit volume of catalyst, R_p is the radius of a representative particle of the catalyst, C_b is the bulk reactant concentration, k_c is the mass transfer coefficient between the catalyst and bulk phases, *n* is the reaction order, C_s is the reactant concentration at the catalyst surface which is same as that in the bulk phase in the absence of external mass transfer limitations, and D_{eff} is the Knudsen diffusivity. The k_c and D_{eff} values were calculated using relations provided elsewhere.[24,25]

$$\frac{Rate.R_p}{C_b.k_c} < \frac{0.15}{n} \tag{4.1}$$

$$N_{W-P} = \frac{Rate.R_p^{\ 2}}{C_s.D_{eff}} < 0.3 \tag{4.2}$$

The dimensionless group on the left-hand side of the inequality for the Mears criterion was calculated to be 0.08 and that for the Weisz-Prater equation was calculated to be 0.07. Thus, based on theoretical calculations, mass transfer limitations do not exist for these experiments. The experimental verification of external mass transfer was verified by changing the catalyst mass and reactant flow proportionally to keep the space velocity constant.[26] In the absence of external mass transfer, both these reactions should produce identical results which was observed for the experiments we performed (Figure 4.2).

Table 4.1. Parameters used in the external and internal mass transfer limitation criteria.

Parameters	**Values**
N	0.24
R_p (cm)	3.2 x 10^{-3}
C_b (mol cm^{-3})	4.3 x 10^{-7}
k_c (cm s^{-1})	1.04
Rate (mol cm^3 s^{-1})	1.1 x 10^{-5}
Density (g cm^{-3})	0.45
D_{eff} (cm^2 s^{-1})	3.6 x 10^{-3}

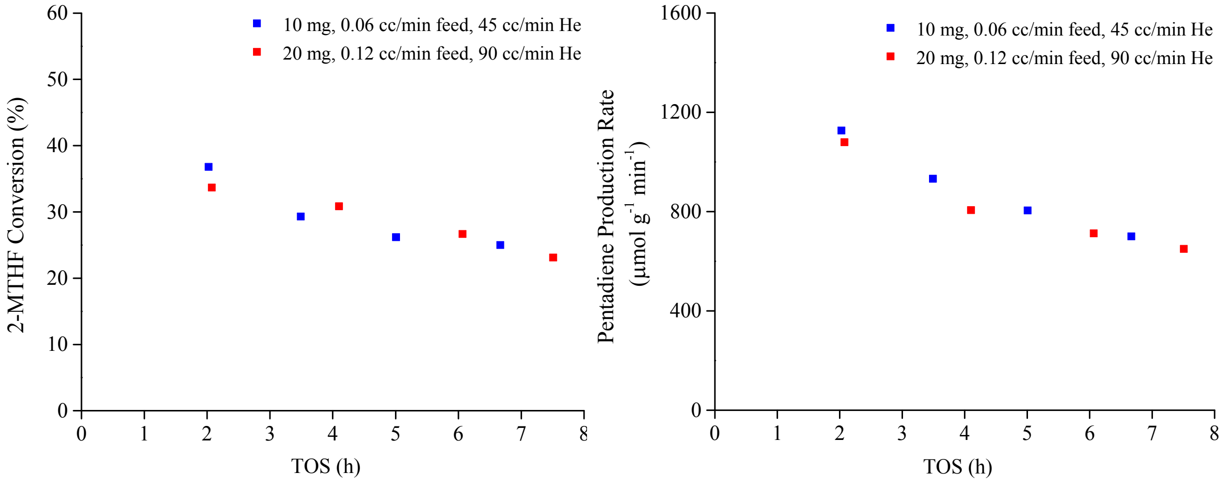

Figure 4.2. Experimental verification of the absence of external mass transfer limitations. The catalyst amount and flow rates are doubled thereby keeping a constant space velocity.

The reaction network was established using conventional contact time measurements where the product selectivities reveal the sequence of product formation. The contact times were varied by altering the catalyst amount and the reactant flow rate. Weight hourly space velocity (WHSV) was defined as the mass of the feed molecule per mass of catalyst per hour and the contact time was defined as inverse of WHSV (Equation(4.3)). The helium flow rate was chosen such that the molar ratio of 2-MTHF:He was kept constant. The rate of production of various products was plotted against the contact time to determine the primary and secondary products. The contact time experiments were carried out in the kinetic regime over SiO_2/Al_2O_3 at a constant temperature of 623 K.

$$\text{Space time (h)} = \frac{1}{\text{WHSV (h}^{-1}\text{)}} = \frac{\text{Mass of catalyst (g)}}{\text{2-MTHF flow rate (g h}^{-1}\text{)}} \tag{4.3}$$

Gaussian09 software was used for thermodynamic calculations. Geometry optimizations and subsequent frequency calculations were performed using B3LYP/6-311+G(2d,p).[27] Frequency calculations provided estimates for standard changes of enthalpy, entropy, and Gibbs free energy, which were used in estimating thermodynamic properties over the range of temperatures used in this study.

The apparent activation energy for pentadiene formation was calculated over the temperature range 573- 653 K. The reaction rate order with respect to 2-MTHF was obtained by varying its partial pressure. We observed that all solid acid catalysts undergo deactivation as the reaction progresses. Each data set was collected within 10 h of the start of the experiment and the initial rates were obtained by extrapolation to time zero. For SiO_2/Al_2O_3, we observed that initial activity could be restored completely upon calcination in air at 773 K.

For the second set of reactions without using any solvent, low flow rates of the cyclic ethers were achieved using a syringe pump (Harvard Apparatus, PHD Ultra) and helium was used as a carrier gas. The products were analysed by an online GC equipped with a barrier discharge ionization detector (GC-BID, Shimadzu). All the lines from the reactor to the gas GC were heat traced and were maintained at 423 K to prevent condensation of the products and reactants.

4.3. Results and Discussion

4.3.1. 2-MTHF Conversion over SiO_2/Al_2O_3

The dehydration of 2-MTHF over SiO_2/Al_2O_3 was investigated at 623 K and atmospheric pressure. We observed the formation of *cis* and *trans*-1,3-pentadiene, 1,4-pentadiene, pent-en-ols, pentanal, pent-en-als, butenes as well as C_2-C_3 alkenes. The conversion of 2-MTHF to *trans*-1,3-pentadiene is an endothermic reaction with ΔH^o of 45.8 kJ mol^{-1} and is highly favourable at 623 K (ΔG^o = -76.8 kJ mol^{-1}). We performed a reaction at high conversion of 2-MTHF to determine the yield to pentadienes. The catalyst undergoes continuous deactivation and the 2-MTHF conversion decreases from 100% to 77% over a period of 58 h (Figure 4.3). The yield towards pentadiene decreases from 67.8% to 51.8%. The initial yield to pentadienes is comparable to that observed by Norman over V-Ti-P oxide.[23] The 1,3-pentadiene (*cis* and *trans* combined) and 1,4-pentadiene yields at 58 h are 41.5% and 10.3% respectively. Brønsted acid catalysts are known to catalyze double bond isomerization and the higher yield towards the conjugated diene, 1,3-pentadiene can be explained owing to its higher stability as compared to 1,4-pentadiene.[28]

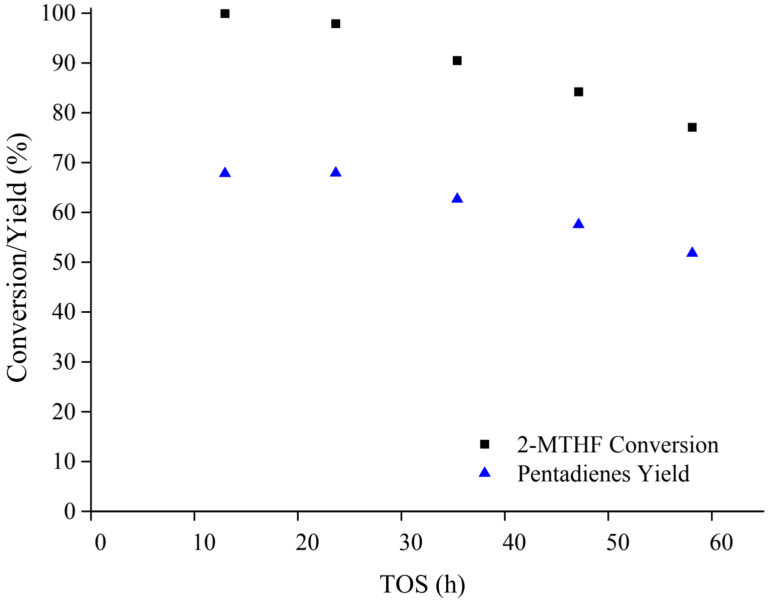

Figure 4.3. 2-MTHF conversion and yield to pentadienes over SiO_2/Al_2O_3. Reaction conditions: 1.0 g catalyst, 10 wt% 2-MTHF in dodecane, 30 cm^3 min^{-1} He, 623 K, 1 atm, WHSV: 0.18 h^{-1}.

4.3.2. Reaction Pathways

The reaction network for ring opening of 2-MTHF to pentadiene was probed using space time studies. Figure 4.4 shows the effect of space time on the selectivity of the various products identified in the reaction. The pentadienes (Figure 4.4(a)) show non-zero initial product selectivity, indicating that they are primary products and are formed directly from 2-MTHF. The selectivity for production of pentadienes also increases with time on stream, suggesting that they can also be formed as secondary products. The selectivity to pent-en-ol and pentanal (Figure 4.4 (b)) at low space times are also non-zero, exhibiting primary product behaviour. The selectivity to pent-en-ol decreases from 19.1% to 7.9% as the space time increases from 10.7 s to 101.3 s, showing that pent-en-ol undergoes further conversion. The selectivity for 1-butene increases with space time, showing an apparent secondary product behaviour. In addition to these products, we observe the formation of pentenes, pent-en-als and C_2-C_3 alkenes.

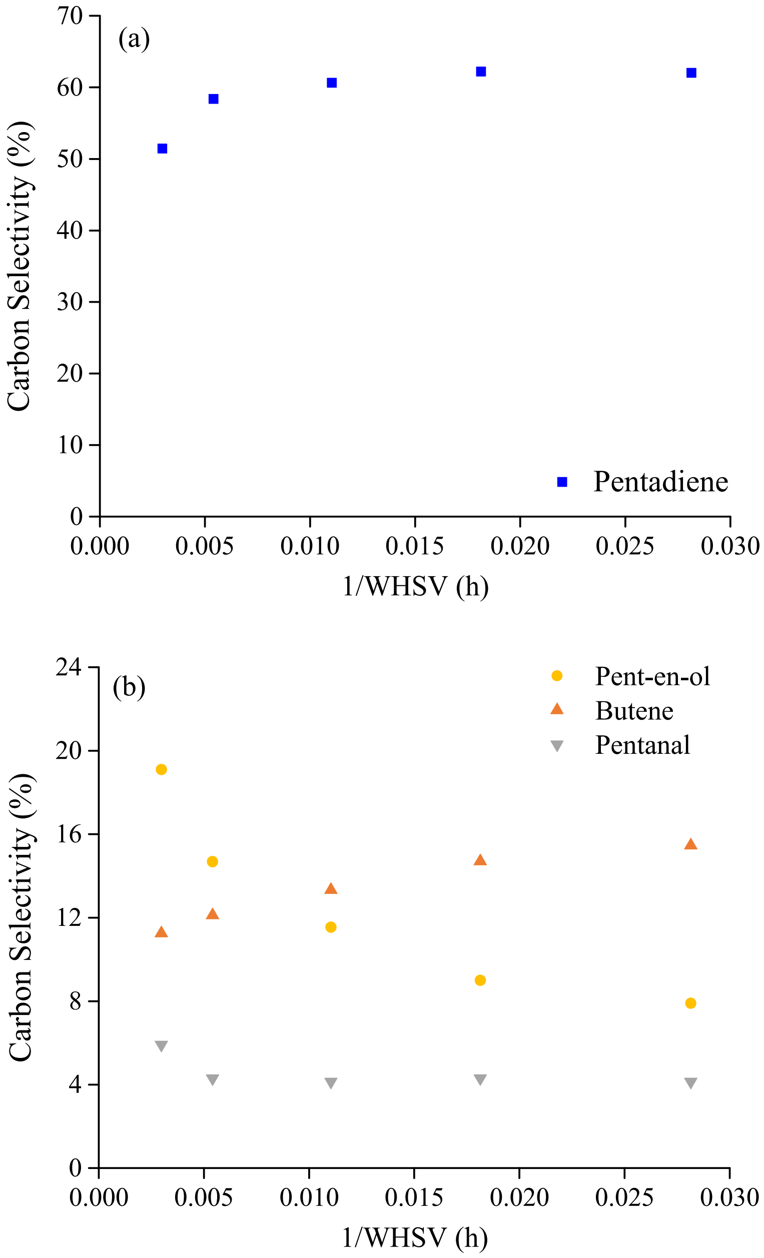

Figure 4.4. Product selectivities vs space times for 2-MTHF ring opening over SiO_2/Al_2O_3. Reaction conditions: 20 wt% 2-MTHF in dodecane, 623 K, 1 atm, WHSV: 35.5- 336 h^{-1}.

There are two positions where the C-O bond can undergo cleavage on 2-MTHF, forming either 2-pentanone or pentanal. The GC-MS fragmentation patterns obtained for carbonyl compounds in the liquid drain confirmed the presence of pentanal. Primary and secondary carbenium ions can be formed during formation of 2-pentanone and pentanal, respectively. Since a secondary carbenium is more stable than a primary carbenium, pentanal formation is favored over that of 2-pentanone. To probe the rate of formation of dienes from pentanal, we conducted experiments with pentanal in dodecane feed, maintaining the same partial pressure as that for 2-MTHF during the space time studies. The specific rate of pentadiene formation from pentanal was 26 μmol g^{-1} min^{-1} which is 30 times lower compared to the pentadiene formation from 2-MTHF (740 μmol g^{-1} min^{-1}) under similar reactions conditions. Also, we do not observe any pent-en-ol in the products during pentanal conversion.

As seen in Figure 4.4, the butene selectivity increases with space time as that of pent-en-ol decreases. We propose that a fraction of pent-en-ols is converted to butene and formaldehyde via reverse Prins reaction over the Lewis acid sites in SiO_2/Al_2O_3. We could not quantify the amount of formaldehyde using GC-FID, but the presence of formaldehyde was confirmed using GC-MS. We thereby assumed equal moles for butene and formaldehyde for quantification. The Prins reaction involves condensation of an aldehyde with an alkene, resulting in the formation of unsaturated alcohols, alkyl dioxanes, and dienes. This acid catalyzed reaction is traditionally catalyzed by homogeneous mineral acids, Lewis acids like $SnCl_4$, as well as solid Lewis acid catalysts. Our findings are also consistent with Travin and co-workers who report reverse Prins reaction of 3-methyl-2-buten-1-ol to form isobutylene and formaldehyde over H_2SO_4 catalyst.[29]

The changes in carbon selectivity with time on stream for the conversion of pure 2-MTHF over SiO_2/Al_2O_3 are shown in Figure 4.5. The conversion based on the products formed decreases from 6.6% at 2 h to 3.8% at 6.1 h time on stream. Since the catalyst undergoes deactivation, the product selectivities at various times during the reaction can be used to understand the reaction network. The pentadiene selectivity decreases with time on stream, whereas pent-en-ol selectivity increases. Based on space time studies, pent-en-ols are primary products, and over a solid acid catalyst we anticipate the enols to undergo dehydration to produce the pentadienes; however, since the catalyst is deactivating, we observe increasing amounts of enols as the reaction progresses. It is important to note that the catalyst is continuously deactivating and the activity shown by a fresh catalyst with a high active site density may be different than the activity shown by a partially deactivated catalyst.

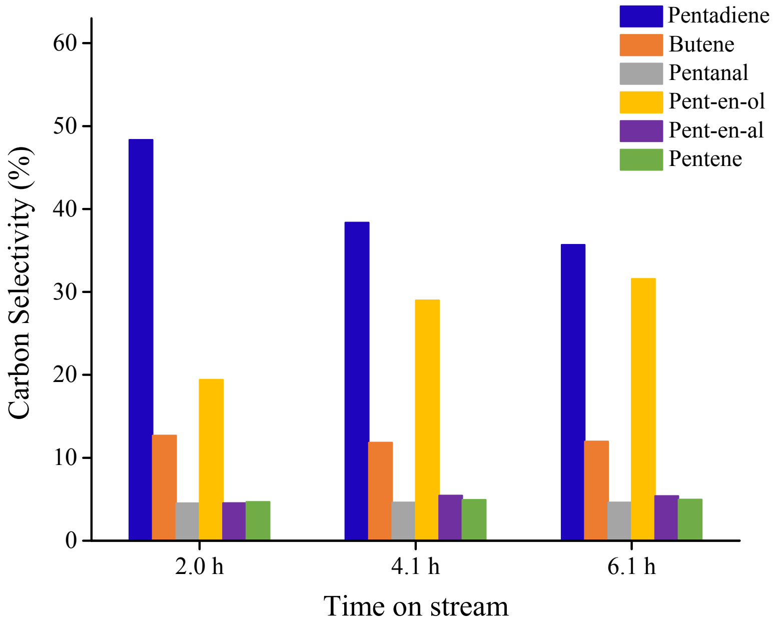

Figure 4.5. Product selectivities with time on stream for a reaction with pure 2-MTHF feed. Reaction conditions: 0.01 g SiO_2/Al_2O_3, pure 2-MTHF feed, 30 cm^3 min^{-1} He, T: 623 K; P: 1 atm.

Based on our findings, we propose a plausible reaction network for 2-MTHF ring opening as shown in Figure 4.6. Attack by a proton from the silica-alumina surface can lead to the formation of a secondary carbenium ion (Figure 4.6, species A) or a primary carbenium ion with a hydroxyl group attached to it (Figure 4.6, species B). The majority of pentadienes are produced via the primary pathway involving concerted hydride-shift, dehydration and deprotonation. Owing to the rearrangement via hydride-shift within the carbenium intermediate, it is possible to form the diene directly without passing through either the enol or aldehyde species. We also propose a secondary pathway to pentadienes through pentanal formation based on reactivity data obtained from reacting pentanal over SiO_2/Al_2O_3. A separate secondary pathway proceeding via pent-en-ol formation and subsequent dehydration is also possible.

In studies involving hydrodeoxygenation of 2-MTHF over metal phosphide catalysts, Oyama *et al*. used space time studies to probe the reaction network.[21,30,31] On WP/SiO_2, the primary products were 1,4-pentadiene, *cis* and *trans*-1,3-pentadiene, and furan. The formation of pent-en-ols and butene was not observed. The authors propose that to produce pentadienes and pentanal, 2-MTHF is bound to two active sites on the catalyst. The 2-MTHF first adsorbs via the ether oxygen atom on the catalyst surface after which a surface nucleophile attacks a carbon in the alpha position to the oxygen to form a doubly bound intermediate species. In the subsequent step, the nearby vacant sites induce β-hydride elimination and release pentadienes. They also observed small amounts of pentanal formed by α-hydride elimination from the primary alkoxide species of the same doubly bound intermediate. Though the details of the mechanism outlined by Oyama *et al.* and in this study are different, both mechanisms explain that dienes and aldehyde come from the same initial intermediates.

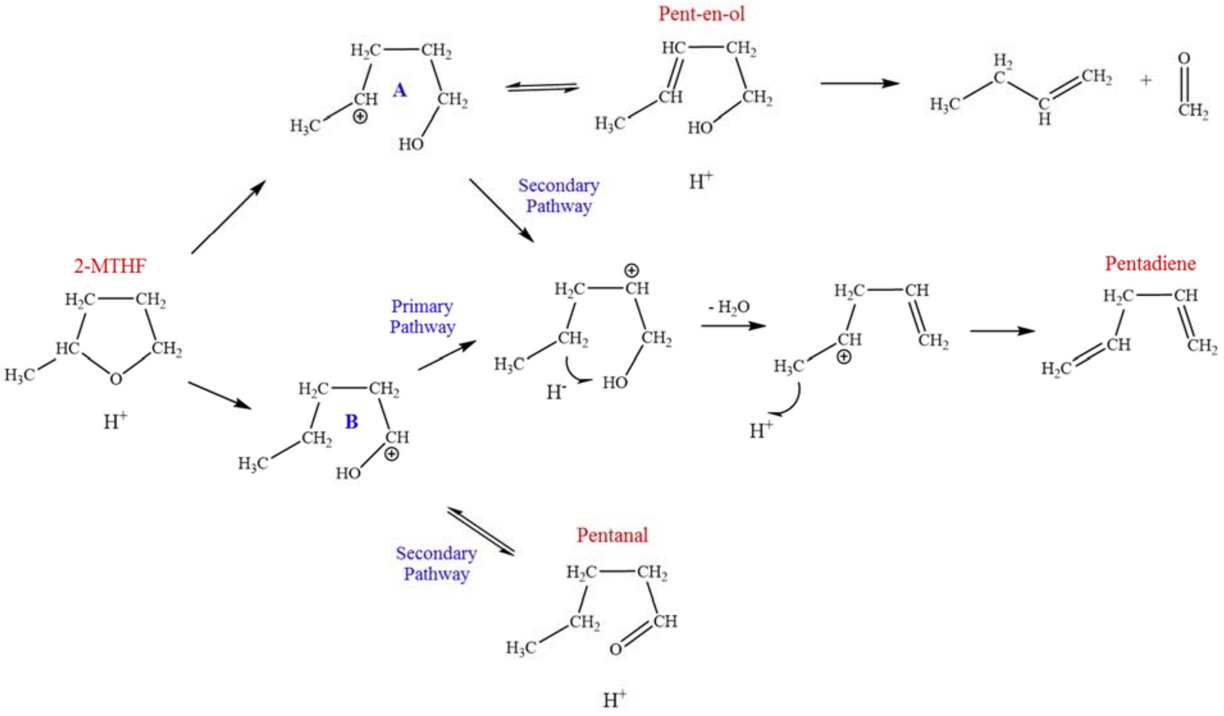

Figure 4.6. Proposed reaction network for 2-MTHF ring opening to pentadiene based on space time studies over SiO_2/Al_2O_3.

4.3.3. Effect of Temperature

We performed reactions in the kinetically controlled regime to determine the apparent activation energy for pentadiene formation over SiO_2/Al_2O_3. Low conversion of 2-MTHF was achieved by decreasing the catalyst amount in the reactor and increasing the feed flow rate. We performed 2-MTHF ring opening reactions at four different temperatures, 573, 603, 623, and 653 K, and collected initial rate data within 10 h for each temperature. As the catalyst undergoes deactivation, the initial rate of pentadiene formation was used to determine the apparent activation energy, E_a. Figure 4.7 summarizes the effect of temperature on the rate of pentadiene formation. The E_a for pentadiene formation is calculated to be 74 ± 7 kJ mol^{-1}.

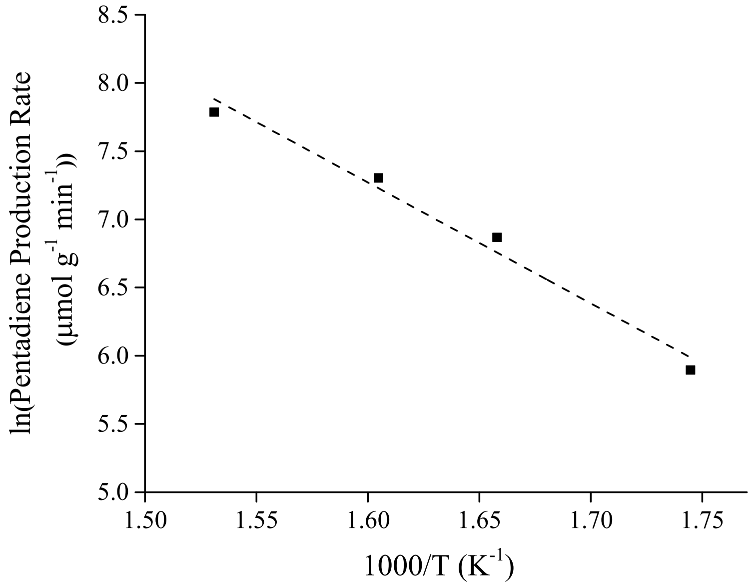

Figure 4.7. Rates of reaction for pentadiene formation at various reaction temperatures. Reaction conditions: 0.01 g SiO_2/Al_2O_3; 10 wt% 2-MTHF in dodecane, 90 cm^3 min^{-1} He, WHSV: 54 h^{-1}; P: 1 atm.

4.3.4. Reaction Rate Order

The partial pressure of 2-MTHF was varied from 0.21–2.51 kPa to obtain the rate order dependence for the ring opening reaction. This variation in partial pressure was achieved by varying the 2-MTHF composition in dodecane as well as the He flow rate. A fractional rate order of 0.24 ± 0.06 with respect to 2-MTHF was obtained as shown in Figure 4.8. The rate of 2-MTHF consumption increases only slightly with increasing 2-MTHF concentration. This behavior can be attributed to a strong interaction between species derived from 2-MTHF and the surface of SiO_2/Al_2O_3, which is in accord with the low experimentally calculated apparent activation energy.

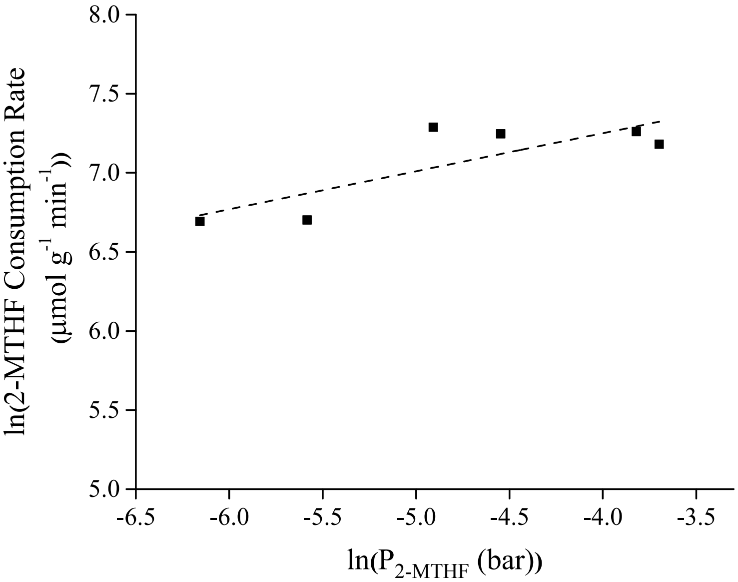

Figure 4.8. Rates of 2-MTHF ring opening over SiO_2/Al_2O_3 at various partial pressures of 2-MTHF at 623 K and 1 atm.

4.3.5. Catalyst Regenerability

We observed catalyst deactivation with time on stream for all the reactions in this study due to coke formation, likely from polymerization of pentadienes. Catalyst regeneration was achieved by calcining the catalyst at 773 K (4 K min^{-1} ramp from room temperature to 773 K, 2 h hold at 773 K) in flowing air. The CO_2 evolution was monitored during calcination using a GC-TCD. The CO_2 peak area increased with temperature and eventually decreased to zero suggesting that coke removal was complete. After calcination, we performed reaction kinetics studies with the same operating conditions. As seen in Figure 4.9, 2-MTHF conversion and the rate of pentadiene formation were similar for the fresh and regenerated catalyst, indicating that the deactivation is reversible. Thus, SiO_2/Al_2O_3 is regenerable upon calcination, with no observable loss in initial catalytic activity.

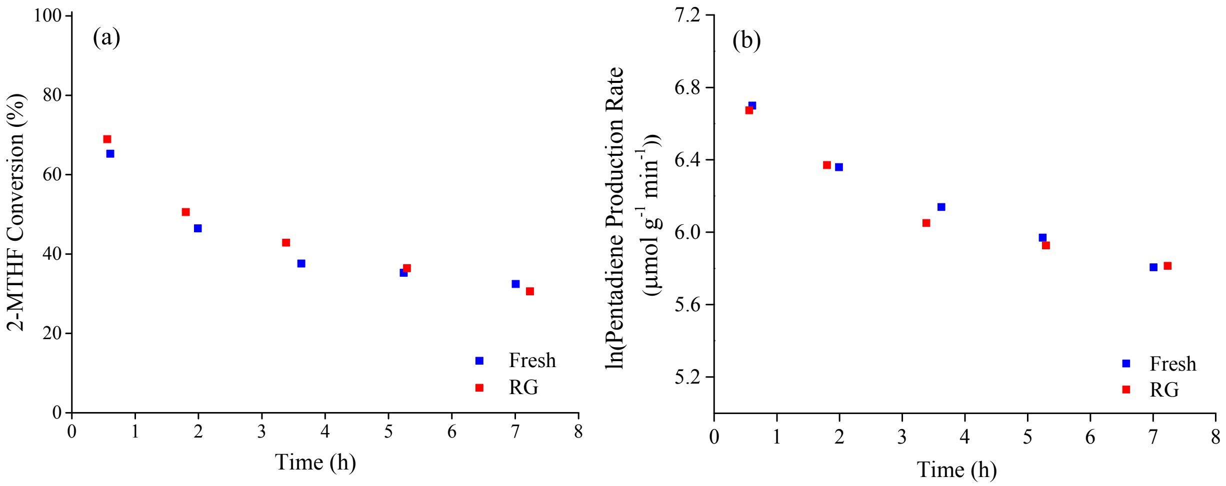

Figure 4.9. (a) 2-MTHF conversion and (b) semi-log plot of pentadiene production rate versus time on stream over fresh (🟦) and regenerated (🟥) SiO_2/Al_2O_3. Reaction conditions: 0.05 g SiO_2/Al_2O_3; 10 wt% 2-MTHF in dodecane feed; T: 623 K; P: 1 atm; WHSV: 11.5 h^{-1}; He flow rate: 90 cm^3 min^{-1}. RG: Regeneration in air at 773 K for 2 h.

We performed a high conversion reaction over 0.15 g of SiO_2/Al_2O_3 to quantify the amount of coke deposited on the catalyst surface. The reaction was carried for 15 h after which the spent catalyst was retrieved after cooling down the reactor at room temperature. Thermogravimetric analysis (TGA) was performed on the spent catalyst in flowing air with a temperature ramp of 10 K min^{-1} to 1073 K (Figure 4.10). We observed a weight loss of 21 wt% after TGA. Assuming the loss in weight to be equal to coke formed, 0.003 moles of carbon were calculated to be deposited on the surface. During the 15 h reaction, 0.45 moles of carbon through 2-MTHF passed over the catalyst. Thus, 0.6 wt% of carbon passed over the catalyst was deposited as coke which is a negligible amount.

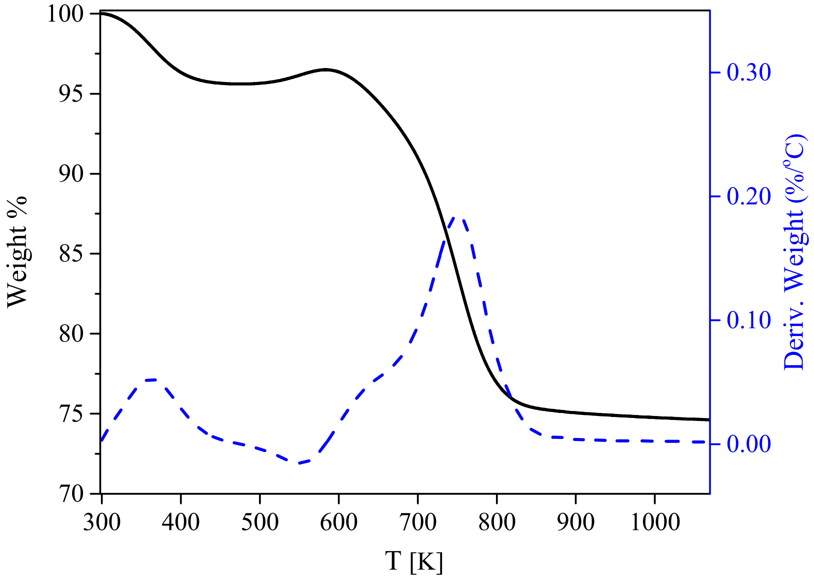

Figure 4.10. Thermogravimetric analysis on SiO_2/Al_2O_3 to quantify the amount of coke deposited. Reaction conditions: 0.15 g SiO_2/Al_2O_3; 10 µL min^{-1} pure 2-MTHF; T: 623 K; P: 1 atm.

4.3.6. 2-MTHF conversion over various solid acids

We further investigated the conversion of 2-MTHF over H-ZSM-5, H-MOR, H-Beta, γ-Al_2O_3, and Al-Sn-Beta. Pentadiene formation was observed over all these catalysts. No conversion of the dodecane solvent was seen during a control experiment over amorphous SiO_2/Al_2O_3 at 623 K and 1 atm. However, we observed conversion of dodecane to form aromatics compounds such as p-xylene, 1-ethyl-2-methyl-benzene, and 1,2,4-trimethyl-benzene, and cracking products, such as hexane and heptane, over H-ZSM-5. Mi and co-workers observed the formation of aromatics during dodecane cracking at 673 K over H-ZSM-5.[32] The amount of carbon present in the undesired aromatics and cracking products corresponded to approximately 10% of the total carbon detected in all the products. We did not observe the formation of aromatics over γ-Al_2O_3 and the niobium-based acids. Experiments performed over Nb_2O_5 and $NbOPO_4$ showed pentadiene formation initially but these catalysts deactivated completely within 4 to 6 h time on stream. Both these niobium acids are white powders but upon removal from the reactor, the spent catalysts were black in color suggesting deactivation due to coke deposition. XRD showed that both the fresh and spent catalysts are amorphous (Figure 4.11) indicating that the decrease in surface area is not due phase change from amorphous to crystalline. The catalyst deactivation could be due to coke formation and decrease in surface area.

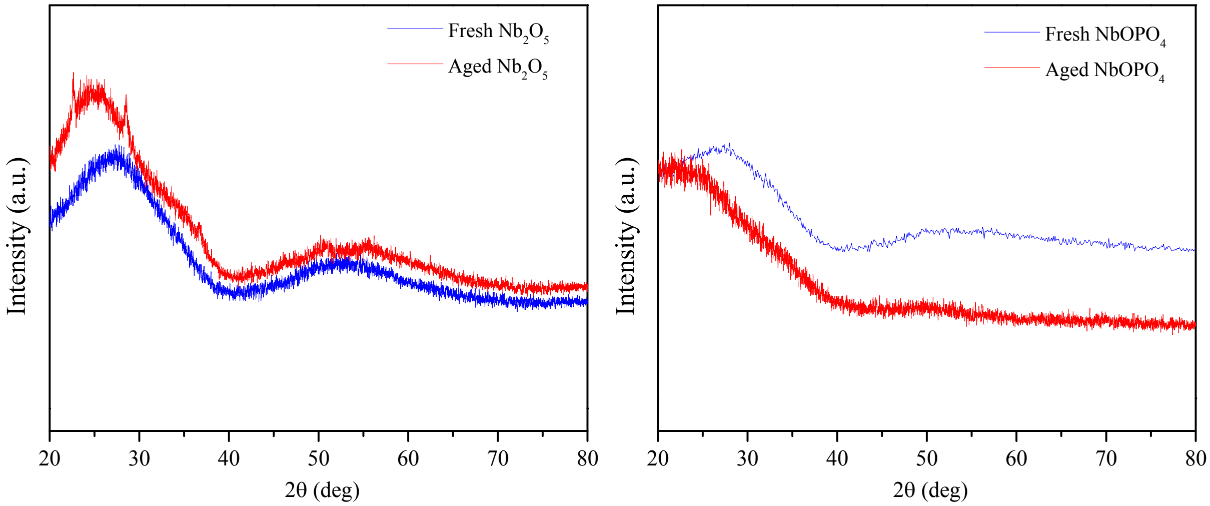

Figure 4.11. Powder X-ray diffraction of fresh and spent (a) Nb_2O_5 and (b) $NbOPO_4$.

Pentadiene formation turnover frequencies (TOF) were obtained by normalizing specific rates with the Brønsted acid site densities. The Brønsted acid site (BAS) and Lewis acid site (LAS) densities for these catalysts were taken from literature except that for SiO_2/Al_2O_3 and H-ZSM-5 which were calculated using NH_3-TPD and IPA-TPD.[33] A primarily Lewis solid acid, γ-Al_2O_3, was also active for the formation of pentadiene, however, the rate was lower as compared to SiO_2/Al_2O_3. The initial rates of production of pentadiene over SiO_2/Al_2O_3 and γ-Al_2O_3 were 496 and 155 μmol g^{-1} min^{-1}, respectively. All the catalysts underwent deactivation as the reaction progressed. The pentadiene TOF over SiO_2/Al_2O_3 decreased from 0.97 min^{-1} to 0.45 min^{-1} over 10 h. The initial pentadiene TOF values calculated at time zero were found to be similar for all the solid acids mentioned in Table 4.2. The niobium-based solid acids are not included in the table as rapid deactivation was observed within a few hours of the start of the reaction. The first order deactivation constants were calculated by plotting the semi-log plot of pentadiene formation versus time on stream. SiO_2/Al_2O_3 had the lowest deactivation constant.

Table 4.2. Pentadiene formation per Brønsted acid site and first order deactivation constants over various solid acids for 2-MTHF ring opening.

Catalyst	**$SiO_2:Al_2O_3$**	**BAS (μmol g^{-1})**	**LAS (μmol g^{-1})**	**Pentadiene TOF (min^{-1})**	**$k_d \times 10^3$ (min^{-1})**
SiO_2/Al_2O_3	10.7	537	145	0.92	1.4
H-ZSM-5	23.0	652	48	0.93	2.0
H-BEA	25.0	269	162	0.85	1.8
H-MOR	20.0	331	71	0.85	2.2

We compared the product selectivities over various solid acids at similar levels of conversion (~35%) in Figure 4.12. The highest pentadiene selectivity of ~70% was observed over SiO_2/Al_2O_3, H-ZSM-5, and Al-Sn-BEA. The other products include butene, pentanal, pent-en-ols, pent-en-als, and pentene. The predominantly Lewis acid catalyst, γ-Al_2O_3, had the highest butene and pent-en-ol selectivities. The Lewis acid site density for γ-Al_2O_3 was determined to be 210 μmol/g and no IPA decomposition to propylene was observed, indicating the absence of Brønsted acid sites. The reactors were loaded with equal amounts (0.05 g) of catalyst for SiO_2/Al_2O_3 and γ-Al_2O_3. Butene selectivities over SiO_2/Al_2O_3 and γ-Al_2O_3 are 17.5% and 21.7% respectively. The conversion of allylic alcohol to an alkene and aldehyde (reverse Prins reaction), i.e. conversion of pent-en-ol to butene and formaldehyde in this scenario, is catalyzed by Lewis acid sites. Since γ-Al_2O_3 possesses a higher number of Lewis acid sites, a higher selectivity to butene is observed.

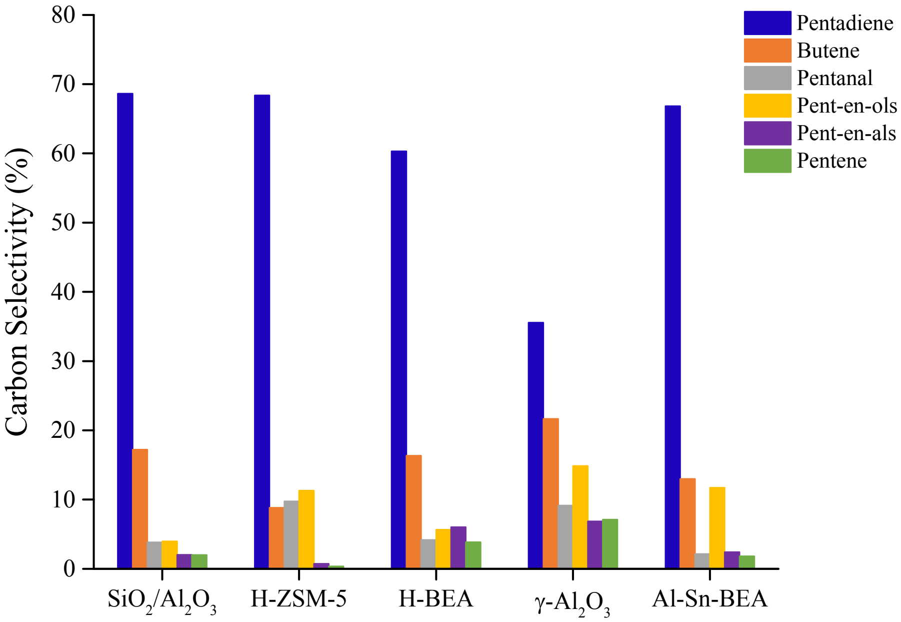

Figure 4.12. Product selectivities for 2-MTHF conversion over different catalysts at 623 K. The selectivities were compared at ~35% conversion.

4.3.7. Ring Opening of other heterocyclics

Cyclic ethers such as tetrahydrofurans and tetrahydropyrans are other heterocyclics formed during hydrodeoxygenation of C_6 polyols.[34,35] We studied the ring opening of tetrahydrofuran, tetrahydropyran, and 2,5-dimethyltetrahydrofuran over SiO_2/Al_2O_3. Dehydration of THP resulted in same set of products as for 2-MTHF- pentadienes, pentenes, pentanal, pent-en-ols, pent-en-als, and butene. Over SiO_2/Al_2O_3, the ring opening of THF showed formation of butadiene, butanal, butenes, propene, and formaldehyde. We did not, however, see the formation of but-en-ol. The products observed during the dehydration of 2,5-DMTHF are hexadienes, 2-hexanone, hex-en-ones, butenes, and acetaldehyde. The hexadiene isomers included 1,5-hexadiene, *cis* and *trans* mixtures of 1,3-hexadienes, 1,4-hexadienes, and 2,4-hexadienes. As in the case of THF, we did not see any enols (hex-en-ols in the case of 2,5-DMTHF) in the product stream. The possible mechanisms for ring opening of THF and 2,5-DMTHF are shown in Figure 4.13. For both THF and 2,5-DMTHF, we observe formation of the carbonyl compounds (i.e. butanal and 2-hexanone, respectively) whereas the enol species are not seen. We speculate that the pathway for formation of the carbonyl compound is favored, as carbenium ions (Figure 4.13, species D and species F) with hydroxyl group attached to the carbon bearing the positive charge are more stable than species C and E. This behavior is in agreement with work involving C-O hydrogenolysis of cyclic ethers by Chia *et al.* who found that the presence of hydroxyl substituent alpha to the dehydration center increases the stability of the carbenium ion.[36] The dehydration of THP proceeds in a pathway similar as that for THF. The rates of pent-en-ol formation starting from 2-MTHF and THP are 122.2 and 1.2 μmol g^{-1} min^{-1} respectively. The lower specific rate for pent-en-ol formation for THP can again be explained based on the relative stability of the carbenium intermediates.

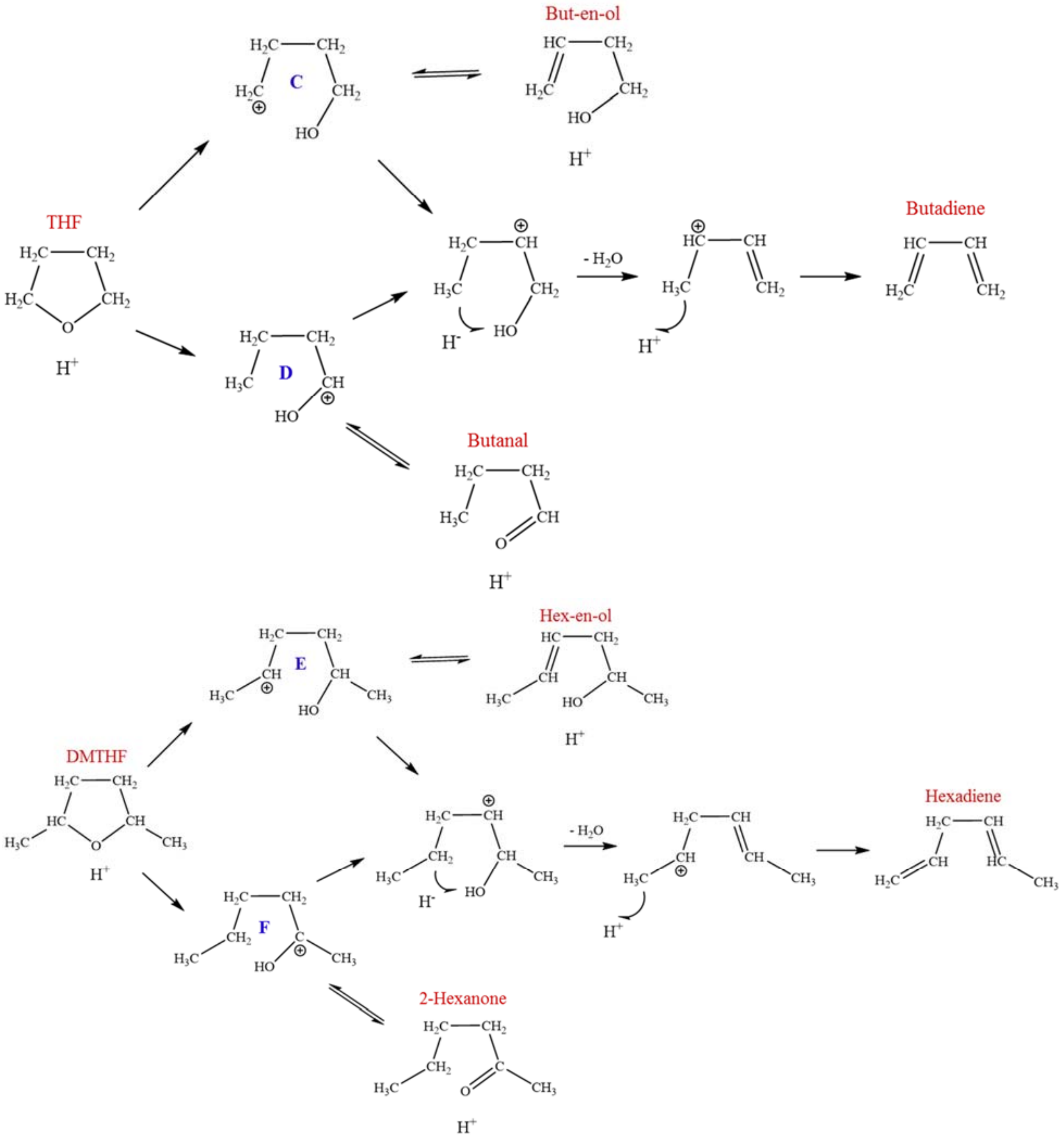

Figure 4.13. Proposed mechanisms for ring opening of tetrahydrofuran (THF) and 2,5-dimethyltetrahydrofuran (2,5-DMTHF) over SiO_2/Al_2O_3.

As discussed earlier, the ring opening of 2-MTHF can proceed via formation of primary or secondary carbenium ions. However, for 2,5-DMTHF, the dehydration can proceed only via secondary carbenium ion formation. Dehydration for both THF and THP, which do not have the methyl branching, can proceed only by primary carbenium ion formation. The rates of ring opening of these cyclic ethers were compared by performing experiments in the differential conversion regime for the same partial pressure of the reactant (Table 4.3). The flow rates of the cyclic ether and the inert carrier gas helium were adjusted to maintain the initial partial pressure at 2.4 kPa. The lowest rate of ring opening was observed for THF. Among the C_5 ethers, 2-MTHF and THP, the rate of ring opening of the former was ~92% higher. We hypothesize that the rate of 2-MTHF dehydration is higher than that of THP owing to the higher stability of secondary carbenium ion as compared to that of the primary carbenium ion. 2,5-DMTHF can undergo ring opening via two routes to form a secondary carbenium ion and thus showed the highest rate of dehydration.

Table 4.3. Rates of ring opening of various heterocyclics over SiO_2/Al_2O_3 at 623 K and 1 atm.

Heterocyclics		**Conversion (%)**	**Rate of Ring Opening (μmol g^{-1} min^{-1})**
Structure	**Name**		
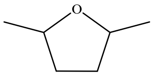	2,5-DMTHF	20.2	6573.7
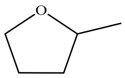	2-MTHF	14.8	2678.6
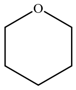	THP	7.3	1397.3
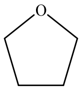	THF	10.1	1096.8

The C_6 diene, *trans*-1,4-hexadiene, is used in the production of ethylene-propylene-diene monomer and is produced via ethylene and 1,3-butadiene codimerization. Behr and Miao have shown 40.3% yield to *trans*-1,4-hexadiene by the codimerization of 1,3-butadiene and ethylene in water and propylene glycol solvent over $RhCl_3$.[37] In our study, a high conversion reaction for 2,5-DMTHF showed a change in conversion from 85.4% to 75.3% over 8.3 h time on stream (Figure

4.14). Throughout the reaction, a high selectivity to hexadiene isomers, particularly cis and trans 2,4-hexadiene isomers, was observed. Nearly 75% yield towards hexadienes is observed under these reactions conditions.

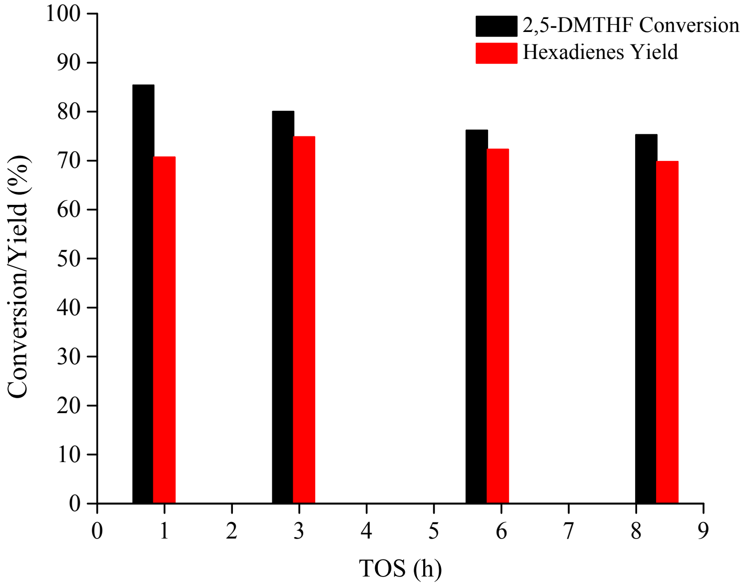

Figure 4.14. 2,5-DMTHF conversion and hexadienes yield. Reaction conditions: 0.01 g SiO_2/Al_2O_3, 5 wt% 2,5-DMTHF in dodecane, 60 cm^3 min^{-1} He, T: 623 K; WHSV: 13.3 h^{-1}; P: 1 atm.

4.4. Conclusions

We have shown that cyclic ethers can undergo ring opening to produce dienes in high yields over solid acid catalysts. Based on space time studies and changes in product distribution with time on stream, we have proposed a reaction network for 2-MTHF dehydration over SiO_2/Al_2O_3. Ring opening occurs via both a primary concerted pathway involving hydride-transfer and dehydration of a carbenium intermediate, and a secondary pathway passing through the formation of pentanal and pent-en-ols. The catalyst deactivates as the reaction progresses, but this deactivation is reversible and the initial activity of the catalyst is fully restored upon calcination in air. A fractional rate order dependence with 2-MTHF is observed due to high surface coverage. The apparent activation energy for 2-MTHF dehydration was calculated to be 74 kJ mol^{-1}. Other solid acids with both Brønsted and Lewis acid sites were active for the dehydration reaction to dienes with the catalytic activity for dienes formation being proportional to the concentration of Brønsted acid sites on the catalyst. Amongst the various cyclic ethers, 2,5-DMTHF showed the highest activity towards dehydration, resulting in the formation of hexadienes with ~75% yield at 623 K.

4.5. Acknowledgements

The contents of this chapter are a part of a manuscript submitted to ACS Catalysis. This work was funded by ExxonMobil.

4.6. References

1. Huber, G. W.; Iborra, S.; Corma, A., Synthesis of transportation fuels from biomass: Chemistry, catalysts, and engineering. *Chem. Rev.* 2006, *106* (9), 4044-4098.
2. Alonso, D. M.; Bond, J. Q.; Dumesic, J. A., Catalytic conversion of biomass to biofuels. *Green Chem.* 2010, *12* (9), 1493-1513.
3. Pace, V.; Hoyos, P.; Castoldi, L.; de Maria, P. D.; Alcantara, A. R., 2-Methyltetrahydrofuran (2-MeTHF): A Biomass-Derived Solvent with Broad Application in Organic Chemistry. *ChemSusChem* 2012, *5* (8), 1369-1379.
4. Jessop, P. G., Searching for green solvents. *Green Chem.* 2011, *13* (6), 1391-1398.
5. Elliott, D. C.; Frye, J. G., Hydrogenated 5-carbon compound and method of making. *U.S. Patent US5883266A* 1999.
6. Xing, R.; Qi, W.; Huber, G. W., Production of furfural and carboxylic acids from waste aqueous hemicellulose solutions from the pulp and paper and cellulosic ethanol industries. *Energy Environ. Sci.* 2011, *4* (6), 2193-2205.
7. Dumesic, J. A.; Alonso, D. M.; Gürbüz, E. I.; Wettstein, S. G., Production of levulinic acid, furfural, and gamma valerolactone from C5 and C6 carbohydrates in mono- and biphasic systems using gamma-valerolactone as a solvent. *US 8,399,688 B2* 2013.
8. Zeitsch, K. J., *The Chemistry and Technology of Furfural and its Many by-products*. Elsevier, The Netherlands: 2000.
9. Dong, F.; Zhu, Y. L.; Ding, G. Q.; Cui, J. L.; Li, X. Q.; Li, Y. W., One-step Conversion of Furfural into 2-Methyltetrahydrofuran under Mild Conditions. *ChemSusChem* 2015, *8* (9), 1534-1537.
10. Kunkes, E. L.; Simonetti, D. A.; West, R. M.; Serrano-Ruiz, J. C.; Gartner, C. A.; Dumesic, J. A., Catalytic conversion of biomass to monofunctional hydrocarbons and targeted liquid-fuel classes. *Science* 2008, *322* (5900), 417-421.
11. Blommel, P.; Dally, B.; Lyman, W.; Cortright, R., Method and systems for making distillate fuels from biomass. *US20120198760 A1* 2012.

12. Eagan, N. E.; Chada, J. P.; Wittring, A. M.; Buchanan, J. S.; Dumesic, J. A.; Huber, G. W., Aqueous-Phase Hydrodeoxygenation of Sorbitol to Monofunctional Fuel Precursors over Co/TiO2 *In preparation*.
13. Huber, G. W.; Chheda, J. N.; Barrett, C. J.; Dumesic, J. A., Production of liquid alkanes by aqueous-phase processing of biomass-derived carbohydrates. *Science* 2005, *308* (5727), 1446-1450.
14. Behr, A.; Neubert, P., Piperylene-A Versatile Basic Chemical in Catalysis. *ChemCatChem* 2014, *6* (2), 412-428.
15. Neubert, P.; Fuchs, S.; Behr, A., Hydroformylation of piperylene and efficient catalyst recycling in propylene carbonate. *Green Chem.* 2015, *17* (7), 4045-4052.
16. Maes, M.; Alaerts, L.; Vermoortele, F.; Ameloot, R.; Couck, S.; Finsy, V.; Denayer, J. F. M.; De Vos, D. E., Separation of C-5-Hydrocarbons on Microporous Materials: Complementary Performance of MOFs and Zeolites. *J. Am. Chem. Soc.* 2010, *132* (7), 2284-2292.
17. Schniepp, L. E.; Geller, H. H., The Preparation of 1,3- and 1,4-Pentadienes from Furfural. *J. Am. Chem. Soc.* 1945, *67* (1), 54-56.
18. Kundu, S.; Lyons, T. W.; Brookhart, M., Synthesis of Piperylene and Toluene via Transfer Dehydrogenation of Pentane and Pentene. *ACS Catal.* 2013, *3* (8), 1768-1773.
19. Kumar, A.; Hackenberg, J. D.; Zhuo, G.; Steffens, A. M.; Mironov, O.; Saxton, R. J.; Goldman, A. S., High yields of piperylene in the transfer dehydrogenation of pentane catalyzed by pincer-ligated iridium complexes. *J. Mol. Catal. A-Chem.* 2017, *426*, 368-375.
20. Dumesic, J. A.; Chia, M., Production of 2,4-hexadienoic acid and 1,3-pentadiene from 6-methyl-5,6-dihydro-2-pyrone. *U.S. Patent US8404890B2* 2013.
21. Bui, P.; Cecilia, J. A.; Oyama, S. T.; Takagaki, A.; Infantes-Molina, A.; Zhao, H. Y.; Li, D.; Rodriguez-Castellon, E.; Lopez, A. J., Studies of the synthesis of transition metal phosphides and their activity in the hydrodeoxygenation of a biofuel model compound. *J. Catal.* 2012, *294*, 184-198.
22. Johns, I. B., Method of preparing an elastomer. *U.S. Patent US2458001* 1949.
23. Norman, D. W., Catalytic dehydration of alcohols and ethers over a ternary mixed oxide. *U.S. Patent US8981172B2* 2015.
24. Vannice, M. A., *Kinetics of Catalytic Reactions*. Springer US: 2005.
25. McCabe, W.; Smith, J.; Harriott, P., *Unit Operations of Chemical Engineering*. McGraw-Hill Education: 2005.
26. Hill, C. G.; Root, T. W., *Introduction to Chemical Engineering Kinetics and Reactor Design*. Wiley: 2014.
27. Frisch, M. J.; Trucks, G. W.; Schlegel, H. B.; Scuseria, G. E.; Robb, M. A.; Cheeseman, J. R.; Scalmani, G.; Barone, V.; Mennucci, B.; Petersson, G. A.; Nakatsuji, H.; Caricato, M.; Li, X.; Hratchian, H. P.; Izmaylov, A. F.; Bloino, J.; Zheng, G.; Sonnenberg, J. L.; Hada, M.; Ehara, M.; Toyota, K.; Fukuda, R.; Hasegawa, J.; Ishida, M.; Nakajima, T.; Honda, Y.; Kitao, O.; Nakai, H.; Vreven, T.; Montgomery Jr., J. A.; Peralta, J. E.; Ogliaro, F.; Bearpark, M. J.; Heyd, J.; Brothers, E. N.; Kudin, K. N.; Staroverov, V. N.; Kobayashi, R.; Normand, J.; Raghavachari, K.; Rendell, A. P.; Burant, J. C.; Iyengar, S. S.; Tomasi, J.; Cossi, M.; Rega, N.; Millam, N. J.; Klene, M.; Knox, J. E.; Cross, J. B.; Bakken, V.; Adamo, C.; Jaramillo, J.; Gomperts, R.; Stratmann, R. E.; Yazyev, O.; Austin, A. J.; Cammi, R.; Pomelli, C.; Ochterski, J. W.; Martin, R. L.; Morokuma, K.; Zakrzewski, V. G.; Voth, G. A.; Salvador, P.; Dannenberg, J. J.; Dapprich, S.; Daniels, A. D.; Farkas, Ö.; Foresman, J. B.; Ortiz, J. V.; Cioslowski, J.; Fox, D. J. *Gaussian 09*, Gaussian, Inc.: Wallingford, CT, USA, 2009.

28. Buchanan, J. S.; Santiesteban, J. G.; Haag, W. O., Mechanistic considerations in acid-catalyzed cracking of olefins. *J. Catal.* 1996, *158* (1), 279-287.
29. Ryabova, R. S.; Osipova, G. F.; Travin, S. O., Kinetic scheme of homogeneous acid-catalyzed transformation of isopentenols. *Russian Chemical Bulletin* 1995, *44* (5), 840-843.
30. Bui, P. P.; Oyama, S. T.; Takagaki, A.; Carrow, B. P.; Nozaki, K., Reactions of 2-Methyltetrahydropyran on Silica-Supported Nickel Phosphide in Comparison with 2-Methyltetrahydrofuran. *ACS Catal.* 2016, *6* (7), 4549-4558.
31. Iino, A.; Cho, A.; Takagaki, A.; Kikuchi, R.; Oyama, S. T., Kinetic studies of hydrodeoxygenation of 2-methyltetrahydrofuran on a Ni2P/SiO2 catalyst at medium pressure. *J. Catal.* 2014, *311*, 17-27.
32. Xian, X. C.; Liu, G. Z.; Zhang, X. W.; Wang, L.; Mi, Z. T., Catalytic cracking of n-dodecane over HZSM-5 zeolite under supercritical conditions: Experiments and kinetics. *Chemical Engineering Science* 2010, *65* (20), 5588-5604.
33. Kubicka, D.; Kumar, N.; Maki-Arvela, P.; Tiitta, M.; Niemi, V.; Karhu, H.; Sami, T.; Murzin, D. Y., Ring opening of decalin over zeolites - II. Activity and selectivity of platinum-modified zeolites. *J. Catal.* 2004, *227* (2), 313-327.
34. Kim, Y. T.; Dumesic, J. A.; Huber, G. W., Aqueous-phase hydrodeoxygenation of sorbitol: A comparative study of Pt/Zr phosphate and Pt-ReOx/C. *J. Catal.* 2013, *304*, 72-85.
35. West, R. M.; Kunkes, E. L.; Simonetti, D. A.; Dumesic, J. A., Catalytic conversion of biomass-derived carbohydrates to fuels and chemicals by formation and upgrading of mono-functional hydrocarbon intermediates. *Catal. Today* 2009, *147* (2), 115-125.
36. Chia, M.; Pagan-Torres, Y. J.; Hibbitts, D.; Tan, Q. H.; Pham, H. N.; Datye, A. K.; Neurock, M.; Davis, R. J.; Dumesic, J. A., Selective Hydrogenolysis of Polyols and Cyclic Ethers over Bifunctional Surface Sites on Rhodium-Rhenium Catalysts. *J. Am. Chem. Soc.* 2011, *133* (32), 12675-12689.
37. Behr, A.; Miao, Q., Selective rhodium catalysed synthesis of trans-1,4-hexadiene in polyethylene glycol 1000-water solvent systems. *Green Chem.* 2005, *7* (8), 617-620.

CHAPTER 5

Alkane Dehydrogenation in Endothermic Cooling Systems

5.1. Introduction

For airborne vehicles, as the speed approaches higher Mach numbers, the temperature of the outside air rises significantly and induces heat load stress on the vehicle structure. Hypersonic flights require substantial cooling of engine and other vehicle components by means of endothermic fuels.[1,2]. There has been a great interest in the use of hydrocarbon fuel as coolant, which can dissipate heat from aircraft systems under high pressure (>500 psi) and high temperature (>723 K). To sufficiently lower the temperature of the aircraft components, the cooling cannot rely solely on the physical heat exchange; it has to promote the reactions that absorb the energy excess by driving endothermic reactions such as dehydrogenation and cracking.[3-5] These endothermic reactions can be significantly improved by the use of catalysts that can not only lower the reaction temperature, but also change the action pathways by reducing pyrolysis. Since dehydrogenation is an endothermic reaction and leads to an increase in number of moles, it is favored at elevated temperatures and low pressures, although these high temperatures might also promote side reactions such as hydrogenolysis, oligomerization, isomerization, and coking. The formation of carbonaceous deposits can clog the fuel system and cause engine failure.[3] Several studies have been performed to develop and modify new catalysts to enhance selectivity towards dehydrogenation and minimize coke formation.[5-7]

Platinum group metals are suitable catalysts for alkane dehydrogenation. Extensive experimental[8-11] and theoretical work[12-14] has been carried out to study adsorption and reactions of C_2 hydrocarbon species over Pt catalysts. For example, Sinfelt *et al.*[8] studied the kinetics of ethane hydrogenolysis to methane and reported that the rate of hydrogenolysis is the first order of ethane pressure and decreases with increasing hydrogen pressure. Dehydrogenation of ethane[15,16], propane[15,17-19], and isobutane[20,21] has been widely studied over supported Pt catalysts. Dumesic and co-workers have conducted thorough experimental and theoretical study on ethane hydrogenolysis,[11,22] stability and reactivity of C_2H_x species[23] over Pt catalysts. It was found that the step edge of Pt(211) binds C_2H_x species more strongly than Pt(111) and the primary pathways for ethane hydrogenolysis on Pt involve highly dehydrogenated species. On Pt catalysts, alkenes further dehydrogenate to alkynes and C-C bond cracking may occur. This generates coke precursor and leads to carbon deposition and deactivation of the catalysts. To mitigate coke formation and improve catalyst activity and achieve better selectivity, possible means includes alloying Pt with Sn[16,19,24,25] and co-feeding hydrogen[26,27] with alkanes. We have studied the dehydrogenation of ethane and isobutane over Pt and PtSn catalysts over various supports with and without hydrogen co-feeding.

For the catalytic oxidative dehydrogenation of ethane, Stair and co-workers have achieved coking and sintering resistant Pd catalysts by overcoating the catalysts with alumina using atomic layer deposition.[28] O'Neill *et al.* have shown that atomic layer deposition of an alumina overcoat stabilizes Cu catalyst for liquid-phase catalytic reactions.[29] The stability was ascribed to selective armoring of under-coordinated copper atoms on the nanoparticle surface. Considering that the under-coordinated edge sites at the step of Pt nanoparticles bind hydrocarbon species more strongly than the terrace and could catalyze deep dehydrogenation to form coke precursors, the selectivity of Pt catalysts could be improved if the highly reactive edge sites are blocked by alumina overcoats. Atomic layer deposition was employed to synthesize alumina overcoated Pt catalysts with varying thickness and the effect of overcoating was investigated on the activity towards ethane dehydrogenation.

5.2. Materials and Methods

5.2.1. Catalyst preparation

5.2.1.1 Incipient Wetness Impregnation and Ion Exchange

Monometallic Pt/SiO_2, Pt/γ-Al_2O_3, bimetallic PtSn/SiO_2 and PtSn/K-L-Zeolite catalysts with varying Pt to Sn atomic ratios were synthesized using methods described in Chapter 2, Section 2.2.1. Briefly, Pt was added to SiO_2 by ion exchange method of Benesi *et al*.[30] To measure the Pt loading, we used ICP-AES. Set Pt:Sn atomic ratio catalysts were prepared (Table 5.1). Tin was added to the Pt/SiO_2 catalyst by evaporative impregnation of a solution of tributyltin acetate in pentane. Monometallic Pt catalyst supported on SiO_2 was also prepared by incipient wetness impregnation with aqueous solutions of tetraammineplatinum(II) nitrate precursor ($Pt(NH_3)_4(NO_3)_2$, Sigma-Aldrich) and the subsequent calcination-reduction-passivation treatment. The silica-supported monometallic Pt catalysts prepared using ion exchange and incipient impregnation methods were studied for catalytic cracking of n-dodecane under supercritical conditions.[31] The K-L-Zeolite was first baked in dry air at 873 K for 18 h to remove all the chemisorbed water before addition of Pt.[32] Pt was impregnated onto KLZ using a solution of $Pt(NH_3)_4(NO_3)_2$ in deionized water under inert atmosphere. Sn was incorporated in the same way using tributyltin acetate as the precursor. The routine of calcination-reduction-passivation followed as above for SiO_2 catalyst. Alumina-supported monometallic Pt catalyst was prepared by incipient wetness method.

Table 5.1. Synthesis method and elemental composition of the Pt and PtSn catalysts.

Catalyst	Pt (wt%)	Sn (wt%)	Pt:Sn atomic ratio	Synthesis Method
Pt/SiO_2	1.9	-	1:0	Ion exchange, pH=8
$PtSn/SiO_2$	1.9	1.2	1:1	Ion exchange, pH=8
$PtSn/SiO_2$	1.9	3.4	1:3	Ion exchange, pH=8
$Pt/\gamma\text{-}Al_2O_3$	1.0	-	1:0	Incipient Wetness
PtSn/KLZ	0.6	0.7	1:2	Incipient Wetness

5.2.1.2. Atomic Layer Deposition

The parent $Pt/\gamma\text{-}Al_2O_3$ catalyst was overcoated with alumina using atomic layer deposition (ALD). This technique is a self-limiting growth process that provides highly conformal coatings.[33] Amorphous alumina overcoat was deposited by precursor-purge cycles of alternate exposure to trimethylaluminum and water at 473 K in a fluidized bed reactor in Chapter 2.[34] The parent and alumina overcoated catalysts are termed as non-overcoated $Pt/\gamma\text{-}Al_2O_3$ and $xALD/Pt/\gamma\text{-}Al_2O_3$ (x equals number of ALD cycles), respectively. The number of surface Pt atoms (Pt_s) was calculated using volumetric uptakes of CO at 308 K.

5.2.2. Reaction Studies and product analysis

Reaction studies of all the alkanes studied- ethane and isobutane were conducted in a down-flow SS tube reactor (Figure 5.1). Alkane dehydrogenation is limited by chemical equilibrium and for lighter paraffins, high temperature is required for significant conversion. The experiments were performed in the temperature range of 723-873 K and pressure of 1 atm with He (Airgas) as a carrier gas. The flow rates were controlled using Brooks mass flow controllers and for temperature control, PID controller (Love Controls) with a K-type thermocouple (Omega) was used. All the data was taken in the kinetic regime. The feed flow rate and mass of catalyst were adjusted to keep the conversion around 20% of equilibrium conversion. Before each reaction, the catalyst was reduced in flowing H_2 at 773 K for 1 h and then brought to the reaction temperature before feeding the reactant gas mixture. The partial pressure of the alkane under study was maintained at 12.5 Torr with 0-200 Torr of hydrogen, and balance helium for a total pressure of 760 Torr.

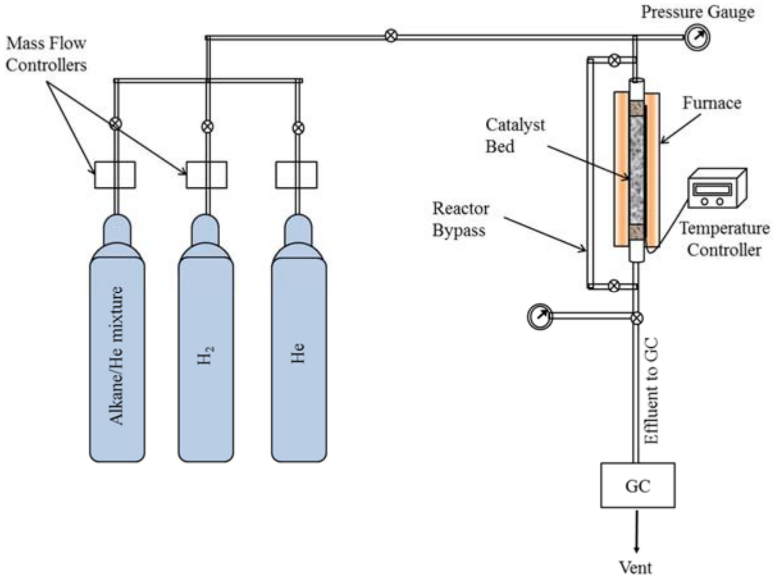

Figure 5.1. Flow reactor schematic for alkane dehydrogenation studies.

Identification of products in the gas phase was performed using a GC-MS. Quantitative analyses were performed for this gas phase reaction using a gas chromatograph equipped with both FID and TCD detectors. The effluent from the reactor was fed straight into this GC, thus maintaining a real-time operation. This was an advantage given the time scale of deactivation of catalyst.

The effect of ALD overcoating was probed for ethane dehydrogenation using the aforementioned reactor. The experiments were performed at 873 K and the data was collected in the kinetic region. Initial ethane reactivities were measured using a feed mixture containing 12.5 Torr ethane, 0-50 Torr hydrogen and balance helium for a total pressure of 1 atm. Reactants and products were quantified using the analytical methods described earlier.

5.3. Results and Discussion

5.3.1. Catalyst characterization

The turnover frequencies for alkane dehydrogenation were calculated based on the number of surface platinum atoms determined by CO uptake at 308 K. We assumed a stoichiometry of one CO molecule per surface platinum atom. The increase in amount of Sn loadings resulted in a decrease in the number of surface Pt atoms (Table 5.2). This decrease could be due to preferential blocking of surface Pt atoms by Sn or weakening of adsorption sites due to ligand effects. The non-overcoated Pt/γ-Al_2O_3 and 5ALD/Pt/γ-Al_2O_3 had 30 μmol g^{-1} and 10 μmol g^{-1} of surface Pt sites respectively. Overcoating with alumina decreases the extent of CO adsorption on Pt/γ-Al_2O_3 indicating that alumina overcoat is covering a fraction of the exposed Pt atoms.

Table 5.2. Site density and elemental composition of the catalysts studied for alkane dehydrogenation.

Catalyst	Pt (wt%)	Sn (wt%)	Pt:Sn atomic ratio	Sites (μmol g^{-1})
Pt/SiO_2	1.9	-	1:0	100
PtSn/SiO_2	2.4	0.5	3:1	70
PtSn/SiO_2	1.9	1.2	1:1	37
PtSn/SiO_2	1.9	3.4	1:3	25
PtSn/KLZ	0.6	0.7	1:2	8
Pt/γ-Al_2O_3	1.0	-	1:0	30
2ALD/Pt/γ-Al_2O_3	1.0	-	1:0	19
5ALD/Pt/γ-Al_2O_3	1.0	-	1:0	10
10ALD/Pt/γ-Al_2O_3	1.0	-	1:0	3

Ex situ catalyst characterization to determine average particle size and distribution for fresh and spent catalysts (reaction conditions: time on stream equals 2 h, 723 K, 1 atm total pressure, 12.5 Torr isobutane, 50 Torr H_2 pressure, balance He), was performed using STEM to investigate the extent of sintering of nanoparticles. Particle size distribution was obtained by quantifying the catalyst particles in the images taken by STEM. For imaging, a high-angle annular dark-field (HAADF) Z-contrast STEM was used. As seen in Table 5.3, majority of particles for fresh Pt/SiO_2, $PtSn/SiO_2$ and PtSn/KLZ were <1 nm in diameter. There was a slight shift in the particle size distribution post reaction, however, majority of particles were still ~1 nm in size. Thus, the catalysts prepared did not deactivate due to metal particle sintering over a period of 2 h. Having small particles is beneficial as it has been shown in previous studies that large particles undergo deactivation faster than the small ones.[35]

Table 5.3. STEM micrographs and particle size distributions for fresh and spent catalysts.

Catalyst	Fresh Catalyst	Post Reaction	Particle Size Distribution
Pt/SiO_2	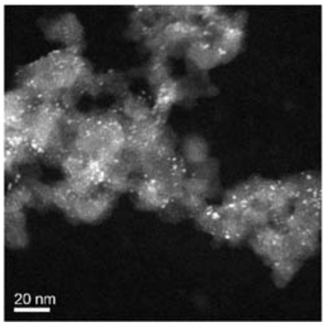	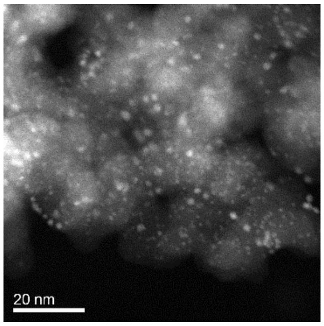	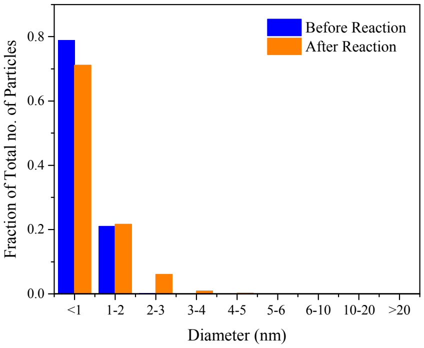
$PtSn/SiO_2$ (Pt:Sn=1:3)	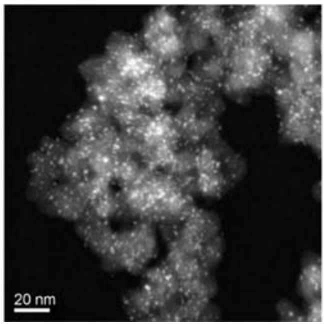	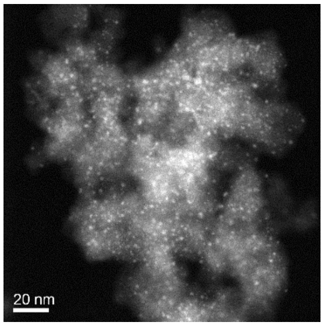	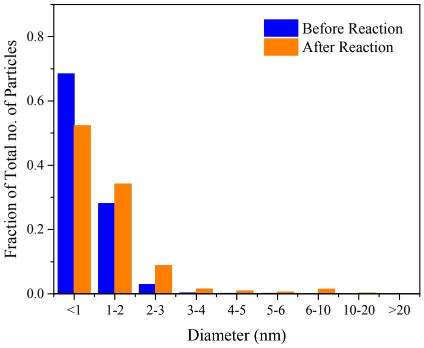
PtSn/KLZ (Pt:Sn=1:2)	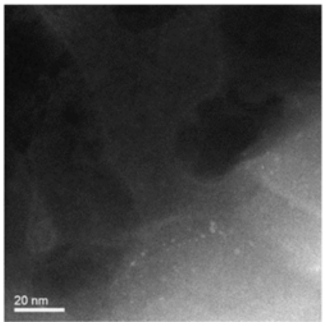	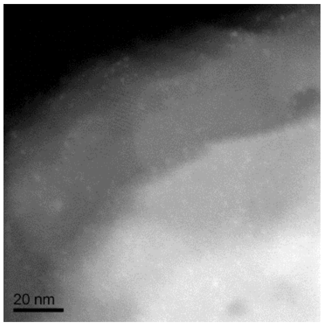	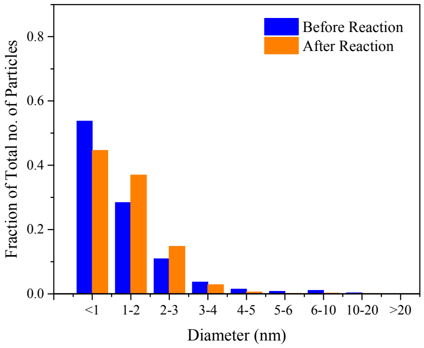

5.3.2. Reaction studies and effect of H_2 co-feeding

Reactivity data for isobutane dehydrogenation over Pt and PtSn catalysts at 723 K for a reaction gas mixture of 12.5 Torr isobutane, 75 Torr H_2, and balance helium is as shown in Table 5.4. The equilibrium conversion for isobutane to isobutene under these reaction conditions is 26%. Hydrogenolysis resulting in the formation of methane, ethane, and propane is higher over the monometallic catalysts as compared to the bimetallic counterparts. On the Pt/γ-Al_2O_3 catalyst, at a higher conversion of 23%, the dehydrogenation selectivity decreased and hydrogenolysis products are observed. Addition of Sn to the 1.88 wt% Pt catalyst significantly decreases the hydrogenolysis rate and increases the selectivity to isobutene to 99%. This result could be due to breaking of Pt ensembles upon addition of Sn and/or the ligand effect.

Table 5.4. Comparison of isobutane dehydrogenation reactivity at 723 K, 12.5 Torr isobutane, 75 Torr H_2 and 760 Torr Total Pressure.

Catalyst	**Pt/SiO_2**	**Pt/γ-Al_2O_3**	**PtSn/SiO_2**	**PtSn/KLZ**
wt% Pt	1.88	1.0	1.88	0.58
Pt:Sn Ratio	-	-	1:3	1:2
WHSV (h^{-1})	118.6	11.9	2.4	7.9
Isobutane Conversion	10.1	23.8	12.4	14.3
CH_4 selectivity	1.3	3.2	0.0	0.7
C_2H_6 selectivity	0.9	1.7	0.0	0.0
C_3H_8 selectivity	2.2	6.7	0.2	0.1
i-C_4H_8 selectivity	91.0	82.6	99.8	99.2

Alkane dehydrogenation in the presence/absence of hydrogen in the feed was studied over a range of 0-200 Torr H_2 pressure under 760 Torr total pressure. It was observed that in the absence of H_2, the monometallic Pt/SiO_2 catalyst exhibits near-zero activity. The origin of this behavior seems to be related to the formation of coke on the catalyst in the absence of H_2. As the H_2 pressure is increased to 25 Torr, we observed a slight increase in the initial dehydrogenation activity. A monotonous increase in the activity is observed as the pressure is further increased to 75 Torr. However, at 200 Torr, there was a decrease in the initial activity towards dehydrogenation (Figure 5.2(a)). Isobutene production TOF vs H_2 pressure (Figure 5.2(b)) at 1.5 h time on stream (TOS) shows that the reaction encounters a maximum.

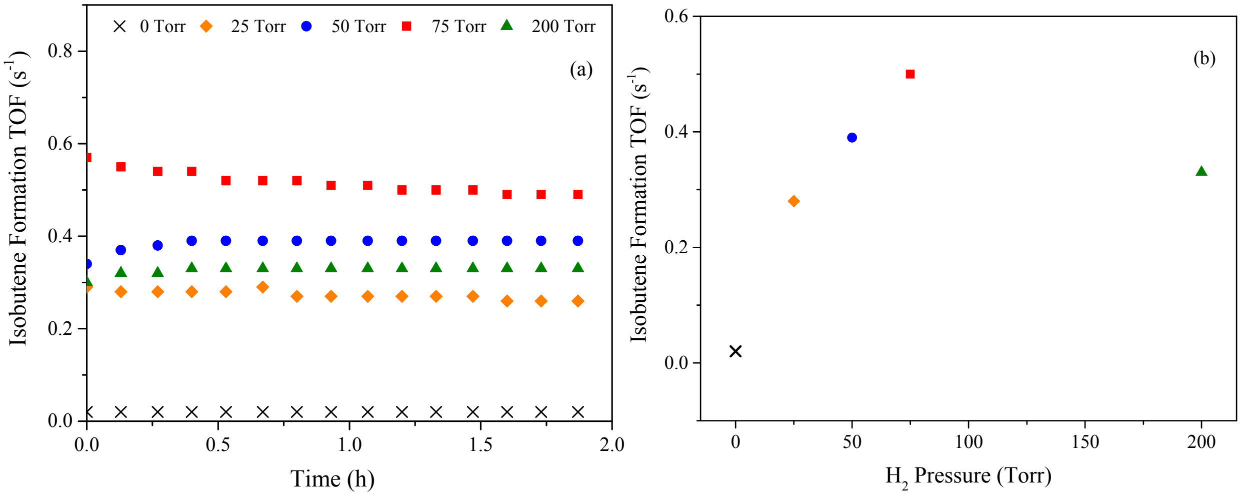

Figure 5.2. Isobutane dehydrogenation over Pt/SiO_2 (a) isobutene TOF vs time on stream (b) isobutene TOF vs H_2 pressure at 1.5 h time on stream. Reaction conditions: T= 723 K, isobutane pressure= 12.5 Torr, 0-200 Torr H_2, balance He, total pressure= 1 atm.

This can be explained as a coupled effect of deactivation and inhibition by H_2. At 200 Torr pressure, the coverage of hydrogen is substantial enough to reduce the certainty of the hydrocarbon interacting with the active site. A similar trend was seen for monometallic Pt on γ-Al_2O_3 with varying hydrogen pressures. Over alumina support, however, there was considerable hydrogenolysis activity as compared to that over Pt/SiO_2.

The product selectivities over Pt/SiO_2 and PtSn/SiO_2 (Pt:Sn = 1:3) at 4 to 6% isobutane conversion are shown in Figure 5.3. The selectivity towards hydrogenolysis products such as methane, propene, etc. increased with increasing hydrogen partial pressure whereas that towards the desired product, isobutene, decreased continuously. Addition of Sn resulted in >99% selectivity towards isobutene at all the various hydrogen partial pressures.

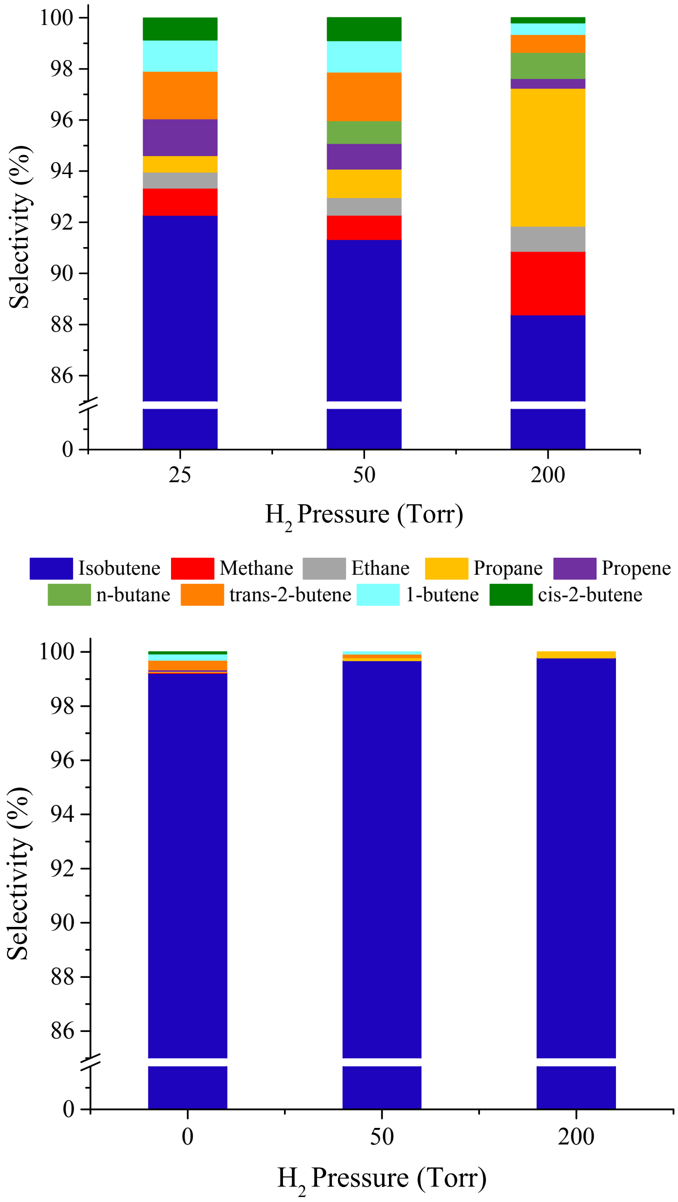

Figure 5.3. Product selectivities over Pt/SiO2 (top) and PtSn/SiO2 (Pt:Sn = 1:3) (bottom). Reaction conditions: T= 723 K, isobutane pressure= 12.5 Torr, 0-200 Torr H_2, balance He, 1 atm total pressure.

Over PtSn catalysts, we observed a significant shift in the initial activity towards isobutene production. On PtSn/SiO2 (Pt:Sn = 1:3), as the H_2 co-feed partial pressure was increased from 0-200 Torr, a monotonic decrease was seen for isobutene TOF (Figure 5.4). A similar trend was seen for PtSn/KLZ (Pt:Sn = 1:2). The negative order with respect to hydrogen pressure for isobutane dehydrogenation over PtSn/SiO2 catalysts (Table 5.5) suggests that addition of Sn to Pt/SiO2 increases the hydrogen coverage on the dehydrogenation sites with increasing hydrogen pressure. Hydrogen competitively adsorbs on the sites required for dissociative adsorption of isobutane. Paffett *et al.* showed that the presence of Sn suppresses both the adsorption and desorption rates of hydrogen on Pt(111) surface.[36] Thus, the Sn additive improves resistance of the supported Pt catalysts to deactivation by coking and without this promotion, in the absence of H_2, the monometallic catalyst deactivates to nearly zero activity within several minutes on stream.

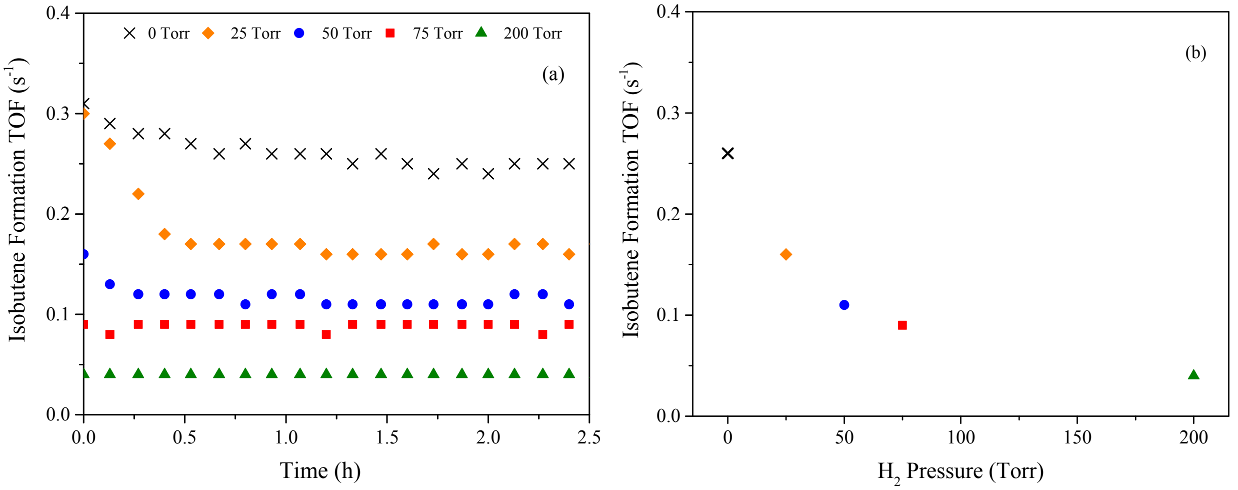

Figure 5.4. Isobutane dehydrogenation over $PtSn/SiO_2$ (Pt:Sn=1:3) (a) isobutene TOF vs time on stream (b) isobutene TOF vs H_2 pressure at 1.5 h time on stream. Reaction conditions: T= 723 K, isobutane pressure= 12.5 Torr, 0-200 Torr H_2, balance He, total pressure= 1 atm.

Comparison between the initial activity of Pt/SiO_2 and $PtSn/SiO_2$ showed a decrease in the activity for the bimetallic system. Xu *et al.* showed that the presence of Sn in the surface layer of Sn/Pt(111) surface alloys decreases the binding energy of molecular isobutane by approximately 10% in comparison to Pt(111).[37] The decrease in binding energy of this molecularly adsorbed species would decrease the sticking coefficient for the dissociative adsorption of isobutane. For the bimetallic system, the increasing presence of H_2 decreases the initial activity. However, the stability of the catalyst is increased as the presence of hydrogen increases the resilience to coke formation by cleaning the Pt surface. On the other hand, the monometallic system shows an increase in initial activity with increasing H_2. This might be because the coke removal capacity of hydrogen overcomes the decrease in activity by competition for the adsorption site. Microcalorimetric investigations by Cortright *et al.* have shown that Sn decreases the number of sites that strongly interact with hydrogen and carbon monoxide.[38] However, these strong adsorption sites are still present on the PtSn catalyst that exhibited high dehydrogenation selectivity. These results suggest that ensemble effects are primarily responsible for the higher dehydrogenation selectivity of catalysts containing Sn. Coking proceeds via formation of highly dehydrogenated species over multiple adsorption sites. Therefore, a catalyst that inhibits the formation of these intermediate species will serve as an optimal one.

Table 5.5. Reaction order with respect to H_2 in the specified partial pressure range.

Catalyst	**Atomic Ratio (Pt:Sn)**	**H_2 Pressure (Torr)**	**Order**
Pt/SiO_2	-	0 - 75	1
$Pt/\gamma\text{-}Al_2O_3$	-	0 - 75	0.9
$PtSn/SiO_2$	1:3	0 - 200	-0.7
PtSn/KLZ	1:2	0 - 200	-0.8

5.3.3. Catalyst regenerability and quantification of coke

Alumina-supported Pt is a well-known industrial catalyst for paraffin dehydrogenation. In addition to the metal sites, the acidic sites on the high surface alumina accelerate hydrogenolysis, isomerization, and enhance coke formation.[39] The ethene TOF over $Pt/\gamma\text{-}Al_2O_3$ catalyst in a continuous flow reactor is as seen in Figure 5.5. The reusability of a catalyst for endothermic cooling was determined in the following manner. After *in situ* reduction of a fresh catalyst at 773 K, the reactor was heated to 873 K in helium and a reaction was carried out at atmospheric pressure with 12.5 Torr ethane, 0 Torr hydrogen and balance helium for 2 h. At these reaction conditions, the equilibrium conversion is 72%. The ethane conversion was maintained at less than 20% of equilibrium value for dehydrogenation. Upon completion of an experiment, the reactor was purged with helium and simultaneously cooled down to ambient temperature. The spent catalyst was then regenerated by calcining in flowing air at 673 K for 1 h. The catalyst bed was again purged with helium, reduced in flowing hydrogen at 773 K and subsequently exposed to the reactant mixture at the aforementioned experimental conditions. As seen in Figure 5.5, the catalyst activity is largely reversed, suggesting that the deactivation is primarily caused by coke deposition. This regeneration-reduction-reaction cycle was carried out for the alumina overcoated catalysts and a similar pattern was observed. Thus, these catalysts are stable and reusable over repeated calcination-reduction cycles. This regenerability will substantially bring down the cost of catalyst associated with the application of endothermic cooling.

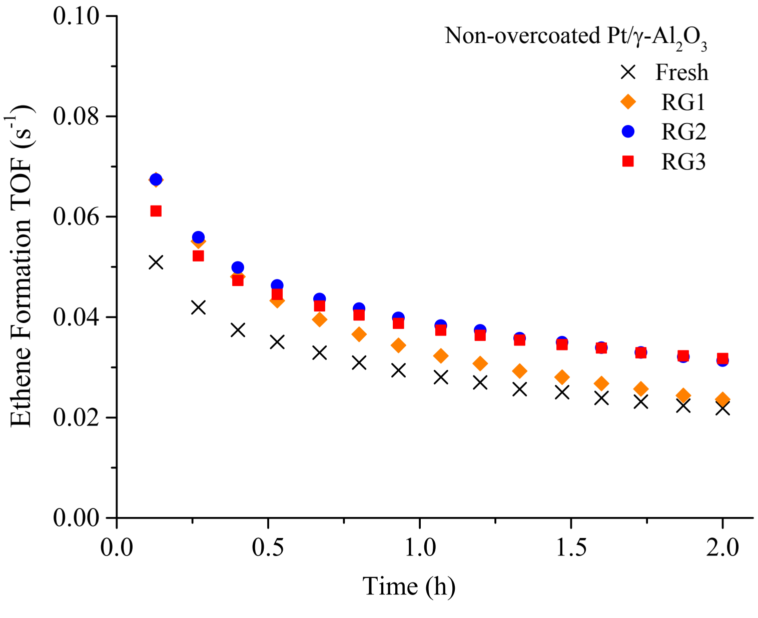

Figure 5.5. Ethane dehydrogenation TOF on non-overcoated Pt/γ-Al_2O_3 (fresh ×; one regeneration [RG1] ◆ ; two regenerations [RG2] ●; three regenerations [RG3] ■). Reaction conditions: 873 K, 12.5 Torr ethane, 0 Torr hydrogen, and balance helium for a total pressure of 1 atm.

The two main paths of catalyst deactivation during gas-phase reactions are sintering and coking. Sintering is an irreversible form whereas carbon deposition can be reversed upon calcination. The interaction of hydrocarbons with metal surfaces usually results in formation of a carbonaceous layer.[40,41] There has been extensive research on the use of modifiers like Sn and Re on oxide supported Pt catalyst as they suppress deposition of coke.[16,42] This is attributed to both geometric and electronic effects. The addition of modifiers prevents the formation of multiple carbon-metal bonds by decreasing the size of surface Pt ensembles and this results is a weakly adsorbed species on the surface.[38,43] To quantify the deactivation of catalyst due to coke formation, a dual bed reactor system was employed. Highly dehydrogenated products are the precursors of coke. Thus, to ensure a flow of equilibrated mixture of isobutane, isobutene and hydrogen through the catalyst under consideration, a pre-bed consisting of a lesser deactivating catalyst e.g., PtSn/KLZ (as seen by the reaction profile) was packed. Thermogravimetric analysis was performed on the spent catalysts. It was assumed that the weight loss during thermogravimetric analysis is solely due the removal of surface coke via CO_2 formation. A ratio of C-atoms deposited per surface Pt atom ($C:Pt_s$) was calculated using the observed change in weight (Table 5.6). It was assumed that the weight loss is solely due the removal of surface coke via CO_2 formation. This $C:Pt_s$ ratio was found to be higher on the Pt/SiO_2 catalyst as compared to the $PtSn/SiO_2$, indicating that coking is more extensive on monometallic than the corresponding bimetallic system. This behavior is attributed to the fact that addition of Sn to Pt/SiO_2 leads to formation of smaller Pt ensembles, thereby decreasing formation of multiple C-M bonds.

Table 5.6. Change in weight observed during thermogravimetric analysis of spent catalysts.

Catalyst	Reaction Time (h)	Sites (µmol g^{-1})	Weight Change (%)	C:Pt_S*
Pt/SiO_2	2	100	2.18	18
Pt/SiO_2	4	100	2.20	*18*
Pt/γ-Al_2O_3	2	30	1.68	47
Pt/γ-Al_2O_3	4	30	1.94	54
γ-Al_2O_3	2	-	0.8	-
Pt-Sn/SiO_2 (1:3)	2	25	0.08	*3*
Pt-Sn/KLZ (1:2)	2	8	0.04	4

Atomic layer deposition of alumina on Pd/Al_2O_3 was shown to greatly reduce catalyst deactivation by coking and sintering for the catalytic oxidative dehydrogenation of ethane.[28] Recently, alumina overcoating has also been shown to stabilize Cu catalyst for liquid phase catalytic reactions by selectively armoring the under-coordinated Cu atoms on the nanoparticle surface by inhibiting leaching of Cu.[29] Thermogravimetric analysis was performed on post reaction catalysts to quantify the amount of coke deposited. Under operating conditions- 873 K and 1 atm, reactions were carried out for 2 h on both the non-overcoated and the alumina-overcoated catalysts in a dual bed reactor system described earlier. The different amounts of coke deposited per gram of catalyst are listed in Table 5.7. For the non-overcoated Pt/γ-Al_2O_3 catalyst, 0.98 mg of coke was formed on 24.55 mg of sample after 2 h of reaction which corresponds to a loss of 3.7 wt%. After 2 h of reaction on 5ALD/Pt/γ-Al_2O_3, a loss of 1.9 wt% was observed. The overcoated catalyst thus gives lesser amount of coke and maintains higher activity at 873 K as compared to the non-overcoated catalyst.

Table 5.7. Thermogravimetric analysis of non-overcoated and ALD overcoated Pt/γ-Al_2O_3 catalysts post reaction.

Catalyst	**Carbon Deposition (mmol C g^{-1})**
Non-overcoated 1 wt. % Pt/γ-Al_2O_3	3.7
2cALD/Pt/γ-Al_2O_3	1.8
5cALD/Pt/γ-Al_2O_3	1.9
10cALD/Pt/γ-Al_2O_3	0.9

5.3.4. Effect of catalyst support

SiO_2 and KLZ supported PtSn catalysts were found to differ in turnover frequencies towards isobutene formation (Table 5.8). It is widely recognized that the support can strongly affect the metal–metal interaction,[44] and if it contains acidity, it can greatly promote the rate of coke formation under isobutane dehydrogenation conditions.[45] SiO_2 is a near-neutral support and K-L-Zeolite, an alkali-doped zeolite, is a nonacidic support. The differential heats of adsorption of H_2 and CO on silica supported and stoichiometrically exchanged L-Zeolite supported Pt are similar.[46] The higher rate over PtSn/KLZ might be due to stabilization of the activated complex for isobutane dissociation on the small particles of PtSn in the zeolitic microstructure[47] and/or by the presence of potassium.

Table 5.8. Support effects on isobutene formation TOF for PtSn system without hydrogen co-feed.

Catalyst	**Time (h)**	**Catalyst Mass (g)**	**Isobutene Selectivity (%)**	**Rate (μmol g^{-1} min^{-1})**	**Isobutene Formation TOF (s^{-1})**
PtSn/SiO_2	1.5	0.05	99	15	0.26
PtSn/KLZ	1.5	0.015	99	66	2.38

5.3.5. Effect of ALD overcoating

DFT calculations for ethane dehydrogenation on the terrace and step of pristine Pt(433) surface revealed that the main product on the terrace is ethene and that the under-coordinated step sites bind C_2H_x and CH_x species more strongly than the sites on terrace. These under-coordinated step sites facilitate deep dehydrogenation, resulting in catalyst deactivation due to coke formation. It was demonstrated that decorating the step sites on Pt(433) surface with AlO_x blocked those sites thereby inhibiting deep dehydrogenation and coke formation. To draw a parallel to the theoretical study of AlO_x on Pt(433) surface, the parent Pt/γ-Al_2O_3 was overcoated with alumina using ALD. Ethene TOF was plotted for reactions on both the catalysts after three regenerations (Figure 5.6). The catalysts deactivated at a higher rate over the first 0.5 h of the reaction following which the deactivation rate decreased. At 2 h times on stream and in the absence of hydrogen, the 5ALD/Pt/γ-Al_2O_3 catalyst exhibited 3 times higher ethene TOF compared to Pt/γ-Al_2O_3. Thus, in hypersonic flights, higher amount of heat will be absorbed per surface Pt atom for the overcoated catalyst.

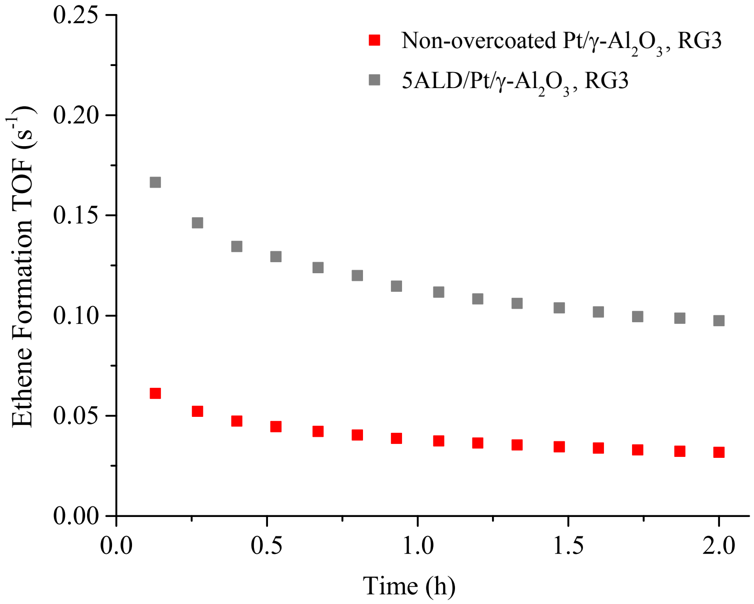

Figure 5.6. Effect of alumina overcoating on ethene production for non-overcoated Pt/γ-Al_2O_3 (■) and 5ALD/ Pt/γ-Al_2O_3 (■) after three regenerations. Reaction conditions: 873 K, 12.5 Torr ethane, 0 Torr hydrogen, and balance He for a total pressure of 1 atm.

Previous studies have shown that co-feeding hydrogen can inhibit the amount of deactivation via coke formation, probably by hydrogenation of highly dehydrogenated coke precursors.[26,48] DFT calculations on Pt(433) terrace and AlO_x decorated Pt(433) step surfaces show that when H* is present in vicinity, hydrogenation of coke precursors is kinetically favorable and ethene is the main gas phase product. Analogous to this result, increasing the hydrogen to ethane ratio from 0 to 4 in the feed caused a significant increase in the ethene production rates as observed from Figure 5.6 and Figure 5.7. A comparison of ethene TOF shows that $5ALD/Pt/\gamma\text{-}Al_2O_3$ has 2.5 times higher steady state activity than the non-overcoated $Pt/\gamma\text{-}Al_2O_3$ at 2 h time on stream in the presence of hydrogen. These findings were corroborated by our reaction kinetic experiments where a four times enhancement of ethylene turnover frequency was observed on 10 cycled atomic layer deposited alumina overcoated $Pt/\gamma\text{-}Al_2O_3$ catalyst compared to $Pt/\gamma\text{-}Al_2O_3$ without alumina decoration.

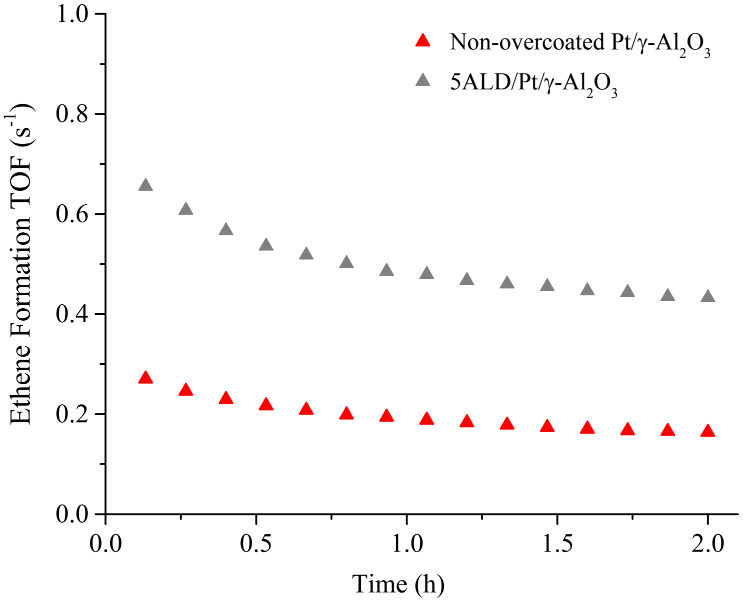

Figure 5.7. Effect of alumina overcoating on ethene production for non-overcoated $Pt/\gamma\text{-}Al_2O_3$ (▲) and $5ALD/Pt/\gamma\text{-}Al_2O_3$ (▲). Reaction conditions: 873 K, 12.5 Torr ethane, 50 Torr hydrogen, and balance He for a total pressure of 1 atm.

5.4. Conclusion

In this chapter, we showed that both addition of Sn and ALD overcoating on Pt catalysts under study for alkane dehydrogenation results in lesser amount of coke being formed on the catalyst surface as compared to that on the monometallic Pt catalyst. The dehydrogenation activity was lower over the bimetallic catalyst but the hydrogenolysis activity was repressed thereby resulting in higher selectivity towards the desired alkene. This is attributed to geometric and/or ligand effect brought about by the Sn addition. In the absence of hydrogen in the feed, monometallic Pt showed near zero activity whereas co-feeding hydrogen to a certain partial pressure resulted in improving the dehydrogenation activity. The coke deposited on the catalyst was removed by calcination and the activity was largely restored upon subsequent reduction. Both the non-overcoated and the overcoated catalysts prepared in this study were stable to the regeneration-reduction-reaction cycle. The alumina overcoated catalyst, 5ALD/Pt/γ-Al_2O_3, showed higher initial as well as steady state activity as compared to the non-overcoated catalyst. This is in agreement with the DFT results on AlO_x decoration of the Pt(433) step surface. The ethene turnover frequencies increased when the hydrogen to ethane ratio was changed from 0 to 4 in the feed. This effect of co-feeding hydrogen was accounted by the theoretical calculations of hydrogenation of strongly bound intermediates in the presence of nearby adsorbed hydrogen. Thermogravimetric analysis showed a higher amount of coke accumulation on the non-overcoated catalyst. Our results from theory and experiments come together to predict the behavior of alumina overcoated catalysts for ethane dehydrogenation and show a promising lead for their use in endothermic cooling application for hypersonic flights.

5.5. Acknowledgements

This work was supported by the Air Force Office of Scientific Research and was performed by a team comprising of Dr. Guowen Peng, Dr. Sungsik Lee, Duygu Gerceker under the guidance of Prof. J. A. Dumesic, Prof. M. Mavrikakis, and Dr. Randal Winans as principal investigators.

5.6. References

1. Sicard, M.; Grill, M.; Raepsaet, B.; Ser, F.; Potvin, C.; Djéga-Mariadassou, G., n-dodecane thermal and catalytic cracking under supercritical conditions. In Studies in Surface Science and Catalysis, Antoine Gédéon, P. M.; Florence, B., Eds. Elsevier: 2008; Vol. Volume 174, Part B, pp 1103-1106.
2. Edwards, T., Liquid fuels and propellants for aerospace propulsion: 1903-2003. J. Propul. Power 2003, 19 (6), 1089-1107.
3. Edwards, T., Cracking and deposition behavior of supercritical hydrocarbon aviation fuels. Combust. Sci. Technol. 2006, 178 (1-3), 307-334.
4. Yeh, Y. H.; Yu, J. Y.; Luo, J.; Gorte, R. J., Endothermic Reforming of n-Hexane on Metal (Pt, Ga) Containing H-ZSM-5 at High Pressures. Ind. Eng. Chem. Res. 2015, 54 (43), 10675-10683.
5. Qu, S. D.; Liu, G. Z.; Meng, F. X.; Wang, L.; Zhang, X. W., Catalytic Cracking of Supercritical n-Dodecane over Wall-Coated HZSM-5 with Different Si/Al Ratios. Energy Fuels 2011, 25 (7), 2808-2814.
6. Jiang, R. P.; Liu, G. Z.; You, Z. Q.; Luo, M. J.; Wang, X. Q.; Wang, L.; Zhang, X. W., On the Critical Points of Thermally Cracked Hydrocarbon Fuels under High Pressure. Ind. Eng. Chem. Res. 2011, 50 (15), 9456-9465.
7. Bao, S. G.; Liu, G. Z.; Wang, L.; Zhang, X. W.; Mi, Z. T., Preparation and properties of hydrocarbon dispersible HZSM-5 nanocrystals for quasi-homogeneous catalytic cracking of n-dodecane. Microporous Mesoporous Mat. 2011, 143 (2-3), 458-466.
8. Sinfelt, J. H.; Taylor, W. F.; Yates, D. J. C., Catalysis over supported metals .3. Comparison of metals of known surface area for ethane hydrogenolysis. J. Phys. Chem. 1965, 69 (1), 95.
9. Cremer, P. S.; Su, X. C.; Shen, Y. R.; Somorjai, G. A., Ethylene hydrogenation on Pt(111) monitored in situ at high pressures using sum frequency generation. J. Am. Chem. Soc. 1996, 118 (12), 2942-2949.
10. Kesmodel, L. L.; Dubois, L. H.; Somorjai, G. A., LEED analysis of acetylene and ethylene chemisorption on the Pt(111) surface- Evidence for ethylidyne formation. Journal of Chemical Physics 1979, 70 (5), 2180-2188.
11. Cortright, R. D.; Watwe, R. M.; Dumesic, J. A., Ethane hydrogenolysis over platinum - Selection and estimation of kinetic parameters. J. Mol. Catal. A-Chem. 2000, 163 (1-2), 91-103.
12. Watwe, R. M.; Cortright, R. D.; Mavrikakis, M.; Norskov, J. K.; Dumesic, J. A., Density functional theory studies of the adsorption of ethylene and oxygen on Pt(111) and Pt(3)Sn(111). Journal of Chemical Physics 2001, 114 (10), 4663-4668.
13. Anghel, A. T.; Jenkins, S. J.; Wales, D. J.; King, D. A., Theory of C2Hx species on Pt{110}(1 x 2): Structure, stability, and thermal chemistry. J. Phys. Chem. B 2006, 110 (9), 4147-4156.

14. Chen, Y.; Vlachos, D. G., Hydrogenation of Ethylene and Dehydrogenation and Hydrogenolysis of Ethane on Pt(111) and Pt(211): A Density Functional Theory Study. J. Phys. Chem. C 2010, 114 (11), 4973-4982.
15. Siddiqi, G.; Sun, P. P.; Galvita, V.; Bell, A. T., Catalyst performance of novel Pt/Mg(Ga)(Al)O catalysts for alkane dehydrogenation. Journal of Catalysis 2010, 274 (2), 200-206.
16. Galvita, V.; Siddiqi, G.; Sun, P. P.; Bell, A. T., Ethane dehydrogenation on Pt/Mg(Al)O and PtSn/Mg(Al)O catalysts. J. Catal. 2010, 271 (2), 209-219.
17. Sun, P.; Siddiqi, G.; Vining, W. C.; Chi, M.; Bell, A. T., Novel Pt/Mg(In)(Al)O catalysts for ethane and propane dehydrogenation. J. Catal. 2011, 282 (1), 165-174.
18. Jablonski, E. L.; Castro, A. A.; Scelza, O. A.; de Miguel, S. R., Effect of Ga addition to Pt/Al2O3 on the activity, selectivity and deactivation in the propane dehydrogenation. Applied Catalysis A: General 1999, 183 (1), 189-198.
19. Barias, O. A.; Holmen, A.; Blekkan, E. A., Propane dehydrogenation over supported Pt and Pt-Sn catalysts: Catalyst preparation, characterization, and activity measurements. J. Catal. 1996, 158 (1), 1-12.
20. Cortright, R. D.; Bergene, E.; Levin, P.; NatalSantiago, M.; Dumesic, J. A., Reactions of isobutane and isobutylene over silica- and L-zeolite-supported Pt/Sn and Pt/Sn/K catalysts. Elsevier Science Publ B V: Amsterdam, 1996; Vol. 101, p 1185-1194.
21. Stagg, S. M.; Querini, C. A.; Alvarez, W. E.; Resasco, D. E., Isobutane dehydrogenation on Pt-Sn/SiO2 catalysts: Effect of preparation variables and regeneration treatments. Journal of Catalysis 1997, 168 (1), 75-94.
22. Cortright, R. D.; Watwe, R. M.; Spiewak, B. E.; Dumesic, J. A., Kinetics of ethane hydrogenolysis over supported platinum catalysts. Catal. Today 1999, 53 (3), 395-406.
23. Watwe, R. M.; Cortright, R. D.; Norskov, J. K.; Dumesic, J. A., Theoretical studies of stability and reactivity of C-2 hydrocarbon species on Pt clusters, Pt(111), and Pt(211). J. Phys. Chem. B 2000, 104 (10), 2299-2310.
24. Kumar, M. S.; Chen, D.; Walmsley, J. C.; Holmen, A., Dehydrogenation of propane over Pt-SBA-15: Effect of Pt particle size. Catal. Commun. 2008, 9 (5), 747-750.
25. Shen, J. Y.; Hill, J. M.; Watwe, R. M.; Spiewak, B. E.; Dumesic, J. A., Microcalorimetric, infrared spectroscopic, and DFT studies of ethylene adsorption on Pt/SiO(2) and Pt-Sn/SiO(2) catalysts. J. Phys. Chem. B 1999, 103 (19), 3923-3934.
26. Wu, J.; Peng, Z. M.; Sun, P. P.; Bell, A. T., n-Butane dehydrogenation over Pt/Mg(In)(Al)O. Appl. Catal. A-Gen. 2014, 470, 208-214.
27. Hauser, A. W.; Gomes, J.; Bajdich, M.; Head-Gordon, M.; Bell, A. T., Subnanometer-sized Pt/Sn alloy cluster catalysts for the dehydrogenation of linear alkanes. PCCP Phys. Chem. Chem. Phys. 2013, 15 (47), 20727-20734.
28. Lu, J.; Fu, B.; Kung, M. C.; Xiao, G.; Elam, J. W.; Kung, H. H.; Stair, P. C., Coking- and Sintering-Resistant Palladium Catalysts Achieved Through Atomic Layer Deposition. Science 2012, 335 (6073), 1205-1208.
29. O'Neill, B. J.; Jackson, D. H. K.; Crisci, A. J.; Farberow, C. A.; Shi, F. Y.; Alba-Rubio, A. C.; Lu, J. L.; Dietrich, P. J.; Gu, X. K.; Marshall, C. L.; Stair, P. C.; Elam, J. W.; Miller, J. T.; Ribeiro, F. H.; Voyles, P. M.; Greeley, J.; Mavrikakis, M.; Scott, S. L.; Kuech, T. F.; Dumesic, J. A., Stabilization of Copper Catalysts for Liquid-Phase Reactions by Atomic Layer Deposition. Angew. Chem.-Int. Edit. 2013, 52 (51), 13808-13812.

30. Benesi, H. A.; Curtis, R. M.; Studer, H. P., Preparation of highly dispersed catalytic metals - Platinum supported on silica gel. J. Catal. 1968, 10 (4), 328.
31. Lee, S.; Kumbhalkar, M. D.; Wiaderek, K. M.; Dumesic, J.; Winans, R. E., Effect of Particle Size upon Pt/SiO2 Catalytic Cracking of n-Dodecane under Supercritical Conditions: In situ SAXS and XANES Studies. ChemCatChem 2017, 9 (1), 99-102.
32. Cortright, R. D.; Dumesic, J. A., L-zeolite-supported platinum and platinum/tin catalysts for isobutane dehydrogenation. Appl. Catal. A-Gen. 1995, 129 (1), 101-115.
33. Puurunen, R. L., Surface chemistry of atomic layer deposition: A case study for the trimethylaluminum/water process. J. Appl. Phys. 2005, 97 (12).
34. Wiedmann, M. K.; Jackson, D. H. K.; Pagan-Torres, Y. J.; Cho, E.; Dumesic, J. A.; Kuech, T. F., Atomic layer deposition of titanium phosphate on silica nanoparticles. J. Vac. Sci. Technol. A 2012, 30 (1).
35. Vanbroekhoven, E. H.; Schoonhoven, J.; Ponec, V., The influence of the metal-particle size on the formation of multiple metal-carbon bonds. Surface Science 1985, 156, 899-910.
36. Paffett, M. T.; Gebhard, S. C.; Windham, R. G.; Koel, B. E., Chemisorption of ethylene on ordered Sn/Pt(111) surface alloys. Surface Science 1989, 223 (3), 449-464.
37. Xu, C.; Koel, B. E.; Paffett, M. T., Adsorption and desorption behavior of n-butane and isobutane on Pt(111) and Sn/Pt(111) surface alloys. Langmuir 1994, 10 (1), 166-171.
38. Cortright, R. D.; Dumesic, J. A., Microcalorimetric, spectroscopic, and kinetic studies of silica-supported Pt and Pt/Sn catalysts for isobutane dehydrogenation. J. Catal. 1994, 148 (2), 771-778.
39. Bhasin, M. M.; McCain, J. H.; Vora, B. V.; Imai, T.; Pujado, P. R., Dehydrogenation and oxydehydrogenation of paraffins to olefins. Appl. Catal. A-Gen. 2001, 221 (1-2), 397-419.
40. Barbier, J., Deactivation of reforming catalysts by coking- A Review. Applied Catalysis 1986, 23 (2), 225-243.
41. Guisnet, M.; Magnoux, P., Organic chemistry of coke formation. Appl. Catal. A-Gen. 2001, 212 (1-2), 83-96.
42. Cortright, R. D.; Hill, J. M.; Dumesic, J. A., Selective dehydrogenation of isobutane over supported Pt/Sn catalysts. Catal. Today 2000, 55 (3), 213-223.
43. Biloen, P.; Helle, J. N.; Verbeek, H.; Dautzenberg, F. M.; Sachtler, W. M. H., The role of rhenium and sulfur in platinum-based hydrocarbon converion catalysts. J. Catal. 1980, 63 (1), 112-118.
44. Nunez, G. M.; Rouco, A. J., Support effects on metal-metal interaction in Rh-Au bimetallic catalysts. J. Catal. 1988, 111 (1), 41-49.
45. Resasco, D. E.; Marcus, B. K.; Huang, C. S.; Durante, V. A., Isobutane dehydrogenation over sulfided nickel catalysts. J. Catal. 1994, 146 (1), 40-55.
46. Sharma, S. B.; Miller, M. T.; Dumesic, J. A., Microcalorimetric study of silica-supported and zeolite-supported platinum catalysts. J. Catal. 1994, 148 (1), 198-204.
47. Derouane, E. G.; Vanderveken, D. J., Strutural recognition and preorganization in zeolite catalysts- Direct aromatization of normal-Hexane on zeolite L-based catalysts. Applied Catalysis 1988, 45 (1), L15-L22.
48. Virnovskaia, A.; Rytter, E.; Olsbye, U., Kinetic and isotopic study of ethane dehydrogenation over a semicommercial Pt,Sn/Mg(Al)O catalyst. Ind. Eng. Chem. Res. 2008, 47 (19), 7167-7177.

CHAPTER 6

XAS Characterization of supported bimetallic catalysts

6.1. Introduction

Since its development in the early 1970s, synchrotron-based X-ray absorption spectroscopy (XAS) has proven to be a versatile structural probe for investigating element specific electronic and structural properties for supported metal catalysts. XAS refers to the details of how x-rays are absorbed by an atom at energies near and above the core-level binding energies of that atom.[1] The spectra are sensitive to the oxidation state, the coordination geometry, nature of the atoms surrounding the selected element, and the coordination number with the surrounding atoms. XAS probes the bulk physical environment and is used in a variety of scientific fields. Both physical and electronic structure are probed, but the probe range is generally only the first two shells of atoms around the absorber atom, which is generally less than 5 to 6 Å. In some special cases (e.g., when the sample is highly crystalline), information about more distant shells can be obtained, usually with greater uncertainty than in the near-shell cases. Measurements can also be made on elements with low loading or even trace abundance, thereby probing the chemical and physical state of dilute species.

XAS is performed at synchrotrons as it requires an intense and energy-tunable source of x-rays. The x-ray absorption spectrum is typically divided into 2 regions (Figure 6.1): x-ray absorption near-edge spectroscopy (XANES) and extended x-ray absorption fine-structure spectroscopy (EXAFS). A XANES or NEXAFS (near-edge x-ray absorption fine structure) spectrum contains information on bound-state electronic transitions and multiple-scattering resonances associated with a given absorption edge. The former gives information similar to optical electronic spectra: valence, coordination chemistry (e.g., octahedral, tetrahedral coordination), relative site distortion, and so on. The latter is sensitive to the details of the atomic geometry of the first few neighbor atom shells, i.e., the multiple-scattering resonances in the

XANES region often serve as a "fingerprint" of a particular structural arrangement of atoms in the vicinity of the absorber. An EXAFS spectrum is produced by electron scattering in the vicinity of the absorber, and thus holds information similar to that recovered from an x-ray scattering experiment, although the scattering is much more local for electrons. Bond distances involving the absorber can be determined for the first two shells with a precision of 0.01 Å or so, and an accuracy of 0.02 to 0.04 Å.[2] Coordination numbers in the best case are accurate to 5%, and in general to 10-20%. Thermal and static disorders are also convoluted into the EXAFS signal. These are usually more of a problem than a source of information but can be used, in favorable cases, to determine vibrational amplitudes and details of site populations. X-ray absorption spectra can be collected in both transmission and fluorescence mode depending on the concentration of the metal under investigation. For concentrated samples, XAS measurements are performed in the transmission mode whereas for lower concentration, fluorescence is the preferred technique.

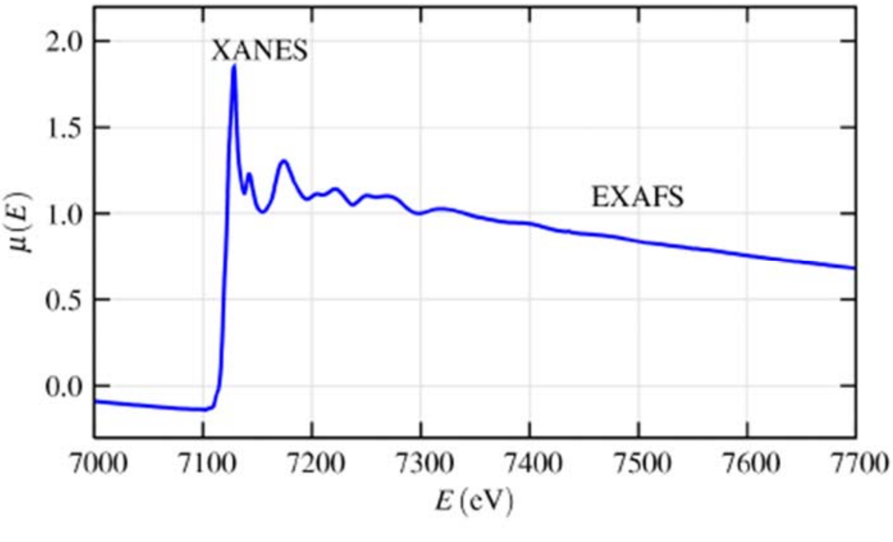

Figure 6.1. XANES and EXAFS regions of the Fe K-edge x-ray absorption spectrum (absorption as a function of energy) (Adapted from Newville[1]).

X-ray absorption measurements can provide essential information about the structure of bimetallic nanoparticles, and these can help us elucidate the nature of the active site in a catalyst when coupled with reactivity studies and other characterization techniques such as scanning transmission electron microscopy, energy dispersive x-ray spectroscopy and so on. As XAS is a bulk technique, the catalysts under study must be monodispersed. Several techniques such as electroless deposition,[3] strong electrostatic adsorption,[4] atomic layer deposition,[5] and controlled surface reactions[6] are used to synthesize catalysts with narrow particle size and composition distributions. For nanoparticles with diameters smaller than 3 to 5 nm, the coordination number is a strong and nonlinear function of the particle diameter. Several correlations have been established in the literature for the relating the average coordination of an atom with its particle size.[7-9] To this end, we have employed XAS to determine the local atomic environment, oxidation state, and particle size of catalysts for the following systems: carbon and silica-supported PtMo catalysts for water gas shift reaction, silica-supported AuMo catalysts for reverse water gas shift reaction, and carbon-supported RhRe catalysts for C-O hydrogenolysis of tetrahydropyran-2-methanol.

6.2. XAS Measurements and Analysis

The XAS measurements for all the catalysts were performed at the Advanced Photon Source at Argonne National Laboratory. For the PtMo catalysts studied for water gas-shift reaction, Pt L_{III}-edge (11.564 keV) and Mo K-edge (20.000 keV) x-ray absorption measurements were conducted on the bending magnet beamline of the Materials Research Collaborative Access Team (MRCAT, 10-BM). For AuMo catalysts, Au L_{III}-edge (11.919 keV) and Mo K-edge (20.000 keV) XAS measurements were performed on the beamlines: 10-BM and 12-BM. The XAS measurements were performed in fluorescence mode using a capillary cell as shown in Figure 6.2. For RhRe/C samples, XAS measurements were performed at beamline 20 (20-BM-B). The Rh K-edge (23.220 keV) and Re L_{III}-edge (10.350 keV) were probed to obtain the extended x-ray absorption fine structure and x-ray absorption near-edge structure. The detailed experimental setup in described later in the respective sections.

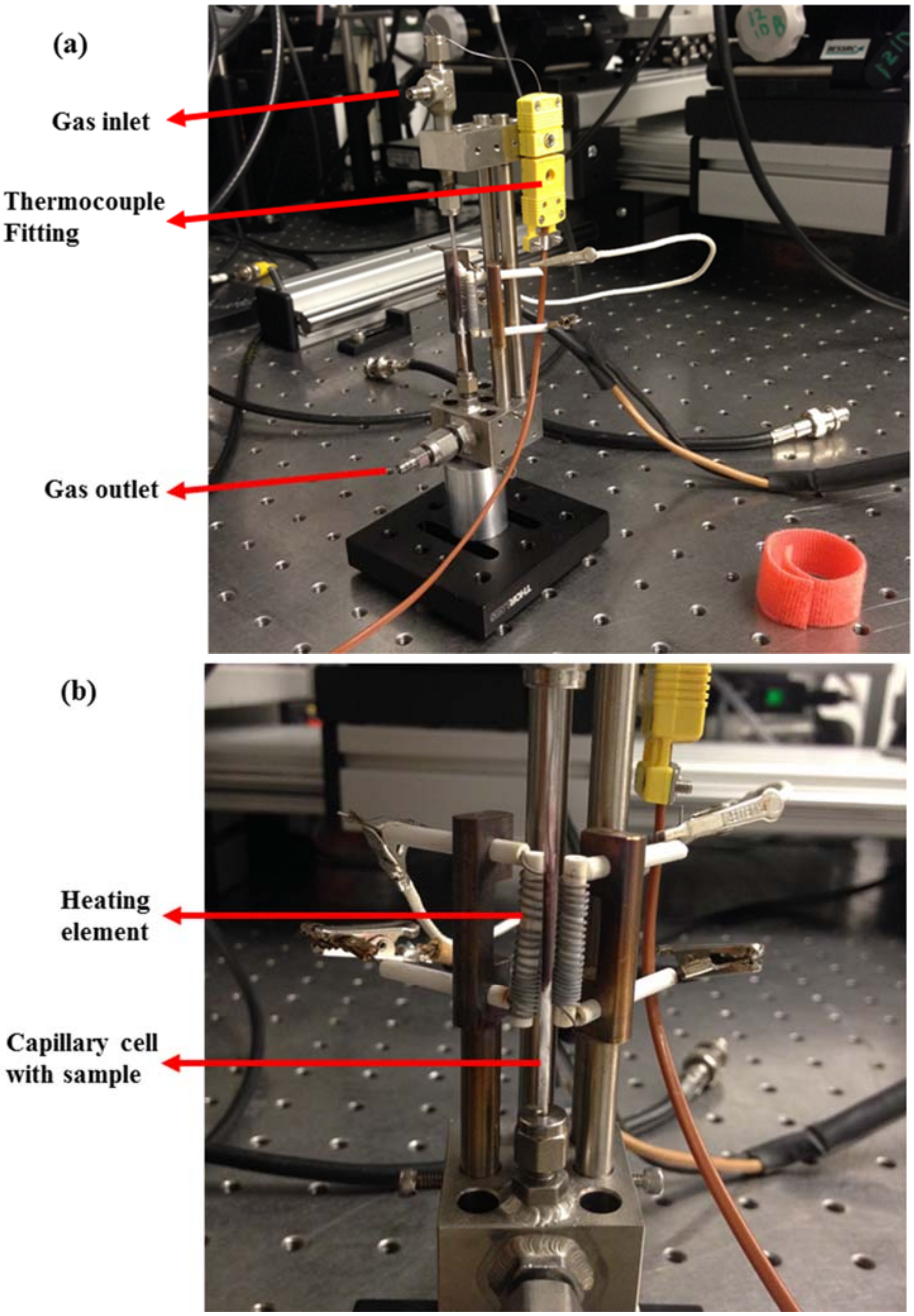

Figure 6.2. (a) *In situ* XAS capillary reactor setup and (b) the zoomed in view of the capillary cell with the heating filament located at the 12-BM beamline at the Advanced Photon Source at Argonne National Laboratory.

The initial XANES and EXAFS analysis was performed using the Athena software.[10] Thereafter, the theoretical phase and amplitude functions for various absorber-backscatterer pairs were calculated with FEFF6 using a two-atom calculation. The phase and amplitude files for elements in the reduced state at room temperature were obtained using the respective foils. The values for S_o^2 and $\Delta\sigma^2$ were determined by fitting the foils with FEFF. Standard procedures using WinXAS 3.2 software were employed to fit the XAS data.[11,12] The EXAFS parameters were obtained by a least square fit in the R-space of the k^2-weighted Fourier transform (FT) data for all catalysts. For the bimetallic scattering, the values of R and $\Delta\sigma^2$ were constrained to be equal for both edges, and R was further constrained to be equal to the average of the monometallic scattering of each component.

6.3. Results and Discussion

6.3.1. Supported PtMo catalysts for Water-Gas Shift Reaction

The water-gas shift (WGS) reaction has been widely used for the production of hydrogen from synthesis gas. As WGS is equilibrium-limited at high temperatures, the reaction is commercially carried out in two steps: a high temperature step that exploits high catalytic activity over an iron-based catalyst at 623 to 673 K, followed by a low temperature step for high CO conversion over a copper-based catalyst at 463 to 503 K.[13] These Cu-based catalysts, though inexpensive, are pyrophoric, deactivate due to leaching, and are poisoned by impurities in the syngas feed. However, noble metals, platinum in particular, and their alloys have attracted attention due to their stability and high activity for low temperature WGS.[14-16] The reactivity of Pt for WGS can be enhanced by introducing a metal oxide promoter, such as molybdenum and rhenium. Since the dissociative adsorption of water on Pt(111) is endothermic by 0.33 eV, the role of the promoter is to stabilize adsorbed water and hydroxyl groups, thereby increasing their respective coverages substantially.[17] Recently, Ribeiro *et al.* studied the WGS activity of Pt on Mo_2C and suggested that the active sites are formed by the Pt-Mo alloy nanoparticles in contact with Mo_2C.[18] The higher activity over Pt/Mo_2C is suggested to be due to water activation on Mo_2C.

Therefore, a close interaction between Pt and the promoter metal is required to realize the full potential of these bimetallic catalysts.

Coimpregnation and successive impregnation methods have been applied to prepare bimetallic catalysts. A monometallic catalyst is firstly prepared and is subsequently modified by incorporation of the second metal/promoter. This approach does not necessarily allow for control over the particle size and composition of the bimetallic catalysts, often rendering a bimodal distribution of metals on the support. Previously, we have observed that catalysts prepared using controlled surface reactions (CSR) have narrow particle size and composition distributions.[19] This homogeneity makes it possible to draw conclusions about the catalyst structure and composition using bulk techniques such as XAS and EDS. To this end, we have prepared PtMo catalysts using controlled surface reactions approach to study their activity towards WGS and have characterized them using CO chemisorption, inductively coupled plasma-atomic emission spectroscopy (ICP-AES), scanning transmission electron microscopy/energy-dispersive X-ray spectroscopy (STEM/EDS), and XAS. We have thereby established the structure-activity relationships for these catalysts and addressed the nature of the active sites.

6.3.1.1. Catalyst Preparation and Characterization

Vulcan XC72 (Cabot) and Davisil Grade 646 (Sigma-Aldrich) were used as carbon and silica supports for the catalysts, respectively. Cycloheptatriene molybdenum tricarbonyl ($(C_7H_8)Mo(CO)_3$, Strem Chemicals, 99%) and anhydrous n-pentane (Sigma-Aldrich) were used without further purification. The $(C_7H_8)Mo(CO)_3$ compound and n-pentane were stored and handled inside a glove box filled with ultra-high purity argon (Airgas). Tetraammineplatinum(II) nitrate ($Pt(NH_3)_4(NO_3)_2$, Sigma-Aldrich, 99.995%) and hydrochloroplatinic acid hydrate ($H_2PtCl_6.xH_2O$, Sigma-Aldrich, 99.995%) were used as Pt precursors. Ammonium hydroxide solution (ACS reagent, 28.0-30.0% NH_3, Sigma Aldrich) was used during the ion exchange of Pt onto silica.

Pt-based monometallic catalysts were prepared by incipient wetness impregnation of H_2PtCl_6 on carbon and silica supports. The H_2PtCl_6 required to achieve a particular metal loading was weighed and dissolved in sufficient Milli-Q water to reach the wetness point of the support, which was found to be 1.7 mL (g carbon)$^{-1}$ and 1.2 mL (g silica)$^{-1}$. The dissolved precursor solution was then added to the support, and the impregnated support was dried at 383 K. The Pt/C and Pt/SiO_2 catalysts were reduced at either 533 K or 723 K under flowing H_2 for 4 hours (1 K min^{-1} ramp rate) and were then passivated with a mixture of 1% O_2 in Ar at room temperature for 1 h.

PtMo bimetallic catalysts were prepared by controlled surface reaction techniques. Briefly, the passivated parent catalyst (Pt/C or Pt/SiO_2) was reduced at 533 K (Pt/C and Pt/SiO_2) or 723 K (Pt/SiO_2) in a Schlenk tube prior to the CSR procedure. The reduced parent catalyst was cooled to room temperature and sealed. The required amount of molybdenum precursor, cycloheptatriene molybdenum tricarbonyl, was weighed and dissolved in n-pentane under an inert atmosphere (ultra-high purity Argon) using a glove box. The sealed Schlenk tube was placed in the glove box and the precursor solution was added to the reduced parent catalyst. The resulting slurry was stirred for 1 h. Molybdenum uptake by the parent catalyst caused a concomitant change in color of the precursor solution. The initially orange slurry became colorless as molybdenum was deposited from the precursor solution onto the parent catalyst. Any solvent remaining after molybdenum uptake was evaporated in a Schlenk line. The dried catalyst was then reduced at 773 K under flowing hydrogen for 45 minutes and passivated with a mixture of 1% O_2 in Ar at room temperature for 0.5 h.

Table 6.1. Characterization results of supported PtMo catalysts prepared by CSR.

Catalyst	**Atomic Mo:Pt (Theo.)**	**Atomic Mo:Pt (ICP)**	**Pt wt% (ICP)**	**Mo wt% (ICP)**	**CO uptake (µmol g^{-1})**	**Disp. (%)**
Pt/C	0	-	5.7	0	147	50
CSR-PtMo/C-1b	0.15	0.17	4.4	0.4	84	37
CSR-PtMo/C-2b	0.30	0.33	4.2	0.7	76	35
CSR-PtMo/C-3b	0.45	0.48	4.4	1.0	52	23
CSR-PtMo/C-4b	0.60	0.54	4.6	1.2	58	24
CSR-PtMo/C-5b	0.75	0.62	4.5	1.2	63	27
Pt/SiO_2	0	-	5.6	0	74	26
CSR-PtMo/SiO_2- 1c	0.15	0.14	5.0	0.3	56	22
CSR-PtMo/SiO_2- 2c	0.30	0.21	4.7	0.5	35	15

To prepare catalysts with higher molybdenum content, the procedure described above was repeated multiple times (*i.e.,* a multicycle synthesis). Catalysts were reduced at 673 K between each cycle and the final reduction was performed at 773 K. With each successive cycle, the total theoretical Mo:Pt atomic ratio was increased by 0.15. Using this procedure, we prepared PtMo catalysts supported on carbon and silica as listed in Table 6.1. The dispersion was based on the CO uptake at 308 K. The CO uptake of the Pt/C parent was 147 µmol/g. After incorporation of molybdenum by CSR with a Mo:Pt ratio of 0.15, the CO uptake decreased to 84 µmol/g (8% decrease with respect to the CSR control), suggesting that Pt sites were partially covered by Mo species. Addition of more Mo to produce Mo:Pt = 0.30 by two cycles and Mo:Pt = 0.45 with three cycles showed decreases of 16% and 43% in CO uptake, respectively. No change in the CO uptake was observed after the fourth and fifth Mo addition cycles.

Table 6.2. Average particle size and composition of PtMo catalysts prepared by CSR using STEM and EDS analyses.

Catalyst ID	**Atomic Mo:Pt (EDS)**	**Average particle size (STEM) (nm)**
CSR-PtMo/C-1b	0.11	1.26 ± 0.55
CSR-PtMo/C-2b	0.21	1.31 ± 0.58
CSR-PtMo/C-3b	0.34	1.38 ± 0.62
CSR-PtMo/C-4b	0.30	1.94 ± 1.08
CSR-PtMo/C-5b	0.32	1.27 ± 0.56
CSR-PtMo/SiO_2- 2c	0.14	3.39 ± 1.92

The average bimetallic particle size and composition obtained by STEM and EDS analysis respectively are as shown in Table 6.2. The nanoparticles in the carbon-supported catalysts were largely unchanged after each successive Mo addition cycle. The actual metal loadings were determined using ICP-AES after digesting the metals in aqua regia. Single nanoparticles were analyzed by EDS, and the results of these EDS measurements were in agreement with the ICP and theoretical values at lower Mo contents. The Mo atomic percentage obtained by EDS was slightly lower than the values obtained by ICP, indicating some deposition of Mo on the support instead of on the Pt nanoparticles. For 1-, 2- and 3-cycle catalysts, 62-71% of Mo is on Pt according to comparative EDS (number averaged values of 30-50 individual nanoparticles) and ICP (bulk catalyst) results. After the 4th cycle, the deposition of Mo onto Pt nanoparticles decreased to 56% and it decreased further to 52% for the 5-cycle catalyst. Moreover, the EDS Mo:Pt ratios of the 3, 4, and 5 cycle catalysts remain nearly constant at about Mo:Pt = 0.32, indicating that Pt nanoparticles become saturated with Mo at this ratio. This saturation occurred at a bulk (*i.e.,* ICP) Mo:Pt ratio of 0.47.

6.3.1.2. Reactivity Studies

All reactions were carried out in a down-flow fixed-bed reactor at 543 K and atmospheric pressure. The feed composition was 10 mol% CO and 20 mol% H_2O with balance He at a total flow rate of 100 cm^3 min^{-1}. The catalytic activities for WGS of carbon-supported catalysts prepared by CSR are reported in Table 6.3. It is apparent that the Pt/C monometallic parent catalyst has low activity for WGS. Incorporation of Mo onto the parent catalyst, with a Mo:Pt atomic ratio of 0.17, increases the rate per mass of catalyst by more than a factor of 600. Increasing the Mo content causes a nearly proportionate, further improvement in reactivity; the catalyst with the highest Mo loading is over 1500 times more reactive than Pt/C on a mass basis.

The promotional factor in terms of the turnover frequency reaches a maximum of 4110 at an ICP ratio of Mo:Pt = 0.47. For catalysts with higher ICP Mo:Pt ratios, a small decrease in TOF is observed. The saturation point for the effective deposition of Mo onto Pt by controlled surface reactions is at Mo:Pt = 0.47 by ICP. Thus, the observation that the TOF remains relatively constant as the ICP Mo:Pt ratio increases above 0.47 is at least partially caused by the non-selective deposition of Mo. Indeed, the catalytic activities of the bimetallic catalysts depend on the composition of the bimetallic nanoparticles rather than that of the bulk catalyst.

Table 6.3. WGS reactivity summary of carbon-supported PtMo catalysts.

Catalyst ID	Atomic Mo:Pt (ICP)	Rate (μmol g^{-1} s^{-1})	TOF (ks^{-1})	TOF Promotional Factor
Pt/C	0	0.0064	0.044	1
CSR-PtMo/C- 1b	0.17	3.9	47	1070
CSR-PtMo/C- 2b	0.34	7.9	104	2360
CSR-PtMo/C- 3b	0.47	9.4	181	4110
CSR-PtMo/C- 4b	0.54	8.8	151	3430
CSR-PtMo/C- 5b	0.61	10.0	158	3590

6.3.1.3. XAS analysis for supported PtMo catalysts

Pt L_{III}-edge (11.564 keV) and Mo K-edge (20.000 keV) X-ray absorption measurements were conducted on the bending magnet beamline of the Materials Research Collaborative Access Team (MRCAT, 10-BM) at the Advanced Photon Source at Argonne National Laboratory. Measurements were made in transmission scan mode with steps from 250 eV before the edge and 1000 eV beyond the edge for both edges. Ionization chambers were optimized for linear response (ca. 10^{10} photons s^{-1}) using a mixture of He, N_2 and Ar gases for 10% and 70% absorption in I_o and I_t respectively. The Pt or Mo foil spectrum was acquired simultaneously with each catalyst scan for energy calibration.

The catalysts were treated in a continuous flow reactor, which consisted of a quartz tube (1 in. OD, 10 in. length) sealed with Kapton film windows by Ultra-Torr fittings at the ends. These fittings had ball valves welded onto them to allow gas to flow through. Catalysts were pressed into self-supporting wafers in a cylindrical holder consisting of six wells (six shooter), and the catalyst amount was calculated to give an absorbance (μx) of ~1.0. This six-shooter was placed inside the flow reactor in contact with a K type thermocouple (Omega), and the catalysts were reduced with flowing 3.5% H_2/He. The catalysts were reduced at the desired temperature for 1 h, purged with He for 15 min, and then cooled to room temperature in He. All XAS spectra were collected on reduced catalysts at room temperature under a static He environment.

The normalized, energy calibrated spectra were obtained by standard protocol using the WinXAS 3.2 software. Edge energy was determined from the maximum in the first derivative of the X-ray absorption near edge structure (XANES) spectrum. Experimental phase shift and backscattering amplitudes functions were obtained from the Pt foil for Pt-Pt (12 at 2.77 Å), and Mo foil for Mo-Mo (8 at 2.76 Å). In addition to the foils, reference compounds, namely Mo_2C (3 Mo-C at 2.09 Å and 12 Mo-Mo at 2.97 Å) and Na_2MoO_4 (4 Mo-O at 1.77 Å) were also used. Theoretical phase and amplitude functions for Pt-Mo and Mo-Pt were calculated from a scattering pair using the FEFF6 software. The EXAFS parameters were obtained by a least square fit in R-space of the k^2-weighted Fourier transform (FT) data.

X-ray absorption studies were carried out to probe the structure of the PtMo bimetallic catalysts after reduction pretreatment. Comparison of the EXAFS spectra of a Mo foil and PtMo/C indicates contributions of scattering from both metal-metal coordination and from coordination between the metal and a light element (e.g., O or C). The average bond lengths of Mo=O, Mo-O and Mo-Mo from reference compounds are 1.69 Å, 1.77 Å and 2.76 Å respectively.[20] We were able to obtain good fits (Table 6.4 and Table 6.5 for the Pt L_{III}-edge and Mo K-edge, respectively) with Mo-O bond distance of 2.06 Å, suggesting that not all Mo in the particles is in the form of MoO_2 or MoO_3, but rather is a highly reduced mixture of different Mo oxidation states.

Table 6.4. EXAFS fits of Pt L_{III}-edge for PtMo/C catalysts reduced at varying reduction temperatures assuming formation of molybdenum oxide.

Sample	Treatment/Scan condition	Scatterer	N	R (Å)	$\Delta\sigma^2$ x10^3 (Å)	E_0 (eV)
CSR-PtMo/C-1b	H_2 473 K/ He RT	Pt-Pt	7.8	2.71	2.0	-3.6
		Pt-Mo	1.7	2.69	2.0	14.7
	H_2 673 K/ He RT	Pt-Pt	7.5	2.71	2.0	-3.8
		Pt-Mo	1.5	2.69	2.0	10.8
CSR-PtMo/C-2b	H_2 473 K/ He RT	Pt-Pt	7.0	2.71	2.0	-3.8
		Pt-Mo	1.7	2.69	2.0	11.0
	H_2 673 K/ He RT	Pt-Pt	7.0	2.71	2.0	-3.9
		Pt-Mo	1.9	2.69	2.0	8.9
CSR-PtMo/C-3b	H_2 473 K/ He RT	Pt-Pt	7.2	2.71	2.0	-3.8
		Pt-Mo	1.8	2.69	2.0	12.1
	H_2 673 K/ He RT	Pt-Pt	7.2	2.71	2.0	-4.0
		Pt-Mo	2.0	2.69	2.0	9.3
CSR-PtMo/C-4b	H_2 473 K/ He RT	Pt-Pt	7.3	2.71	2.0	-3.9
		Pt-Mo	2.0	2.69	2.0	11.8
	H_2 673 K/ He RT	Pt-Pt	7.1	2.71	2.0	-4.2
		Pt-Mo	2.3	2.69	2.0	8.9
CSR-PtMo/C-5b	H_2 473 K/ He RT	Pt-Pt	7.1	2.71	2.0	-3.9
		Pt-Mo	1.9	2.69	2.0	11.8
	H_2 673 K/ He RT	Pt-Pt	6.9	2.71	2.0	-4.2
		Pt-Mo	2.4	2.69	2.0	8.1
CSR-PtMo/SiO_2-1c	H_2 473 K/ He RT	Pt-Pt	10.2	2.74	2.0	-2.0
		Pt-Mo	0.5	2.72	2.0	13.2
	H_2 673 K/ He RT	Pt-Pt	9.8	2.74	2.0	-1.5
		Pt-Mo	0.8	2.72	2.0	12.8
CSR-PtMo/SiO_2-2c	H_2 473 K/ He RT	Pt-Pt	10.0	2.74	2.0	-2.3
		Pt-Mo	0.4	2.72	2.0	14.2
	H_2 673 K/ He RT	Pt-Pt	9.9	2.74	2.0	-2.1
		Pt-Mo	1.3	2.72	2.0	12.0

The estimated uncertainties are: N, ±10%; R, ±0.02 Å

Table 6.5. EXAFS fits of Mo K-edge for PtMo/C catalysts reduced at varying reduction temperatures assuming formation of molybdenum oxide.

Sample	Treatment/Scan condition	Scatterer	N	R (Å)	$\Delta\sigma^2$ x10^3 (Å)	E_0 (eV)
CSR-PtMo/C-1b	H_2 473 K/ He RT	Mo-O	1.7	2.06	2.0	4.8
		Mo-Pt	2.6	2.69	2.0	-0.6
	H_2 673 K/ He RT	Mo-O	0.9	2.06	2.0	6.6
		Mo-Pt	4.2	2.69	2.0	1.3
CSR-PtMo/C-2b	H_2 473 K/ He RT	Mo-O	1.5	2.06	2.0	5.5
		Mo-Pt	2.2	2.69	2.0	0.2
	H_2 673 K/ He RT	Mo-O	1.2	2.06	2.0	5.3
		Mo-Pt	3.6	2.69	2.0	-1.2
CSR-PtMo/C-3b	H_2 473 K/ He RT	Mo-O	2.0	2.06	2.0	5.7
		Mo-Pt	1.9	2.69	2.0	-2.6
	H_2 673 K/ He RT	Mo-O	1.6	2.06	2.0	4.1
		Mo-Pt	3.0	2.69	2.0	-1.6
CSR-PtMo/C-4b	H_2 473 K/ He RT	Mo-O	2.3	2.06	2.0	5.6
		Mo-Pt	1.8	2.69	2.0	-6.1
	H_2 673 K/ He RT	Mo-O	1.9	2.06	2.0	3.8
		Mo-Pt	3.0	2.69	2.0	-1.0
CSR-PtMo/C-5b	H_2 473 K/ He RT	Mo-O	2.2	2.06	2.0	5.1
		Mo-Pt	1.6	2.69	2.0	-4.0
	H_2 673 K/ He RT	Mo-O	1.9	2.06	2.0	3.5
		Mo-Pt	3.2	2.69	2.0	-1.3
CSR-PtMo/SiO_2-1c	H_2 473 K/ He RT	Mo-O	1.3	2.04	2.0	2.0
		Mo-Pt	4.3	2.72	2.0	4.8
	H_2 673 K/ He RT	Mo-O	1.2	2.04	2.0	5.1
		Mo-Pt	5.6	2.72	2.0	4.4
CSR-PtMo/SiO_2-2c	H_2 473 K/ He RT	Mo-O	1.5	2.04	2.0	4.3
		Mo-Pt	3.2	2.72	2.0	4.4
	H_2 673 K/ He RT	Mo-O	1.5	2.04	2.0	1.0
		Mo-Pt	4.4	2.72	2.0	4.9

The estimated uncertainties are: N, ±10%; R, ±0.02 Å

The Pt-Pt coordination from the Pt L_{III}-edge is almost constant, suggesting that the metal particle size does not change considerably over this range of particle composition. This result is in agreement with the STEM results in Table 6.2. As the number of Mo addition cycles increased, the Pt-Mo coordination was observed to increase for the samples reduced at 673 K. The STEM analysis shows that the average Pt particle size for the carbon-supported PtMo catalyst prepared by 2 cycles (CSR-PtMo/C-2b) is 1.31 nm, while that for the corresponding silica-supported PtMo catalyst (CSR-PtMo/SiO_2-2c) is 3.39 nm. This result was also observed in the EXAFS results shown in Figure 6.3, where the total Pt coordination was higher for the catalysts with silica as a support as compared to carbon-supported catalysts.

Fits for the Mo K-edge showed lower total coordination for Mo as compared to the total Pt coordination. In addition, Mo-Mo interactions were not observed in any of the samples. As the Mo loading increased, the Mo-O coordination increased along with a decrease in the Mo-Pt coordination. Furthermore, the Mo-O coordination is lowered when the reduction temperature is increased from 473 to 673 K. In accordance with previous findings, these results suggest that Mo initially favors entering the Pt nanoparticles, but is increasingly coordinated to a light element (*i.e.,* present near the surface) as the Mo content increases and reduction temperature decreases.[19] MoO_x/C species may also contribute to the Mo-O coordination after saturation of the Pt nanoparticles with Mo.

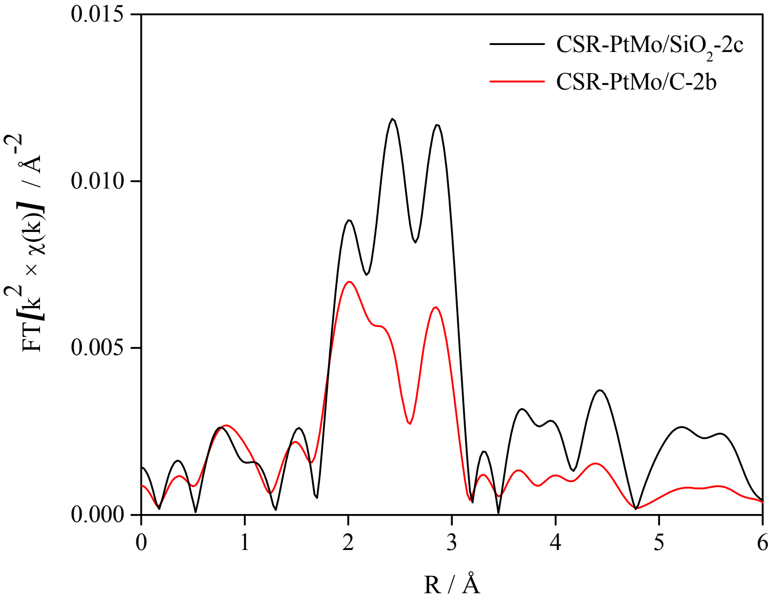

Figure 6.3. Magnitude of k^2-weighted Fourier transform of EXAFS data of Pt L$_{\text{III}}$-edge for CSR-PtMo/C-2b (red), and CSR-PtMo/SiO$_2$-2c (black) (Δk = 2.7-12.0 Å^{-1} and ΔR = 1.8-3.2 Å^{-1}).

The Mo K-edge XANES can be fit as a linear combination of contribution from Mo foil and MoO_2; however, the edge energy is also in agreement with that of Mo-C in Mo_2C. Since the measurements were obtained for catalysts for both the carbon supported and silica supported samples, the origin of the possible carbon species could be the organometallic precursor (cycloheptatriene molybdenum(0) tricarbonyl) used for Mo. The experimental XAS data, thus, were fit assuming the formation of molybdenum carbide (Table 6.6 and Table 6.7). The fits for both the Pt L$_{\text{III}}$-edge and Mo K-edge assuming formation of molybdenum carbide have nearly the same trends as the fits assuming molybdenum oxide.

Table 6.6. EXAFS fits of Pt L$_{III}$-edge for PtMo/C catalysts reduced at varying reduction temperatures assuming formation of molybdenum carbide.

Sample	**Treatment/Scan condition**	**Scatterer**	**N**	**R (Å)**	**$\Delta\sigma^2$ x10^3 (Å)**	**E_0 (eV)**
CSR-PtMo/C-1b	H_2 473 K/ He RT	Pt-Pt	7.8	2.73	2.0	-2.2
		Pt-Mo	1.6	2.71	2.0	13.5
	H_2 673 K/ He RT	Pt-Pt	7.4	2.73	2.0	-2.3
		Pt-Mo	1.6	2.71	2.0	9.0
CSR-PtMo/C-2b	H_2 473 K/ He RT	Pt-Pt	7.0	2.73	2.0	-2.3
		Pt-Mo	1.6	2.71	2.0	9.8
	H_2 673 K/ He RT	Pt-Pt	6.9	2.73	2.0	-2.5
		Pt-Mo	2.0	2.71	2.0	8.0
CSR-PtMo/C-3b	H_2 473 K/ He RT	Pt-Pt	7.2	2.73	2.0	-2.4
		Pt-Mo	1.7	2.71	2.0	11.0
	H_2 673 K/ He RT	Pt-Pt	7.1	2.73	2.0	-2.7
		Pt-Mo	2.2	2.71	2.0	8.9
CSR-PtMo/C-4b	H_2 473 K/ He RT	Pt-Pt	7.3	2.73	2.0	-2.6
		Pt-Mo	1.9	2.71	2.0	11.0
	H_2 673 K/ He RT	Pt-Pt	7.1	2.73	2.0	-2.8
		Pt-Mo	2.4	2.71	2.0	9.0
CSR-PtMo/C-5b	H_2 473 K/ He RT	Pt-Pt	7.1	2.73	2.0	-2.5
		Pt-Mo	1.9	2.71	2.0	9.7
	H_2 673 K/ He RT	Pt-Pt	6.9	2.73	2.0	-2.7
		Pt-Mo	2.5	2.71	2.0	8.5
CSR-PtMo/SiO_2-1c	H_2 473 K/ He RT	Pt-Pt	10.0	2.75	2.0	-1.2
		Pt-Mo	0.6	2.73	2.0	12.7
	H_2 673 K/ He RT	Pt-Pt	9.8	2.75	2.0	-0.7
		Pt-Mo	0.8	2.73	2.0	8.8
CSR-PtMo/SiO_2-2c	H_2 473 K/ He RT	Pt-Pt	10.0	2.75	2.0	-1.3
		Pt-Mo	0.9	2.73	2.0	14.4
	H_2 673 K/ He RT	Pt-Pt	9.9	2.75	2.0	-1.3
		Pt-Mo	1.3	2.73	2.0	10.3

The estimated uncertainties are: N, ±10%; R, ±0.02 Å

Table 6.7. EXAFS fits of Mo K-edge for PtMo/C catalysts reduced at varying reduction temperatures assuming formation of molybdenum carbide.

Sample	Treatment/Scan condition	Scatterer	N	R (Å)	$\Delta\sigma^2$ x10^3 (Å)	E_0 (eV)
CSR-PtMo/C- 1b	H_2 473 K/ He RT	Mo-C	3.4	2.09	0.0	5.1
		Mo-Pt	2.6	2.71	3.0	1.3
	H_2 673 K/ He RT	Mo-C	2.0	2.09	0.0	4.2
		Mo-Pt	4.4	2.71	3.0	2.5
CSR-PtMo/C- 2b	H_2 473 K/ He RT	Mo-C	3.2	2.09	0.0	5.5
		Mo-Pt	2.1	2.71	3.0	2.4
	H_2 673 K/ He RT	Mo-C	2.5	2.09	0.0	4.5
		Mo-Pt	3.4	2.71	3.0	2.3
CSR-PtMo/C- 3b	H_2 473 K/ He RT	Mo-C	4.0	2.09	0.0	6.0
		Mo-Pt	1.8	2.71	3.0	-1.5
	H_2 673 K/ He RT	Mo-C	3.1	2.09	0.0	2.8
		Mo-Pt	3.0	2.71	3.0	2.2
CSR-PtMo/C- 4b	H_2 473 K/ He RT	Mo-C	4.5	2.09	0.0	5.5
		Mo-Pt	1.6	2.71	3.0	-4.5
	H_2 673 K/ He RT	Mo-C	3.7	2.09	0.0	2.9
		Mo-Pt	2.8	2.71	3.0	2.6
CSR-PtMo/C- 5b	H_2 473 K/ He RT	Mo-C	4.8	2.09	0.0	5.6
		Mo-Pt	1.8	2.71	3.0	-4.6
	H_2 673 K/ He RT	Mo-C	3.9	2.09	0.0	2.5
		Mo-Pt	2.8	2.71	3.0	3.2
CSR-PtMo/SiO_2- 1c	H_2 473 K/ He RT	Mo-C	2.8	2.11	0.0	5.6
		Mo-Pt	4.5	2.73	3.0	6.6
	H_2 673 K/ He RT	Mo-C	2.4	2.10	0.0	8.7
		Mo-Pt	6.1	2.73	3.0	4.8
CSR-PtMo/SiO_2- 2c	H_2 473 K/ He RT	Mo-Pt	3.1	2.09	0.0	6.1
		Mo-C	3.4	2.73	3.0	5.7
	H_2 673 K/ He RT	Mo-Pt	3.4	2.10	0.0	3.4
		Mo-C	4.7	2.73	3.0	4.6

The estimated uncertainties are: N, ±10%; R, ±0.02 Å

The EXAFS data shows that Mo is coordinated to a light scatterer, which can be either O forming a molybdenum oxide species, or C forming a molybdenum carbide species. If Mo is coordinated with C, then the active site for WGS could be Mo-carbide species on the Pt surface. The CSR technique selectively deposits Mo onto Pt, thereby minimizing the formation of Mo_2C on the support, especially for the lower Mo loadings, as evidenced by EDS analysis. The EXAFS results and the linear increase in the turnover frequency with increasing Mo loading suggests that the active sites for WGS reaction under the conditions studied herein are Pt moieties in close contact with Mo moieties i.e. MoO_x or MoC_x.

6.3.2. Supported AuMo catalysts for Reverse Water-Gas Shift Reaction

Supported gold catalysts with highly dispersed nanoparticles have received considerable attention for an increasing number of reactions such as CO oxidation,[21] hydrogen dissociation,[22] formic acid decomposition,[23] water-gas shift,[24,25] and the selective and total oxidation of hydrocarbons.[26] The major factors contributing to the catalytic activity are thought to be under-coordinated Au atoms,[27] the geometry of the Au clusters,[28] the oxidation state of Au atoms,[29] and the interface between Au and the metal oxide support.[22,30] Activation of reactants at the Au-metal oxide interface is widely proposed to be a key step for reactions such as H_2 dissociation, CO oxidation, water-gas shift (WGS), and reverse water-gas shift (RWGS). Ribeiro and co-workers elucidated the effect of the interface on water activation and determined that the WGS reaction rate scales linearly with the amount of under-coordinated Au atoms, estimated from physical models of Au clusters and particle size measurements.[24,25] Specifically, under-coordinated perimeter and corner sites were found to dominate the reactivity, with the corner sites being more active than the perimeter sites. Accordingly, in the present work we have explored an approach to identify and quantitatively assess the active sites involved in the RWGS reaction over supported

Au catalysts, both metallic and interfacial. In these studies, we have used a Au/SiO_2 catalyst to study the activity of under-coordinated Au sites, and we then modified this material with molybdenum oxides moieties using the controlled surface reactions synthesis (CSR) approach as described in Section 6.3.1.1. Using this technique, it is possible to uniformly deposit Mo moieties on supported Pt nanoparticles with negligible deposition on the support. Therefore, we hypothesize that the deposition of Mo will selectively occur on these under-coordinated sites during CSR of AuMo. To test this hypothesis, we have utilized a variety of characterization tools such as sub-ambient CO FTIR, XAS, and Raman spectroscopy to probe the effect of Mo on the reactivity of the catalyst, the state of Au and Mo, and the number of active sites under different conditions.

6.3.2.1. Catalyst Preparation and Characterization

A 4 wt% Au/SiO_2 catalyst was prepared by the deposition-precipitation method. 2.0 g of dry silica (Cab-o-Sil EH-5) was dispersed in 400 mL of a 2 mM chloroauric acid (Sigma-Aldrich) solution at room temperature. The pH of the mixture was adjusted to 9 by drop-wise addition of 2.5 M ammonium hydroxide (Sigma-Aldrich). The mixture was aged for 6 h under vigorous stirring at room temperature and was then filtered and washed with deionized water to remove chloride ions. The sample was dried overnight at 373 K in air. The dried catalyst was reduced in a flow-through cell at a temperature of 623 K (with a heating rate of 2 K min^{-1}) under pure hydrogen flow (30 cm^3 min^{-1}) for 4 h. The reduced sample was then transferred to an inert atmosphere glove box. $AuMo/SiO_2$ catalysts were prepared by addition of Mo onto the parent Au/SiO_2 using a modified CSR method.[19] A solution of cycloheptatriene molybdenum tricarbonyl (Strem Chemicals) in n-pentane (1 mg precursor/g solvent) was added to the 4 wt% Au/SiO_2 catalyst inside the glove box. The mixture was stirred for 2 h inside the glove box and transferred to a vacuum oven where the sample was dried overnight at 318 K. The dried sample was stored inside the glove box until use. Hereafter, AuMo/SiO_2 samples will be referred as to AuMo X, where X = the Mo/Au atomic ratio. Mo/SiO_2 samples were prepared by depositing the organometallic Mo precursor following the same method as for AuMo/SiO_2.

The number of Au and AuMo sites were determined from FTIR spectra of adsorbed CO collected at sub-ambient temperatures (e.g., 150 – 270 K). Bands at 2111 and 2122 cm^{-1} can be attributed to CO adsorbed on under-coordinated Au^0 and $Au^{\delta+}$ species, respectively. Correlations of RWGS reactivity with changes in FTIR spectra for samples containing different amounts of Mo indicate that the interfacial sites are an order of magnitude more active than Au sites for the RWGS reaction. FTIR spectra of CO adsorbed on the Au^0 and $Au^{\delta+}$ sites on Au/SiO_2 and AuMo/SiO_2 show that metallic sites are more abundant after reduction whereas oxidized sites prevail under RWGS reaction conditions. Calcination of the catalysts increases the quantity of under-coordinated Au sites, which is responsible for an increase in RWGS activity. Raman spectra of Mo/SiO_2 show a feature at 975 cm^{-1}, attributed to a dioxo $(O=)_2Mo(-O-Si)_2$ species not observed in spectra of AuMo/SiO_2 catalysts, indicating preferential deposition of Mo on Au.

6.3.2.2. Reactivity Measurements

RWGS reaction studies were conducted in a fixed-bed down-flow reactor at 573 K and 8.1 bar pressure. The conversions were maintained below 5% to achieve to ensure differential reactor operation. Deposition of Mo onto Au/SiO_2 by CSR increases the rate at all Mo levels as compared to Au/SiO_2 (Figure 6.4). Calcination of the catalysts increases the rate measured for all the catalysts, but the effect of calcination is more marked at lower Mo levels. This result agrees with the infrared measurements where the CO uptake after calcination shows a higher increase at low Mo loadings. Importantly, while calcined Au shows the highest increase in the rate compared to its as-synthesized counterpart (by a factor of 3), the rate for as-synthesized AuMo 0.1 is an order of magnitude higher than that of as-synthesized Au. This result indicates that a combination of Au and interfacial AuMo sites formed during CSR are much more active than Au sites alone.

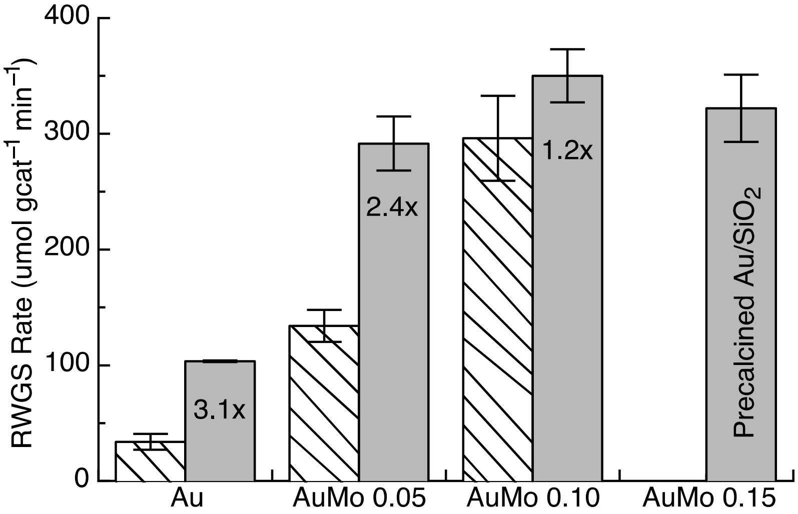

Figure 6.4. RWGS at 573 K and 8.1 bar with H_2:CO_2 = 2:1 for as-synthesized (hashed bars) and calcined (gray bars) Au/SiO_2 and AuMo/SiO_2. Numbers inside the gray bars show the increase in the rate after calcination.

6.3.2.3. XAS analysis for supported AuMo catalysts

Au L_{III}-edge (11.919 keV) and Mo K-edge (20.000 keV) X-ray absorption spectroscopy (XAS) measurements were performed on the beam lines of the Materials Research Collaborative Access Team (MRCAT, 10-BM and 12-BM) at the Advanced Photon Source (APS) at Argonne National Laboratory. Ionization chambers were optimized to provide maximum current with a linear response (~10^{10} photons detected s^{-1}). The X-ray beam was 0.25 mm^2 and data were collected in both transmission and fluorescence modes. A Canberra 13 element Ge Array detector was used to collect fluorescence data at Sector 12BM, whereas transmission scans were obtained at Sector 10BM. A third detector in series was used to simultaneously collect a foil reference spectrum with each measurement for energy calibration. All catalysts were pretreated in a continuous-flow reactor, consisting of a quartz tube (1 inch OD, 10 inch length) sealed with Kapton windows by two Ultra-Torr fittings. A ball valve was welded to each Ultra-Torr fitting to enable gas flow through the reactor. An internal K-type thermocouple was fixed against the catalyst sample holder to monitor temperature. Catalyst samples were pressed into a cylindrical sample holder consisting of six wells, each forming a self-supporting pellet. The mass of catalyst was selected to give an absorbance (μx) of approximately 1.0. The catalysts were reduced in flowing 3.5% H_2 in He (50 cm^3 min^{-1}) at 573 K, purged with flowing He for 10 min and then cooled to room temperature. Calcination treatments were performed by flowing air at 573 K, cooling to room temperature and performing the reduction procedure detailed above. XAS spectra were collected for the reduced samples before and after calcination. Traces of oxygen and moisture in the H_2 and He were removed by means of a purifier (Matheson PUR-Gas Triple Purifier Cartridge).

Table 6.8. Elemental composition of the AuMo catalysts under study.

Sample	**Catalyst ID**	**Au (wt%)**	**Mo (wt%)**
AuMo/SiO_2	AuMo 0.1	4	0.2
AuMo/SiO_2	AuMo 0.5	4	1.0

Using STEM analysis, the particle size for AuMo 0.1 was determined to be 1.7 ± 1.3 nm. Frenkel *et al.* have developed correlation between the average first shell coordination number and the particle diameter for Pt nanoparticles assuming the particles to be hemispherical cuboctahedrons.[9] Since both Pt and Au are fcc metals, this correlation could be applied to determine the particle size for Au nanoparticles. From the EXAFS fitting (Figure 6.5) of the spectrum for AuMo 0.1 from the Au L_{III}-edge, we obtained the following values: N = 7.1, R= 2.82 Å. The first shell average coordination of 7.1 relates to a nanoparticle size of 1.5 nm. This value is consistent with the average particle size determined using STEM.

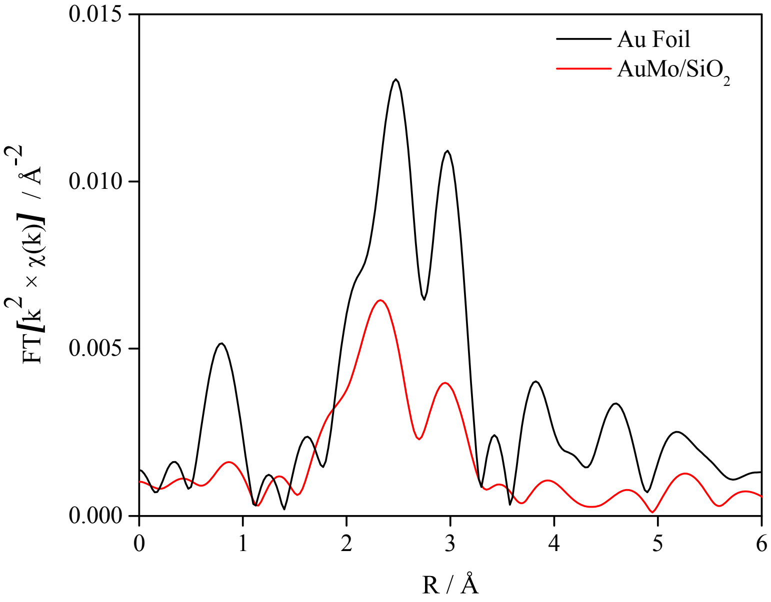

Figure 6.5. Magnitude of k^2-weighted Fourier Transform of EXAFS data at Au LIII-edge for Au foil and AuMo 0.1 catalyst reduced at 573 K and scanned in He at room temperature (Δk = 3.1-12.0 Å^{-1}).

X-ray adsorption near edge spectroscopy was used to determine the extent of Mo oxidation in the Mo/SiO_2 and AuMo/SiO_2 samples. The elemental composition of the catalysts is listed in Table 6.8. Fluorescence data, Figure 6.6, were collected after the samples were calcined and reduced in H_2. According to fits of the XANES curves, Mo in the analyzed Mo and AuMo samples is in a high oxidation state (e.g., Mo^{+6}). Importantly, this result suggests that Au and Mo exist as a metal-metal oxide combination, and not as bimetallic alloy, as has been observed for the case of PtMo.[31]

The edge energy of a XANES spectrum was determined from the maximum in the first derivative of the leading edge. The edge energy of the reference foil was determined for each sample and the difference in the edge energy from 20.000 keV was used to correct data for that sample. The XANES spectra and first derivative of the scans are shown in Figure 6.7. The edge energies calculated from the first derivative are given in Table 6.9.

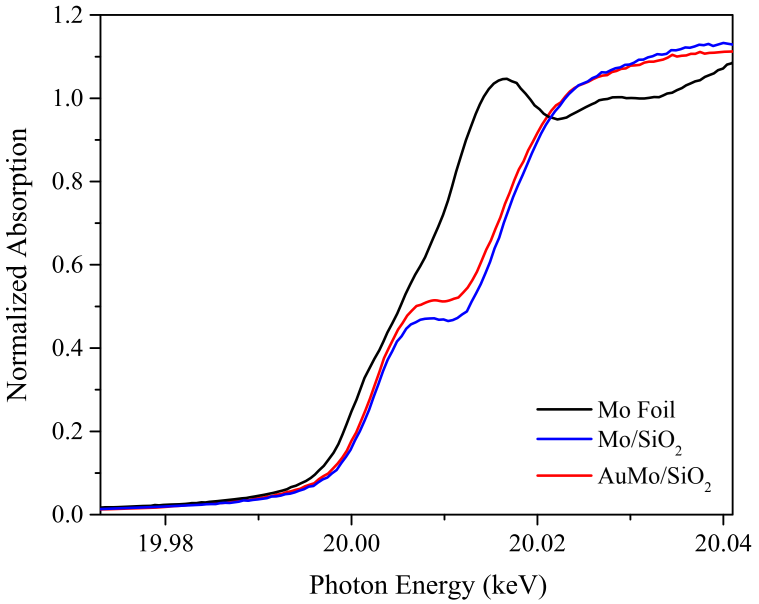

Figure 6.6. Mo K-edge XANES fluorescence data characterizing reduced (573 K) Mo/SiO$_2$ and AuMo/SiO$_2$ after calcination at 573 K. The Mo loading for all samples was 0.2 wt% (AuMo 0.1).

XAS studies of Mo addition to supported Pt catalysts have been reported by Ribeiro, *et al.*[1] In agreement with the findings by Ribeiro *et al.*, Mo is highly reduced in the PtMo/SiO$_2$ sample upon reduction at 573 K. Moreover, the Mo in the PtMo/SiO$_2$ sample is in a more reduced state than in the AuMo/SiO$_2$ sample. This conclusion is indicated by the chemical shift towards higher energy as we go from PtMo to AuMo. The Mo on these AuMo samples is in a high oxidation state (*e.g.*, Mo^{6+}).

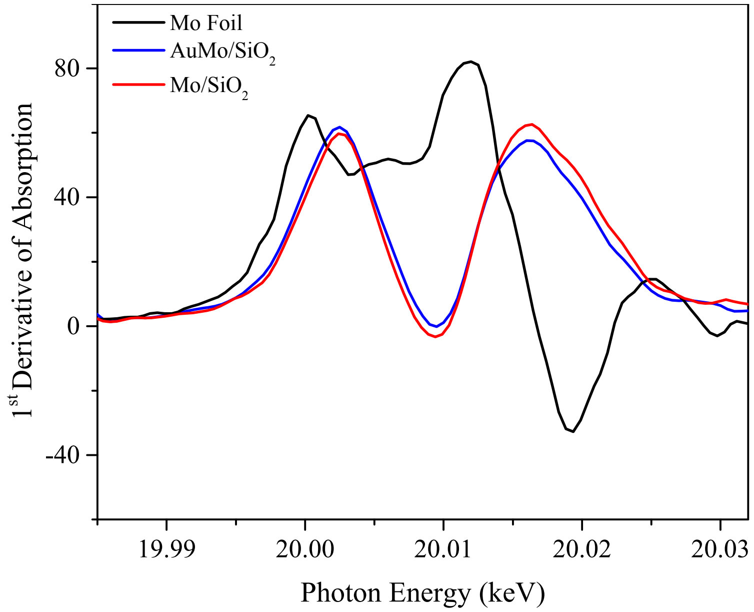

Figure 6.7. First derivative of the Mo K-edge XANES for Mo foil, AuMo/SiO$_2$, and Mo/SiO$_2$ catalysts. The pretreatment conditions are given in Table 6.9.

Transmission spectra for samples with higher Mo loading samples, Figure 6.8, indicate a slightly different behavior for AuMo. In particular, when the AuMo samples are only pretreated in hydrogen, the Mo is in a more reduced state, existing as a mixture of Mo^{+4} and Mo^{+6}. Calcination of this same sample, however, leads to oxidation of the Mo, and only Mo^{+6} was observed. Altogether, the XANES results indicate that the Au-Mo interactions observed by FTIR and Raman spectroscopy stem from Au-MoO$_x$ species.

Table 6.9. Mo K-edge energy as determined from the maximum point of the first derivative from XANES.

Sample	Treatment	Edge Energy (eV)	Oxidation State
Mo Foil	-	20000.2	0
Na$_2$MoO$_4$	-	20018.0	6
Mo/SiO$_2$	O$_2$ at 573 K, scan in He RT	20016.5	6
AuMo/SiO$_2$	O$_2$ at 573 K, scan in He RT	20016.4	6

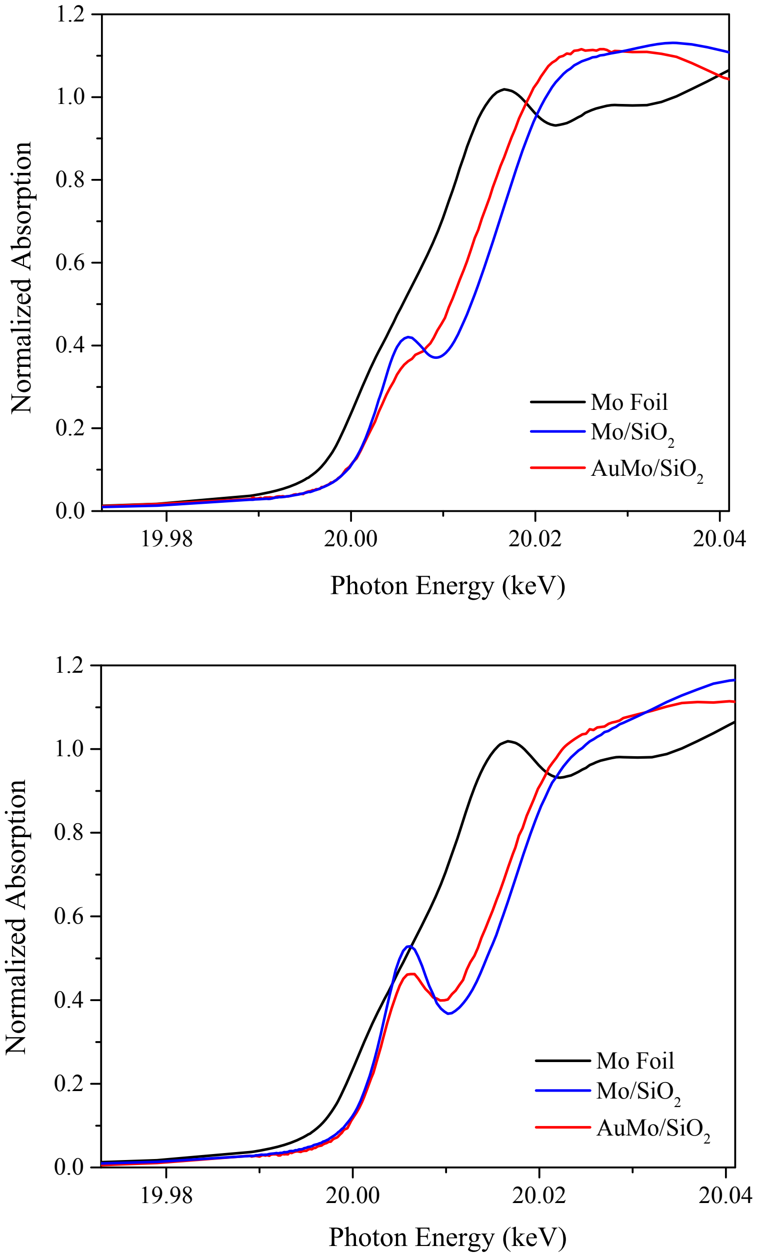

Figure 6.8. Mo K-edge XANES transmission data characterizing reduced silica-supported samples after a) reduction and b) calcination at 573 K. The Mo loading for all samples was 1 wt% (AuMo 0.5).

Results from reactivity, CO FTIR, Raman spectroscopy and x-ray absorption spectroscopy indicate that the deposition of Mo onto Au nanoparticles occurs preferentially on under-coordinated Au sites to form Au/MoO_x interfacial sites that are active for RWGS (Figure 6.9).

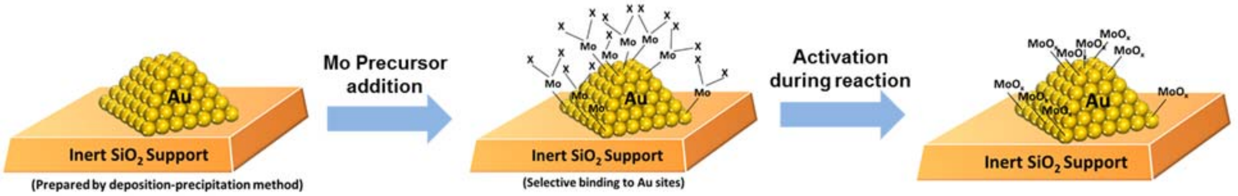

Figure 6.9. Deposition of Mo using CSR on the under-coordinated Au sites to form Au/MoO_x interfacial sites.

6.3.3. Supported RhRe catalysts for Hydrogenolysis of THP-2M

Supported bimetallic catalysts containing a reducible metal and an oxophilic promoter are known to selectively catalyze C-O hydrogenolysis reactions for conversion of biomass-derived intermediates to value-added chemicals.[32-34] Chia and co-workers have reported selective C-O cleavage for a variety of cyclic ethers and polyols over RhRe/C.[34] Hydrogenolysis of tetrahydropyran-2-methanol (THP-2M) to 1,6-hexanediol with >90% selectivity has been achieved using Re promoted Rh catalysts (Figure 6.10). C-O hydrogenolysis over RhRe/C has been proposed to occur through a bifunctional mechanism involving acid-catalyzed ring opening at the Re site followed by the metal-catalyzed hydrogenation at a nearby Rh site.[34,35] Multiple studies have shown that neither Rh nor Re alone is effective for the conversion of THP-2M and that a synergistic interaction between them is necessary for C-O hydrogenolysis to take place.[34-37] In this study, we have investigated the effect of carbon supports on the formation of RhRe bifunctional catalysts.

Carbon is available in various allotropic forms which have long been used as catalyst supports. Both the physical properties and surface chemistry of various forms of carbon can affect the properties of metal impregnated onto them. Metal precursors can anchor to the surface functional groups, such as -OH and -COOH, present on carbon.[38] Each precursor possesses different affinity to the surface and its surface mobility can be inhibited owing to this anchoring. Little attention has been given to the effect of physical and chemical properties of the support carbons on the structure and activity of the metals loaded onto them. In lieu of this fact, we have prepared RhRe catalysts on two different carbon supports- Norit Darco 12X40 (NDC by Cabot Corp., an activated carbon) and Vulcan XC72 (VXC by Cabot Corp., a carbon black) for probing their reactivity towards THP-2M hydrogenolysis and have probed the extent of alloy formation on the catalysts using XAS characterization along with other characterization techniques such as STEM, EDS, and Raman spectroscopy.

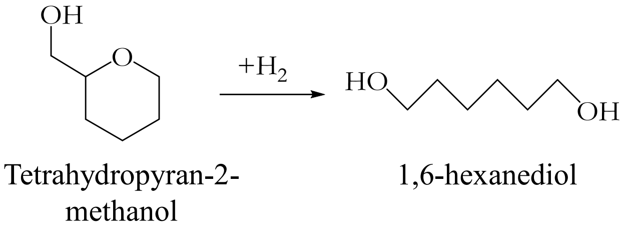

Figure 6.10. Hydrogenolysis of tetrahydropyran-2-methanol to produce 1,6-hexanediol.

6.3.3.1. Catalyst Preparation and Characterization

Single and bimetallic catalysts were prepared by incipient wetness impregnation of the carbon supports with aqueous solutions of $RhCl_3.xH_2O$ (Sigma Aldrich) and NH_4ReO_4 (Sigma Aldrich). The RhRe catalysts were obtained by successive impregnation of dried, unreduced Rh/C with aqueous solution of NH_4ReO_4 (0.12 M). Because of NDC's lower incipient wetness point, the NH_4ReO_4 solution was impregnated in two stages with air-drying the catalyst at 383 K in-between. All RhRe catalysts examined in this work contained 4 wt% Rh with an atomic ratio of Rh:Re = 1.0:0.5. Before use in experiments, catalysts were dried in air at 383 K, reduced in flowing hydrogen at 723 K (unless noted otherwise), and passivated with flowing 1 vol% O_2 in He at room temperature. This reduction and passivation was considered the last step of catalyst synthesis.

Monometallic Re/NDC and Re/VXC with 3.6 wt% Re were prepared by incipient wetness impregnation for use in x-ray absorption spectroscopy studies. The theoretical metal loadings on the catalysts and the CO chemisorption results are listed in Table 6.10. The dispersion of monometallic Rh was higher on NDC support. Addition of Re to Rh/VXC led to a decrease in CO adsorption from 130 μmol g^{-1} to 76 μmol g^{-1} indicating that Re might have covered a fraction of the surface Rh atoms. In contrast, addition of Re onto Rh/C led to an increase in the CO uptake.

Table 6.10. Results of CO pulse chemisorption characterization of the catalysts used in this study.

Catalyst	**Rh loading (wt%)**	**Re loading (wt%)**	**Rh:Re (mol:mol)**	**Irreversible CO uptake (μmol g^{-1})**	**CO:Rh (mol:mol)**
Rh/NDC	4	-	-	204	0.51
RhRe/NDC	3.9	3.6	1:0.5	232	0.60
Rh/VXC	4	-	-	130	0.32
RhRe/VXC	4	3.6	1:0.5	76	0.19

The surface composition of the carbon supports was determined by X-ray photoelectron spectroscopy (XPS) using monochromatic Al K_α x-ray source. The biggest difference between the two carbons was their oxygen content as determined by XPS; NDC carbon has 20 times more surface oxygen than VXC carbon. The higher concentration of oxygen on the surface of NDC is most likely due to acid treatments during the carbon activation process. This XPS result is consistent with the higher water uptake by NDC support determined using water adsorption experiment. The higher oxygen population of the NDC surface may provide sites that can preferentially interact with one of the two metal precursors. Diffuse reflectance infrared Fourier transform spectroscopy (DRIFTS) was performed to probe the functional groups present on the support and it was observed that NDC contains a variety of oxygen-containing functionalities which are present only in small amounts on the VXC support.

6.3.3.2. Reactivity Studies

The hydrogenolysis of THP-2M over RhRe/VXC and RhRe/NDC was performed in a 50 mL batch reactor. The conversion of THP-2M reached 72% in 74 h over RhRe/VXC whereas that over RhRe/NDC reached only 10% in 28 h (Figure 6.11). The selectivity to 1,6-haxanediol was >90% over RhRe/VXC throughout the reaction. Small quantities of 1-hexanol, 2-MTHP, 1-pentanol and THP were also formed. The maximum selectivity towards 1,6-hexanediol observed over RhRe/NDC, however, was only 10%. The specific rate of C-O hydrogenolysis was 76 and 1 μmol g^{-1} min^{-1} over RhRe/VXC and RhRe/NDC respectively. Thus, the hydrogenolysis activity over RhRe/VXC is two orders-of-magnitude higher than that of RhRe/NDC.

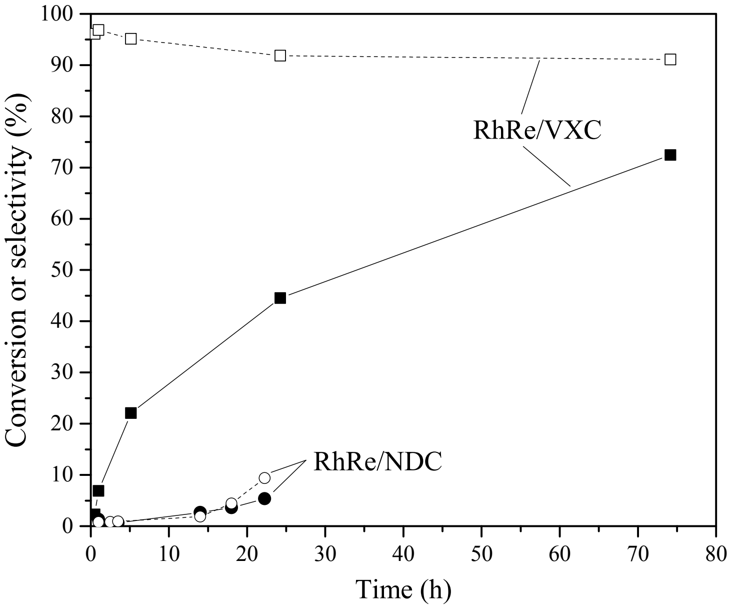

Figure 6.11. Hydrogenolysis of THP-2M in a batch reactor over RhRe/NDC and RhRe/VXC. THP-2M conversion (●) and 1,6-HDO selectivity (○) over RhRe/NDC. THP-2M conversion (■) and 1,6-HDO selectivity (□) over RhRe/VXC. Reaction conditions: 5% aq. THP-2M feedstock (initial reaction volume = 50 mL), mass ratio of catalyst:feedstock = 1:7, 393 K, 40 bar H_2.

6.3.3.3. XAS analysis for carbon-supported RhRe

XAS measurements were performed at the Advanced Photon Source at Argonne National Laboratory using a bending magnet source at X-ray Science Division (XSD) Beamline 20 (20-

BM-B). Ionization chambers were optimized for the maximum current with linear response (ca. 10^{10} photons detected s^{-1}). The Rh K-edge (23.220 keV) and Re L_{III}-edge (10.350 keV) were probed to obtain the extended x-ray absorption fine structure (EXAFS) and x-ray absorption near-edge structure (XANES). All spectra were obtained in transmission mode. A Pt foil (K-edge: 24.35 keV) was used to align the monochromator before Rh K-edge measurements. A Ga foil (K-edge: 10.37 keV) was used to align the monochromator before Re L_{III}-edge measurements. XANES data had a resolution of 0.14 eV. Catalyst samples were pressed into a cylindrical sample holder consisting of six wells, each forming a self-supporting wafer. The catalyst amount used was calculated to give an absorbance (μx) of approximately 1.0 for Rh K-edge measurements and 0.3-0.4 for Re L_{III}-edge measurements (the latter due to high white line absorbance). Catalysts were reduced in a continuous-flow reactor, which consisted of the six-well sample holder placed in the center of a quartz tube (2.54 cm OD, 25.4 cm length) sealed with Kapton windows by two Ultra-Torr fittings. Ball valves were welded to each Ultra-Torr fitting and served as the gas inlet and outlet. An internal K-type thermocouple (Omega) was placed against the catalyst sample holder to monitor the temperature. The catalyst reduction was performed in flowing 3.5 vol% H_2 in He (100 cm^3 min^{-1}) while heating to 473 K at 4 K min^{-1} and holding for 15 min. After the reactor cooled to room temperature, the quartz tube was purged with flowing He for 5 min, sealed by closing the ball valves, and transported to the beamline hutch for XAS analysis. Another sets of scans were taken for each catalyst in its reduced and passivated form.

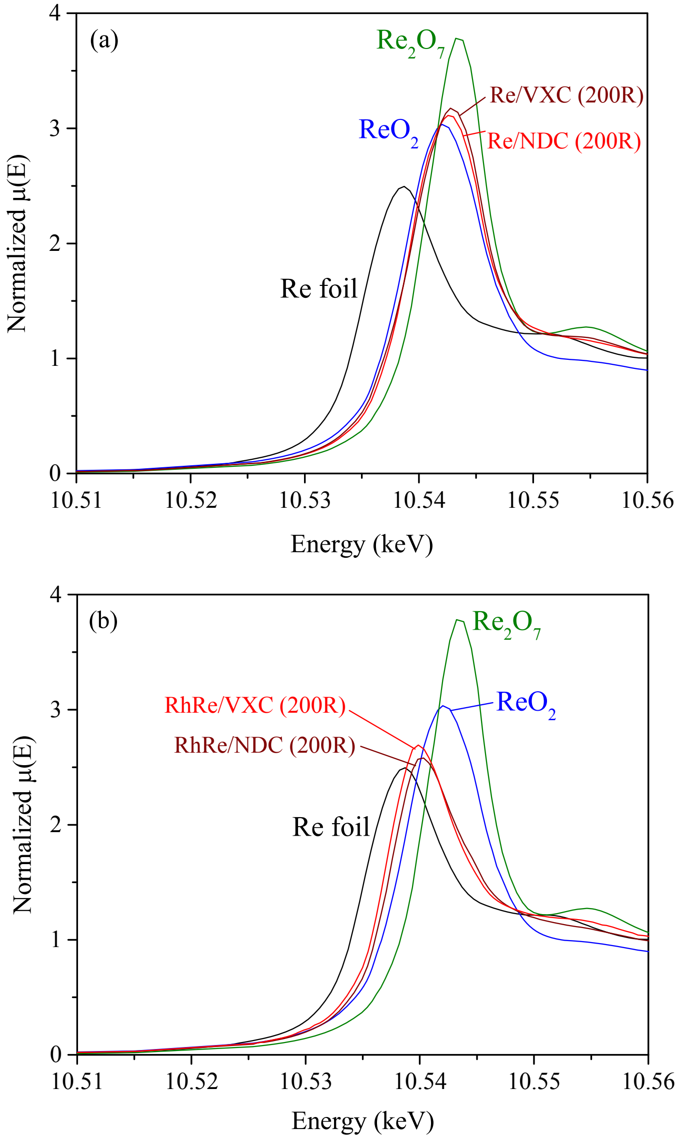

Figure 6.12. Re LIII-edge XANES (10.52 - 10.56 keV) of (a) monometallic Re/NDC and Re/VXC reduced at 473 K and (b) RhRe/NDC and RhRe/VXC reduced at 473 K. Spectra were acquired under *in situ* conditions.

Table 6.11 provides a summary of Rh K-edge and Re LIII-edge XANES fits. The Re LIII-edge XANES of Re foil, ReO_2, Re_2O_7, Re/NDC, and Re/VXC is shown in Figure 6.12. The XANES data shows that rhodium had similar degree of reduction for RhRe/NDC and RhRe/VXC at 473 K (~90% and ~84% reduced, respectively). Monometallic Re in Re/NDC and Re/VXC is fully oxidized even after reduction pretreatment at 473 K, however, Re is reduced in both bimetallic catalysts at 473 K. This is consistent with the report of Chia *et al.*, who showed that (1) temperatures higher than 723 K are required to reduce Re to a metallic state and (2) the presence of metallic Rh promotes the reduction of Re.[39] The Re L_{III}-edge XANES of RhRe/VXC (Figure 6.12(b)) shows that respectively, 83% and 87% of the Re is reduced in these catalysts after reduction at 473 K.

The values of parameters from R-space fits of Rh K-edge and Re L_{III}-edge EXAFS spectra for Rh and Re standards, RhRe/VXC, and RhRe/NDC catalysts are reported in Table 6.12. The Cowley short-range order parameter (α) has been used to estimate the degree of segregation of each species in bimetallic materials.[9,40] A Cowley parameter value $-1 \leq \alpha < 0$ suggests clustering of atoms is not favored, while $0 < \alpha \leq 1$ suggests component segregation. Using the metal-metal coordination values from Table 6.12, the Cowley parameters for Rh in RhRe/NDC and RhRe/VXC were found to be -0.31 and -0.07, respectively. The more negative value for RhRe/NDC suggests less clustering of Rh, owing to smaller Rh particles as also suggested by STEM-EDS analysis. The Cowley parameter for Re in RhRe/NDC is 0.08, versus a value of 0.12 for RhRe/VXC; the difference is well within the error associated with Cowley parameter analysis. This result suggests that the Re is more segregated than the Rh in both RhRe/NDC and RhRe/VXC (positive α values) and even forms some monometallic Re particles as seen from STEM-EDS analysis. It is important to note that over-interpretation based on Cowley parameter should be avoided, as the analysis was originally developed for bulk alloys rather than catalyst nanoparticles.

Table 6.11. Fit of Rh K and Re L_{III}-edge XANES for the monometallic Re/C and RhRe/C catalysts prepared using two different carbon supports.

Catalyst	Treatment/scan condition	Edge energy (keV)	XANES fit		
Rh edge		23.22		Rh(III)	Rh(0)
RhRe/NDC	No/He RT			0.908	0.092
RhRe/VXC	No/He RT			0.550	0.450
RhRe/NDC	H_2 473 K/He RT			0.12	0.88
RhRe/VXC	H_2 473 K /He RT			0.16	0.84
Re edge		10.53	Re(IV)	Re(VII)	Re(0)
Re/NDC	No/He RT		0.630	0.370	-
Re/VXC	No/He RT		0.468	0.532	-
Re/NDC	H_2 473 K /He RT		0.702	0.298	-
Re/VXC	H_2 473 K /He RT		0.642	0.358	-
RhRe/NDC	No/He RT		0.322	0.656	0.022
RhRe/VXC	No/He RT		0.807	-	0.193
RhRe/NDC	H_2 473 K /He RT		0.13	-	0.87
RhRe/VXC	H_2 473 K /He RT		0.17	-	0.83

Several previous studies have used XAS to characterize the supported bimetallic RhRe catalysts to gain understanding about the active site for hydrogenolysis.[39,41,42] XAS characterization is a bulk technique and to accurately represent local co-ordinations in nanoparticles, the nanoparticles should have a uniform composition throughout the catalyst. This is not the case for RhRe/NDC which shows segregation of Re species on the surface.

Table 6.12. Fit of Rh K and Re L_{III}-edge EXAFS for the RhRe/C catalysts prepared using two different carbon supports.

Catalyst	**Treatment/ scan conditions**	**Absorber-backscatterer**	**N**	**R (Å)**	**$\Delta\sigma^2$ ($\times 10^3$ Å^2)**	**ΔE_o (eV)**
Rh edge						
Rh foil	-	Rh-Rh	12.0	2.72		
RhRe/NDC	No/He RT	Rh-Rh	0.2	2.72	3.5	4.8
		Rh-Re	-	-	-	-
		Rh-O	3.6	-	2.7	6
RhRe/VXC	No/He RT	Rh-Rh	2.3	2.72	3.5	-5.4
		Rh-Re	1.5	2.63	2.0	3.6
		Rh-O	3.4	-	7.7	
RhRe/NDC	H_2 473 K/He RT	Rh-Rh	4.8	2.68	2.0	0.6
		Rh-Re	3.7	2.63	2.0	-14.0
		Rh-O	0.6	2.05	1.0	-1.9
RhRe/VXC	H_2 473 K/He RT	Rh-Rh	6.5	2.68	2.0	4.4
		Rh-Re	3.6	2.63	2.0	-4.4
		Rh-O	-	-	-	-
Re edge						
Re foil	-	Re-Re	12.0	2.75		
RhRe/NDC	H_2 473 K/He RT	Re-O	0.4	1.75	1.0	9.7
		Re-Re	3.5	2.66	2.0	-9.3
		Re-Rh	5.6	2.63	2.0	2.7
RhRe/VXC	H_2 473 K/He RT	Re-O	0.2	1.75	1.0	9.3
		Re-Re	4.4	2.66	2.0	-3.8
		Re-Rh	6.3	2.63	2.0	-0.4

Scanning Transmission Electron Microscopy (STEM) and Energy Dispersive X-Ray Spectroscopy (EDS) were performed to obtain the catalyst particle size and composition distribution. The average particle sizes of RhRe/NDC and RhRe/VXC were 1.61 ± 0.61 nm and

1.98 ± 0.73 nm respectively; particles on the NDC support were, on average, larger, but the difference is not statistically significant. Figure 6.13 compares the number distribution of particle compositions in the two samples. Both samples contain measurable populations of monometallic particles.

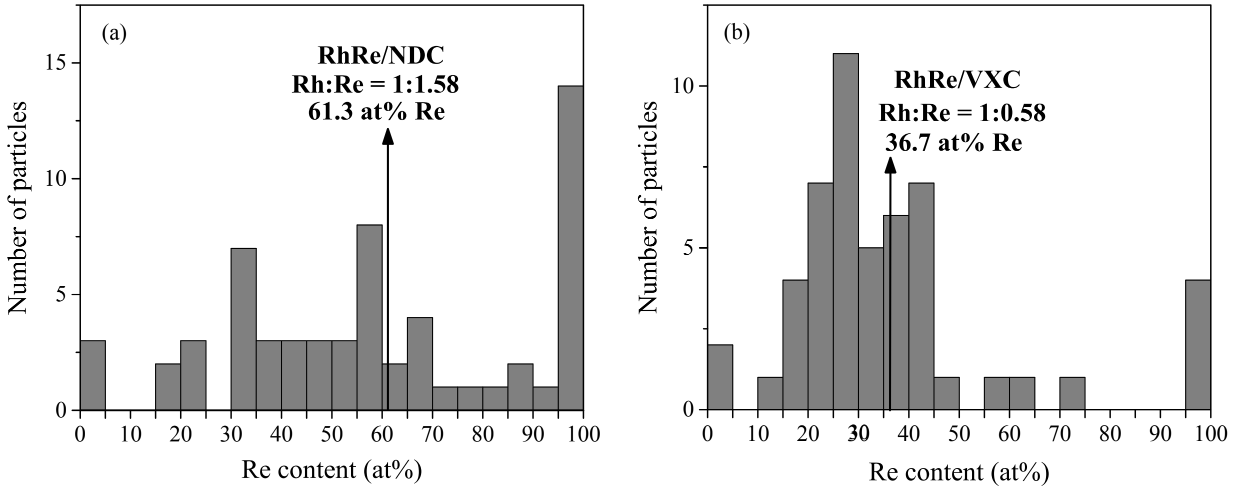

Figure 6.13. Composition distribution for the catalysts obtained by EDS spot beam analysis. (a) RhRe/NDC - Average composition 61.3 atomic % Re determined over 59 particles. (b) RhRe/VXC - Average composition 36.7 atomic % Re determined over 52 particles. Both catalysts have a theoretical composition of 33.3 atomic % Re.

Re-only particles are more common than Rh-only particles, especially in the NDC-supported catalyst; this result is consistent with the Cowley analysis of the EXAFS data. Aside from the monometallic “tails,” the compositions of the particles on the VXC support exhibit an approximately normal distribution, with an average Rh:Re atomic ration 1.0:0.58, very close to both the ratio determined by ICP analysis (1.0:0.51) and the theoretical ratio (1.0:0.50). In contrast, the composition distribution of the NDC-supported metals is flatter. More important, however, is that the average Rh:Re EDS ratio of the NDC-supported catalyst is 1.0:1.58, significantly different from both its ICP and theoretical ratios. The difference suggests that EDS analysis of the NDC-supported material does not detect all of the sample’s Rh content. It is likely that particles on the NDC surface that are too small to be detected in the STEM, below about 1 nm, have large relative

Rh contents.[43] Overall, the STEM/EDS characterization suggests differences in metals distribution on the surfaces of the two carbons. Rh and Re appear to be more uniformly distributed across particles of different size on the VXC surface than on NDC. On NDC, there is evidence of preferential location of Rh in very small particles, leaving larger particles enriched in Re. Thus, based on the STEM/EDS and XAS characterization, a pictorial representation of the catalyst is shown in Figure 6.14.

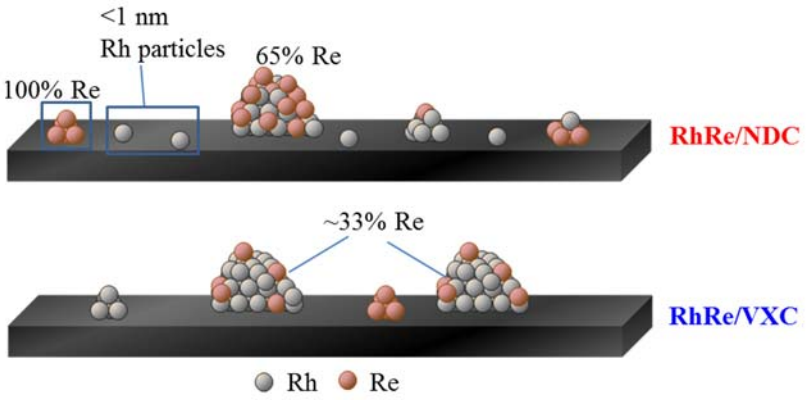

Figure 6.14. Pictorial representation of RhRe/NDC and RhRe/VXC catalysts.

6.4. Conclusions

Supported PtMo catalysts showed higher water gas shift activity as compared to monometallic platinum. A series of catalysts with increasing Mo loadings were prepared using CSR. Using XAS analysis, we observe that with an increase in the number of Mo addition cycles, the Pt-Pt coordination remained constant, suggesting that the metal particle size does not change considerably over this range of particle composition. Fits for the Mo K-edge showed lower total coordination for Mo as compared to the total Pt coordination. In addition, Mo-Mo interactions were not observed in any of the samples. As the Mo loading increased, the Mo-O coordination increased along with a decrease in the Mo-Pt coordination. Mo initially favors entering the Pt nanoparticles, but is increasingly coordinated to a light element present near the surface as the Mo content increases. The EXAFS results and the linear increase in water gas shift TOF with increasing Mo content suggests that the active sites for WGS are Pt moieties in close contact with either MoO_x or MoC_x.

The activity for reverse water gas shift reaction was observed to be an order of magnitude over $AuMo/SiO_2$ than monometallic Au/SiO_2. Combined results from reactivity, CO FTIR, Raman spectroscopy indicate that Mo is deposited preferentially on the undercoordinated Au sites and the resulting Au/MoO_x interfacial sites are the active centers for this conversion.

The hydrogenolysis of THP-2M was investigated over RhRe bimetallic catalysts supported on two varieties of carbon- Norit Darco and Vulcan. The reactivity over RhRe/VXC was observed to be two orders of magnitude higher than RhRe/NDC. Based on STEM/EDS and XAS analyses, metal segregation is observed over Norit carbon to a higher extent than Vulcan carbon thereby decreasing the contact between Rh and Re. The increase in hydrogenolysis activity over RhRe/VXC can thus be explained owing to the higher degree of alloying between Rh and Re on Vulcan carbon.

6.5. Acknowledgements

Much of the work contained in this chapter was performed in collaborative teams and was previously published. Studies on supported PtMo catalysts was published in 2016, and is adapted here with permission from ACS Catalysis.[44] Similarly, the work on silica-supported AuMo was published in 2015, and is adapted here with permission from the Journal of American Chemical Society.[45] The work on RhRe/C, published in 2016 in Catalysis Science & Technology, is open source.[46]

6.6. References

1. Newville, M., Fundamentals of XAFS. Reviews in Mineralogy and Geochemistry 2014, 78 (1), 33-74.
2. Rehr, J. J., Theory and calculations of X-ray spectra: XAS, XES, XRS, and NRIXS. Radiat. Phys. Chem. 2006, 75 (11), 1547-1558.
3. Beard, K. D.; Borrelli, D.; Cramer, A. M.; Blom, D.; Van Zee, J. W.; Monnier, J. R., Preparation and Structural Analysis of Carbon-Supported Co Core/Pt Shell Electrocatalysts Using Electroless Deposition Methods. ACS Nano 2009, 3 (9), 2841-2853.
4. Lambert, S.; Job, N.; D'Souza, L.; Pereira, M. F. R.; Pirard, R.; Heinrichs, B.; Figueiredo, J. L.; Pirard, J. P.; Regalbuto, J. R., Synthesis of very highly dispersed platinum catalysts supported on carbon xerogels by the strong electrostatic adsorption method. J. Catal. 2009, 261 (1), 23-33.
5. Weber, M. J.; Mackus, A. J. M.; Verheijen, M. A.; van der Marel, C.; Kessels, W. M. M., Supported Core/Shell Bimetallic Nanoparticles Synthesis by Atomic Layer Deposition. Chem. Mat. 2012, 24 (15), 2973-2977.
6. Barbier, J.; Marecot, P.; Delangel, G.; Bosch, P.; Boitiaux, J. P.; Didillon, B.; Dominguez, J. M.; Schifter, I.; Espinosa, G., Preparation of platinum-gold bimetallic catalysts by redox reactions. Appl. Catal. A-Gen. 1994, 116 (1-2), 179-186.
7. Jentys, A., Estimation of mean size and shape of small metal particles by EXAFS. PCCP Phys. Chem. Chem. Phys. 1999, 1 (17), 4059-4063.
8. de Graaf, J.; van Dillen, A. J.; de Jong, K. P.; Koningsberger, D. C., Preparation of highly dispersed Pt particles in zeolite Y with a narrow particle size distribution: Characterization by hydrogen chemisorption, TEM, EXAFS spectroscopy, and particle modeling. J. Catal. 2001, 203 (2), 307-321.
9. Frenkel, A. I.; Hills, C. W.; Nuzzo, R. G., A view from the inside: Complexity in the atomic scale ordering of supported metal nanoparticles. J. Phys. Chem. B 2001, 105 (51), 12689-12703.
10. Ravel, B.; Newville, M., Athena, Artemis, Hephaestus: data analysis for X-ray absorption spectroscopy using IFEFFIT. J. Synchrot. Radiat. 2005, 12 (4), 537-541.
11. Ressler, T., WinXAS: a program for X-ray absorption spectroscopy data analysis under MS-Windows. J. Synchrot. Radiat. 1998, 5, 118-122.
12. Lytle, F. W.; Sayers, D. E.; Stern, E. A., Report of the interhnational workshop on standards and criteria in x-ray absorption spectroscopy. Physica B 1989, 158 (1-3), 701-722.
13. Carrasquillo-Flores, R.; Gallo, J. M. R.; Hahn, K.; Dumesic, J. A.; Mavrikakis, M., Density Functional Theory and Reaction Kinetics Studies of the Water-Gas Shift Reaction on Pt-Re Catalysts. ChemCatChem 2013, 5 (12), 3690-3699.
14. He, R.; Davda, R. R.; Dumesic, J. A., In situ ATR-IR spectroscopic and reaction kinetics studies of water-gas shift and methanol reforming on Pt/Al2O3 catalysts in vapor and liquid phases. J. Phys. Chem. B 2005, 109 (7), 2810-2820.
15. Dietrich, P. J.; Sollberger, F. G.; Akatay, M. C.; Stach, E. A.; Delgass, W. N.; Miller, J. T.; Ribeiro, F. H., Structural and catalytic differences in the effect of Co and Mo as promoters for Pt-based aqueous phase reforming catalysts. Appl. Catal. B-Environ. 2014, 156, 236-248.
16. Zhai, Y. P.; Pierre, D.; Si, R.; Deng, W. L.; Ferrin, P.; Nilekar, A. U.; Peng, G. W.; Herron, J. A.; Bell, D. C.; Saltsburg, H.; Mavrikakis, M.; Flytzani-Stephanopoulos, M., Alkali-

Stabilized Pt-OHx Species Catalyze Low-Temperature Water-Gas Shift Reactions. Science 2010, 329 (5999), 1633-1636.

17. Grabow, L. C.; Gokhale, A. A.; Evans, S. T.; Dumesic, J. A.; Mavrikakis, M., Mechanism of the water gas shift reaction on Pt: First principles, experiments, and microkinetic modeling. J. Phys. Chem. C 2008, 112 (12), 4608-4617.
18. Sabnis, K. D.; Cui, Y. R.; Akatay, M. C.; Shekhar, M.; Lee, W. S.; Miller, J. T.; Delgass, W. N.; Ribeiro, F. H., Water-gas shift catalysis over transition metals supported on molybdenum carbide. J. Catal. 2015, 331, 162-171.
19. Hakim, S. H.; Sener, C.; Alba-Rubio, A. C.; Gostanian, T. M.; O'Neill, B. J.; Ribeiro, F. H.; Miller, J. T.; Dumesic, J. A., Synthesis of supported bimetallic nanoparticles with controlled size and composition distributions for active site elucidation. J. Catal. 2015, 328, 75-90.
20. Doonan, C. J.; Stockert, A.; Hille, R.; George, G. N., Nature of the catalytically labile oxygen at the active site of xanthine oxidase. J. Am. Chem. Soc. 2005, 127 (12), 4518-4522.
21. Haruta, M.; Yamada, N.; Kobayashi, T.; Iijima, S., Gold catalysts prepared by coprecipitation for low-temperature oxidation of hydrogen and of carbon monoxide. J. Catal. 1989, 115 (2), 301-309.
22. Fujitani, T.; Nakamura, I.; Akita, T.; Okumura, M.; Haruta, M., Hydrogen Dissociation by Gold Clusters. Angew. Chem.-Int. Edit. 2009, 48 (50), 9515-9518.
23. Ojeda, M.; Iglesia, E., Formic Acid Dehydrogenation on Au-Based Catalysts at Near-Ambient Temperatures. Angew. Chem.-Int. Edit. 2009, 48 (26), 4800-4803.
24. Shekhar, M.; Wang, J.; Lee, W. S.; Williams, W. D.; Kim, S. M.; Stach, E. A.; Miller, J. T.; Delgass, W. N.; Ribeiro, F. H., Size and Support Effects for the Water-Gas Shift Catalysis over Gold Nanoparticles Supported on Model Al2O3 and TiO2. J. Am. Chem. Soc. 2012, 134 (10), 4700-4708.
25. Wang, J.; Kispersky, V. F.; Delgass, W. N.; Ribeiro, F. H., Determination of the Au active site and surface active species via operando transmission FTIR and isotopic transient experiments on 2.3 wt.% Au/TiO2 for the WGS reaction. J. Catal. 2012, 289, 171-178.
26. Stangland, E. E.; Stavens, K. B.; Andres, R. P.; Delgass, W. N., Characterization of gold-titania catalysts via oxidation of propylene to propylene oxide. J. Catal. 2000, 191 (2), 332-347.
27. Xu, Y.; Mavrikakis, M., Adsorption and dissociation of O-2 on gold surfaces: Effect of steps and strain. J. Phys. Chem. B 2003, 107 (35), 9298-9307.
28. Hakkinen, H.; Abbet, W.; Sanchez, A.; Heiz, U.; Landman, U., Structural, electronic, and impurity-doping effects in nanoscale chemistry: Supported gold nanoclusters. Angew. Chem.-Int. Edit. 2003, 42 (11), 1297-1300.
29. Boronat, M.; Illas, F.; Corma, A., Active Sites for H-2 Adsorption and Activation in Au/TiO2 and the Role of the Support. J. Phys. Chem. A 2009, 113 (16), 3750-3757.
30. Bowker, M.; James, D.; Stone, P.; Bennett, R.; Perkins, N.; Millard, L.; Greaves, J.; Dickinson, A., Catalysis at the metal-support interface: exemplified by the photocatalytic reforming of methanol on Pd/TiO2. J. Catal. 2003, 217 (2), 427-433.
31. Williams, W. D.; Bollmann, L.; Miller, J. T.; Delgass, W. N.; Ribeiro, F. H., Effect of molybdenum addition on supported platinum catalysts for the water-gas shift reaction. Appl. Catal. B-Environ. 2012, 125, 206-214.
32. Nakagawa, Y.; Tamura, M.; Tomishige, K., Catalytic Reduction of Biomass-Derived Furanic Compounds with Hydrogen. ACS Catal. 2013, 3 (12), 2655-2668.

33. Buntara, T.; Noel, S.; Phua, P. H.; Melian-Cabrera, I.; de Vries, J. G.; Heeres, H. J., Caprolactam from Renewable Resources: Catalytic Conversion of 5-Hydroxymethylfurfural into Caprolactone. Angew. Chem.-Int. Edit. 2011, 50 (31), 7083-7087.
34. Chia, M.; Pagan-Torres, Y. J.; Hibbitts, D.; Tan, Q. H.; Pham, H. N.; Datye, A. K.; Neurock, M.; Davis, R. J.; Dumesic, J. A., Selective Hydrogenolysis of Polyols and Cyclic Ethers over Bifunctional Surface Sites on Rhodium-Rhenium Catalysts. J. Am. Chem. Soc. 2011, 133 (32), 12675-12689.
35. Furimsky, E., In Carbons and Carbon-Supported Catalysts in Hydroprocessing, The Royal Society of Chemistry: Cambridge, 2008.
36. Falcone, D. D.; Hack, J. H.; Klyushin, A. Y.; Knop-Gericke, A.; Schlogl, R.; Davis, R. J., Evidence for the Bifunctional Nature of Pt-Re Catalysts for Selective Glycerol Hydrogenolysis. ACS Catal. 2015, 5 (10), 5679-5695.
37. Kim, Y. T.; Dumesic, J. A.; Huber, G. W., Aqueous-phase hydrodeoxygenation of sorbitol: A comparative study of Pt/Zr phosphate and Pt-ReOx/C. J. Catal. 2013, 304, 72-85.
38. Román-Martínez, M. C.; Cazorla-Amorós, D.; Linares-Solano, A.; De Lecea, C. S.-M. n.; Yamashita, H.; Anpo, M., Metal-support interaction in Pt/C catalysts. Influence of the support surface chemistry and the metal precursor. Carbon 1995, 33 (1), 3-13.
39. Chia, M.; O'Neill, B. J.; Alamillo, R.; Dietrich, P. J.; Ribeiro, F. H.; Miller, J. T.; Dumesic, J. A., Bimetallic RhRe/C catalysts for the production of biomass-derived chemicals. J. Catal. 2013, 308, 226-236.
40. Cowley, J. M., Short-range order and long-range order parameters. Physical Review 1965, 138 (5A), 1384-&.
41. Koso, S.; Watanabe, H.; Okumura, K.; Nakagawa, Y.; Tomishige, K., Stable Low-Valence ReOx Cluster Attached on Rh Metal Particles Formed by Hydrogen Reduction and Its Formation Mechanism. J. Phys. Chem. C 2012, 116 (4), 3079-3090.
42. Shinmi, Y.; Koso, S.; Kubota, T.; Nakagawa, Y.; Tomishige, K., Modification of Rh/SiO2 catalyst for the hydrogenolysis of glycerol in water. Appl. Catal. B-Environ. 2010, 94 (3-4), 318-326.
43. Alba-Rubio, A. C.; Sener, C.; Hakim, S. H.; Gostanian, T. M.; Dumesic, J. A., Synthesis of Supported RhMo and PtMo Bimetallic Catalysts by Controlled Surface Reactions. ChemCatChem 2015, 7 (23), 3881-3886.
44. Sener, C.; Wesley, T. S.; Alba-Rubio, A. C.; Kumbhalkar, M. D.; Hakim, S. H.; Ribeiro, F. H.; Miller, J. T.; Dumesic, J. A., PtMo Bimetallic Catalysts Synthesized by Controlled Surface Reactions for Water Gas Shift. ACS Catal. 2016, 6 (2), 1334-1344.
45. Carrasquillo-Flores, R.; Ro, I.; Kumbhalkar, M. D.; Burt, S.; Carrero, C. A.; Alba-Rubio, A. C.; Miller, J. T.; Hermans, I.; Huber, G. W.; Dumesic, J. A., Reverse Water-Gas Shift on Interfacial Sites Formed by Deposition of Oxidized Molybdenum Moieties onto Gold Nanoparticles. J. Am. Chem. Soc. 2015, 137 (32), 10317-10325.
46. Karanjkar, P. U.; Burt, S. P.; Chen, X. L.; Barnett, K. J.; Ball, M. R.; Kumbhalkar, M. D.; Wang, X. H.; Miller, J. B.; Hermans, I.; Dumesic, J. A.; Huber, G. W., Effect of carbon supports on RhRe bifunctional catalysts for selective hydrogenolysis of tetrahydropyran-2-methanol. Catal. Sci. Technol. 2016, 6 (21), 7841-7851.

CHAPTER 7

Final Remarks & Recommendations for Future Work

7.1. Final Remarks

Biomass is an attractive option that is renewable, carbon-neutral, and can be used to alleviate the current dependency on fossil fuels. The preferred pathways from biomass to liquid transportation fuels involve removal of oxygen and/or increasing carbon chain length, leading to an increase in energy density of the molecule. We showed that levoglucosan, an anhydrosugar present in pyrolysis oil, can be converted to monofunctional oxygenates with 56% carbon yield. Nearly 75% carbon yield to monoalkenes and dienes was achieved from these monofunctionals using solid acid catalysts. The dehydration of biomass-derived cyclic ethers can serve as a potential alternative to produce dienes. There is limited work reported in the literature regarding the chemistry that occurs during this process. We have studied the reaction network and determined the intrinsic kinetic parameters for this conversion which is catalyzed by both Brønsted and Lewis solid acids. The understanding of the actual surface chemistry and the active site for this reaction are a few areas for future research.

Endothermic reactions such as dehydrogenation can be carried out to dissipate the heat generated in a hypersonic flight. Alkane dehydrogenation, usually carried over Pt group metals, is accompanied by formation of undesirable carbonaceous species on the catalyst surface. The amount of coke deposited per surface Pt atom was lowered by overcoating Pt/γ-Al_2O_3 catalyst using atomic layer deposition. PtSn bimetallic catalyst showed lower hydrogenolysis activity as compared to monometallic catalyst and higher selectivity to the desired alkene. The geometric and/or ligand effect brought about by addition of a promoter metal to the parent catalyst resulted in alleviating catalyst deactivation.

XAS is powerful technique to characterize monodispersed bimetallic catalysts which are increasingly being used for processes related to biomass valorization. The oxidation states of the constituent metals and their local atomic environment were determined for well-defined supported PtMo, AuMo, and RhRe catalysts using XAS. We have developed correlations between the catalyst structure and its activity thereby elucidating the nature of the active sites.

7.2. Recommendations for Production of Dienes and Distillate Range Hydrocarbons from Lignocellulosic Biomass

7.2.1. Dienes from cyclic ethers

The dehydration of cyclic ethers such as 2-MTHF to pentadienes over solid acids was explored in Chapter 4. Nearly 70% yield to pentadienes was observed with the rest of the carbon present in by-products such a pentanal, pent-en-ols, pentenes and butene. The amorphous SiO_2/Al_2O_3 deactivated continuously due to coke formation resulting in lower pentadiene yield with time on stream. Thus, finding a robust solid acid catalyst that shows high yield to dienes and longer one-way cycle before regeneration is important. Boron phosphate and silicoaluminophosphate (SAPO-40) are possible alternatives as they have shown relatively high stability for gas-phase dehydration of 2-methylbutanal to isoprene[1] and glycerol to acrolein,[2] respectively.

Silica is inert for this dehydration reaction whereas pentadiene formation is observed over γ-Al_2O_3. Reactivity studies over amorphous silica-aluminas with varying SiO_2:Al_2O_3 ratio would be of potential interest to correlate the dehydration activity with the strength and density of acid sites. The Lewis acid sites catalyze the conversion of pent-en-ols to butene and formaldehyde (reverse Prins reaction), thereby resulting in loss of carbon to undesired products as well as formation of corrosive compounds. To this end, the dehydration reaction could be investigated over purely Brønsted acid catalysts such as Amberlyst 70 and supported heteropolyacids (e.g., phosphotungstic acid supported on MCM-41) as well as acids with low Lewis acid site density such as H-Y zeolite. This investigation will verify that butene is indeed formed on the Lewis acid centers and will also provide insight into the nature of the active site for diene formation. From here, the focus can be on catalyst stability and diene selectivity.

We have proposed a reaction pathway for the dehydration of 2-MTHF over SiO_2/Al_2O_3 based on space time studies. The actual surface intermediates and the relative stability of carbenium ions can be determined using density functional theory calculations. Since amorphous SiO_2/Al_2O_3 doesn't have a well-defined structure, the theoretical calculations can be based on a zeolitic structure. These studies will help in confirming the mechanism for 2-MTHF dehydration proposed in Chapter 4.

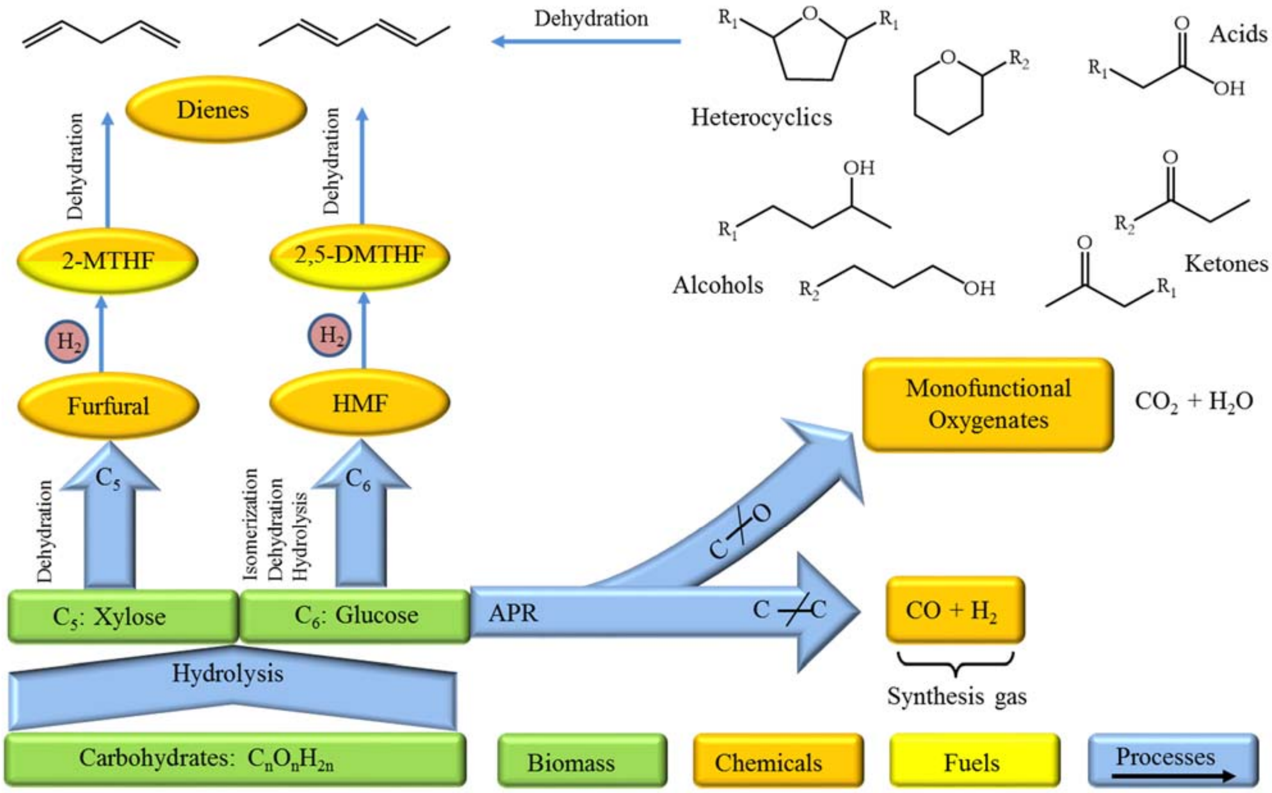

Figure 7.1. Roadmap for conversion of lignocellulosic biomass to precursors for fuels and chemicals. The cyclic ethers present in the monofunctional oxygenates and those produced via furfural and 5-hydroxymethylfurfural can be converted to dienes (Based on Ref[3] and modified).

The cyclic ethers present in the monofunctional stream can be converted to dienes. Alternatively, the C_5 sugars from lignocellulosic biomass can be converted to furfural with yields as high as 85%.[4] Furfural can be converted to 2-MTHF with 97% yield over Pd and Cu catalysts.[5] A roadmap for production of C_5 and C_6 cyclic ethers is illustrated in Figure 7.1. A parametric study to optimize the reaction conditions (reaction temperature, pressure, and space time) will aid in determining the maximum yield of dienes from 2-MTHF and thereby, the overall yield to pentadienes from biomass. During the past years, we have conducted technoeconomic analyses of various catalytic strategies to convert lignocellulose to fuels and chemicals in collaboration with Professor Maravelias' research group. A technoeconomic analysis for the production of pentadienes from the C_5 sugars in biomass will help assess the cost competitiveness of this pathway as compared to the conventional sources such as crude oil and natural gas. This analysis is invaluable in assessing the factors that control the economics of the process and for providing directions for future research for process optimization, thereby improving the economic feasibility.

7.2.2. Coupling of biomass-derived ethanol

In Chapter 3, we discussed the deoxygenation of biomass-derived levoglucosan into distillate range molecules using a 5-step cascade process. In recent years, the conversion of biomass to fuels and chemicals has been widely studied but most of these studies involve multiple steps with certain loss of carbon associated with each step.[6,7] A potential alternative to reduce the number of conversion steps and the carbon losses would be to convert the lignocellulose directly into ethanol[8] and subsequently couple ethanol to middle-distillate range hydrocarbons (diesel and jet). Ethanol is the only renewable liquid fuel produced in large volumes globally. However, it suffers from several limitations, including low energy density, high volatility, and contamination due to absorption of water from atmosphere.

To this end, ethanol can be converted to middle-distillates using 2 routes: dehydration-oligomerization and Guerbet coupling. Ethanol dehydration of ethylene has been extensively studied and >99% yield has been achieved using alumina based catalysts. Ethylene can be then oligomerized to C_{12+} olefins using a process analogous to Shell's Higher Olefin Process.[9] Ethanol can be also be coupled using Guerbet chemistry which involves four fundamental reactions as outlined in Figure 7.2: dehydrogenation, aldolization, dehydration, and hydrogenation.[10] Guerbet coupling can take place in a single reactor or a few reactors in series and requires low pressure which makes it advantageous compared to the dehydration-oligomerization route. It is important to note that Guerbet coupling is a hydrogen-neutral process. This coupling has been reported in the literature with reaction conditions varying from 473-673 K and 0-5 bar H_2 pressure with transition metal (Cu, Ni, and Pd) catalysts supported on basic oxides such as MgO, and $MgAl_xO_y$.[11] Most of the previous work on Guerbet coupling has only focused on forming a dimer (i.e. ethanol is converted into butanol). For this chemistry to be practical for the production of distillate range molecules, it must be expanded to conversion of alcohols into larger oligomers. Understanding the factors affecting the sequential Guerbet couplings starting with ethanol would be of potential interest.

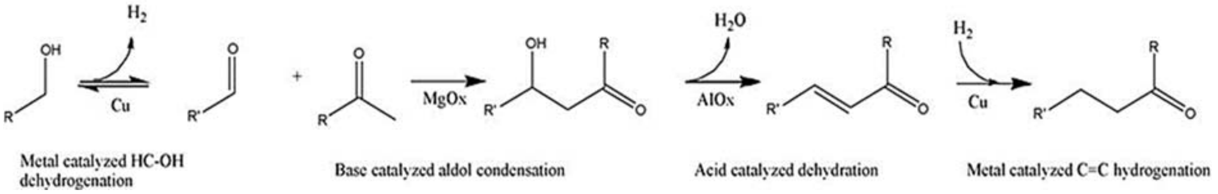

Figure 7.2. Steps involved in Guerbet coupling of alcohols (Adapted from West *et al.*[10]).

For a liquid phase reaction of a mixture of acetaldehyde and heptanal over MgO, $MgAl_xO_y$ and rehydrated $MgAl_xO_y$, Tichit *et al.* concluded that the strength of acid-base pairs dictates the formation of a particular product.[12] Study of mixed oxides with varying Mg/Al ratios would provide insight into the effect of strength and spatial density of acid-base pairs on the product distribution. Optimal ratio of Mg/Al can be chosen by comparing the activity of ethanol dehydrogenation and dehydration, the former being the desirable reaction. The atomic level control of ALD provides the opportunity to create different bifunctional catalysts with homogeneous architectures which in turn makes it easier to draw conclusions from catalyst characterization techniques. Overcoating alumina with varying number of MgO cycles could provide useful information about the nature of acid-base pairs required for Guerbet coupling.

An inherent drawback of biomass processing is the presence of water in the products. The mixed oxide, $MgAl_xO_y$, suffers a loss of surface area upon exposure to water resulting in reformation of the hydrotalcite layered structure. This deactivation is known to be reversible upon calcination. Thus, developing a hydrothermally stable support would be an area of interest. A possible strategy is to prepare catalysts with TiO_x and ZrO_x overcoating using atomic layer deposition as these oxides are hydrothermally stable. Another approach towards catalyst hydrothermal stability would be to coat the support metal oxide with graphitic carbon. Overcoating γ-Al_2O_3 (otherwise hydrothermally unstable) with graphitic carbon before adding Ru showed catalyst stability for more than 100 hours for biomass-derived lactic acid hydrogenation to propylene glycol in aqueous environments.[13]

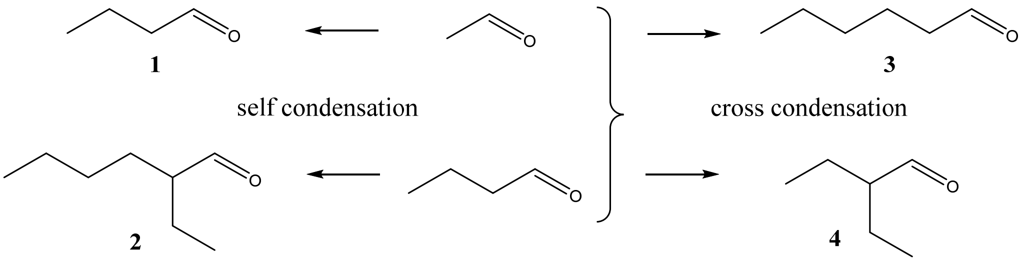

Figure 7.3. Simplified scheme for self and cross condensations of acetaldehyde and butanal. In base catalyzed aldol condensation, abstraction of proton from the α-C leads to formation of carbanion which then attacks the carbonyl carbon on a neighboring aldehyde.

As conversion of ethanol to a diesel range hydrocarbon requires sequential coupling steps, contact time studies can be performed to understand the correlation between residence time and length-scale of coupling i.e. formation of dimers, trimers, tetramers, etc., thereby determining the optimal parameters that promote secondary condensation and not just stop at dimer (butanol) formation. The key to understanding the types of products formed in this reaction involves the understanding of self vs cross aldol condensation as shown in Figure 7.3. Coupling of a C_2 primary anion with an aldehyde will lead to the formation of a linear aldehyde (Figure 7.3, species 1 and 3) whereas that of a C_4 secondary anion with an aldehyde will lead to the formation of a branched aldehyde (Figure 7.3, species 2 and 4). Selectivity of these products depends on the relative rates of formation of carbanion/surface enolate species and their reactivities. To promote formation of a linear aldehyde i.e. attack by a C_2 primary carbanion, the reactor set-up can be designed for a continuous addition of ethanol for maintaining high concentration throughout the course of reaction. Subsequent hydrodeoxygenation of adducts can be carried over Pt/$NbOPO_4$ to yield diesel range alkanes.

7.3. References

1. Hutchings, G. J.; Hudson, I. D.; Bethell, D.; Timms, D. G., Dehydration of 2-methylbutanal and methyl isopropyl ketone to isoprene using boron and aluminium phosphate catalysts. J. Catal. 1999, 188 (2), 291-299.
2. Lourenco, J. P.; Fernandes, A.; Bertolo, R. A.; Ribeiro, M. F., Gas-phase dehydration of glycerol over thermally-stable SAPO-40 catalyst. RSC Adv. 2015, 5 (14), 10667-10674.
3. Wettstein, S. G.; Alonso, D. M.; Gurbuz, E. I.; Dumesic, J. A., A roadmap for conversion of lignocellulosic biomass to chemicals and fuels. Curr. Opin. Chem. Eng. 2012, 1 (3), 218-224.
4. Dumesic, J. A.; Alonso, D. M.; Gürbüz, E. I.; Wettstein, S. G., Production of levulinic acid, furfural, and gamma valerolactone from C5 and C6 carbohydrates in mono- and biphasic systems using gamma-valerolactone as a solvent. US 8,399,688 B2 2013.
5. Dong, F.; Zhu, Y. L.; Ding, G. Q.; Cui, J. L.; Li, X. Q.; Li, Y. W., One-step Conversion of Furfural into 2-Methyltetrahydrofuran under Mild Conditions. ChemSusChem 2015, 8 (9), 1534-1537.
6. Kunkes, E. L.; Simonetti, D. A.; West, R. M.; Serrano-Ruiz, J. C.; Gartner, C. A.; Dumesic, J. A., Catalytic conversion of biomass to monofunctional hydrocarbons and targeted liquid-fuel classes. Science 2008, 322 (5900), 417-421.
7. Alonso, D. M.; Bond, J. Q.; Dumesic, J. A., Catalytic conversion of biomass to biofuels. Green Chem. 2010, 12 (9), 1493-1513.

8. Humbird, D. D., R.; Tao, L.; Kinchin, C.; Hsu, D.; Aden, A.; Schoen, P.; Lukas, J.; Olthof, B.; Worley, M.; Sexton, D.; Dudgeon, D. Process design and economics for biochemical conversion of lignocellulosic biomass to ethanol dilute-acid pretreatment and enzymatic hydrolysis of corn stover; National Renewable Energy Laboratory: Golden, CO :, 2011.
9. Freitas, E. R.; Gum, C. R., Shell's Higher Olefin Process. Chem. Eng. Prog. 1979, 75 (1), 73-76.
10. West, R. M.; Kunkes, E. L.; Simonetti, D. A.; Dumesic, J. A., Catalytic conversion of biomass-derived carbohydrates to fuels and chemicals by formation and upgrading of mono-functional hydrocarbon intermediates. Catal. Today 2009, 147 (2), 115-125.
11. Kozlowski, J. T.; Davis, R. J., Heterogeneous Catalysts for the Guerbet Coupling of Alcohols. ACS Catal. 2013, 3 (7), 1588-1600.
12. Tichit, D.; Lutic, D.; Coq, B.; Durand, R.; Teissier, R., The aldol condensation of acetaldehyde and heptanal on hydrotalcite-type catalysts. J. Catal. 2003, 219 (1), 167-175.
13. Xiong, H. F.; Schwartz, T. J.; Andersen, N. I.; Dumesic, J. A.; Datye, A. K., Graphitic-Carbon Layers on Oxides: Toward Stable Heterogeneous Catalysts for Biomass Conversion Reactions. Angew. Chem.-Int. Edit. 2015, 54 (27), 7939-7943.